




Universitat Autònoma de Barcelona

**ADVERTIMENT.** L'accés als continguts d'aquesta tesi queda condicionat a l'acceptació de les condicions d'ús establertes per la següent llicència Creative Commons:  [http://cat.creativecommons.org/?page\\_id=184](http://cat.creativecommons.org/?page_id=184)

**ADVERTENCIA.** El acceso a los contenidos de esta tesis queda condicionado a la aceptación de las condiciones de uso establecidas por la siguiente licencia Creative Commons:  <http://es.creativecommons.org/blog/licencias/>

**WARNING.** The access to the contents of this doctoral thesis it is limited to the acceptance of the use conditions set by the following Creative Commons license:  <https://creativecommons.org/licenses/?lang=en>

UNIVERSITAT AUTÒNOMA DE BARCELONA

DOCTORAL THESIS

---

**Thermal and thermoelectric  
Properties of Two-dimensional  
Materials**

---

Alois Arrighi

*Supervisors:*

Prof Sergio O. Valenzuela

Prof Clivia Sotomayor-Torres

Physics and Engineering of Nanodevices

Phononic and Photonic Nanostructures

February 10, 2020



UNIVERSITAT AUTÒNOMA DE BARCELONA

*Abstract*

Department of Physics

**Thermal and thermoelectric Properties of Two-dimensional Materials**

by Aloïs Arrighi

Thermal management is becoming a critical issue in the packaging and design of nanoelectronics. Advanced cooling solutions and efficient energy harvesting are key aspects to help keep the trend for ever smaller and faster electronics. This thesis is focused on thermal management and the use of heat waste in emerging materials for electronics. In particular, two-dimensional materials (2DM), and related heterostructures, are amongst the most intriguing prospects for future electronics and are being intensively investigated. Here, two main subjects were explored. First, the thermal transport of suspended 2DMs, including CVD graphene, transition metal dichalcogenides (TMDCs) and heterostructures of TMDCs with hexagonal boron nitride (hBN) and, second, the thermal properties and thermoelectricity of  $(\text{Bi}_{1-x}\text{Sb}_x)_2\text{Te}_3$  (BST) thin films. These materials are being considered for interconnects and THz transistors (graphene), digital electronics (TMDCs) and electrical insulation (hBN) and are well known as thermoelectric generators, as are also materials that have recently been identified as topological insulators (BST).

In the first part, the objective was to demonstrate the measurement of the thermal conductivity of 2DMs using the recently developed two-laser Raman spectroscopy method. Its implementation was rendered difficult by the relatively small exfoliated flakes of the materials investigated and their high thermal conductivity. The thermal conductivity of CVD graphene was found to be about  $300 \text{ W}/(\text{m.K})$ . Although smaller than exfoliated graphene, it is argued that this could be due to grain boundaries and disorder. Exfoliated  $\text{MoS}_2$  and  $\text{MoSe}_2$  (two well-known TMDCs) presented thermal conductivities of 12 to  $24 \text{ W}/(\text{m.K})$  and  $60 \text{ W}/(\text{m.K})$ . Measurements on different membranes of  $\text{MoS}_2$  further showed that the conductivity increases with the thickness in thin membranes (few monolayers). Furthermore, stacking an exfoliated hBN membrane on top of a previously characterized  $\text{MoS}_2$  sample allowed us to demonstrate a notorious increase of the thermal conductivity in the hBN/ $\text{MoS}_2$  heterostructure, when heat is introduced on  $\text{MoS}_2$ . Indeed, when compared with  $\text{MoS}_2$  alone the thermal conductivity is found to be almost one order of magnitude larger,  $185 \text{ W}/(\text{m.K})$ .

For the second part, BST thin films were grown by molecular beam epitaxy. The main objective was to investigate the correlation of the thermoelectric properties of these materials with the Fermi level, which would tune the relative weight of bulk and topological surface state (TSS) transport. It was first demonstrated that controlling the concentration of Sb we could engineer the band structure and tune the Fermi level from the valence to the conduction band. Such demonstration was achieved by using angle-resolved photoemission spectroscopy in combination with conductivity and Hall measurements in relatively thin (10 nm) films. The Sb concentration at which TSS dominated the transport was also identified. Thermoelectric experiments on the same films were then carried out but no clear correlation between the thermopower and the carrier nature was found when the TSSs were dominant. These results indicate that TSS transport has limited influence on the thermoelectric properties. Further studies should be carried out using even thinner films. Finally, a side characterization of the BST thin films using Raman spectroscopy demonstrated specific variations in the behaviour associated to Sb concentration. An increase of the laser power showed the emergence of non-active Raman peaks of undetermined origin. However, they can indicate the presence of broken structural symmetries, surface phonon modes or other effects such as plasmonic resonances. This interesting response is worthy of for further investigation.



# Contents

<b>Abstract</b>	<b>iv</b>
<b>1 Introduction</b>	<b>1</b>
1.1 Energy management . . . . .	1
1.2 Two-dimensional materials . . . . .	4
1.3 Topological insulators . . . . .	6
<b>2 Experimental Techniques</b>	<b>9</b>
2.1 Raman Spectroscopy . . . . .	9
2.1.1 Background . . . . .	9
2.1.2 Raman thermometry . . . . .	10
2.1.3 Two-Laser Raman thermometry . . . . .	14
2.2 Thermoelectric transport measurements . . . . .	15
2.2.1 Thermoelectric effects . . . . .	15
2.2.2 Thermoelectric measurement set-up . . . . .	18
<b>3 Thermal conductivity of suspended 2D materials</b>	<b>21</b>
3.1 Fabrication of the 2D material based suspended membranes	23
3.1.1 Mechanical exfoliation of 2d materials . . . . .	23
3.1.2 Fabrication of the suspended membranes . . . . .	25
3.1.3 Transferring of 2D materials onto the membranes . . . . .	27
3.2 Measurements of Graphene thermal conductivity . . . . .	30
3.3 MoS <sub>2</sub> and hBN/MoS <sub>2</sub> heterostructures thermal conductivity	33
3.3.1 Two laser Raman thermometry of MoS <sub>2</sub> . . . . .	35
3.3.2 Two laser Raman thermometry of hBN/MoS <sub>2</sub> het- erostructure . . . . .	38
3.3.3 Layer thickness and thermal conductivity . . . . .	40
3.4 Measurements of MoSe <sub>2</sub> thermal conductivity . . . . .	42
3.5 Summary . . . . .	44



<b>4</b>	<b>Thermal expansion and Raman spectra of <math>(\text{Bi}_{1-x}\text{Sb}_x)_2\text{Te}_3</math> alloys</b>	<b>49</b>
4.1	Raman Characterization . . . . .	49
4.2	Thermal transport . . . . .	51
4.2.1	Thermal expansion . . . . .	52
4.2.2	Determination of the absorption coefficient . . . . .	53
4.3	Evolution of the Raman spectra with laser intensity . . . . .	55
4.4	Discussion . . . . .	60
4.5	Summary . . . . .	63
<b>5</b>	<b>Seebeck measurement of <math>(\text{Bi}_{1-x}\text{Sb}_x)_2\text{Te}_3</math> alloys</b>	<b>65</b>
5.1	Growth characterization . . . . .	65
5.2	Nanofabrication process . . . . .	69
5.3	Thermopower and Seebeck coefficient estimation . . . . .	73
5.4	Summary . . . . .	79
<b>6</b>	<b>Conclusion and perspective</b>	<b>81</b>
<b>A</b>	<b>Thermal conductivity modelisation</b>	<b>87</b>
<b>B</b>	<b>Raman parameters and BST concentration</b>	<b>91</b>
<b>C</b>	<b>Exfoliation and transfer technique</b>	<b>93</b>
	Graphene exfoliation . . . . .	93
	hBN exfoliation . . . . .	93
	TMDCs exfoliation: . . . . .	95
	TIs film exfoliation: . . . . .	96
C.0.1	Transfer of 2d materials on the membranes . . . . .	97
	PPC or PMMA Transfer: . . . . .	98
	PLLA Transfer: . . . . .	100
	CVD graphene: . . . . .	100
	<b>Bibliography</b>	<b>103</b>

# List of Tables

3.1	Summary of studied MoS <sub>2</sub> samples . . . . .	41
4.1	Thermal expansion values of BST films for different concentration . . . . .	52



# List of Abbreviations

<b>2D</b>	Two-dimensional
<b>TI</b>	Topological Insulators
<b>hBN</b>	hexagonal Boron Nitride
<b>MoS<sub>2</sub></b>	Molybdenum Disulfide
<b>BST</b>	$(Bi_{1-x}Sb_x)_2Te_3$
<b>TMDC</b>	Transition Metal Dichalcogenide
<b>PEND</b>	Physics and Engineering of NanoDevices (group)
<b>P2N</b>	Phononic and Photonic Nanostructures (group)
<b>AEMD</b>	Advanced Electronic Materials and Devices (group)
<b>2LRT</b>	Two Laser Raman Thermometry
<b>PDMS</b>	Polydimethylsiloxane
<b>PPC</b>	Polypropylene Carbonate
<b>PMMA</b>	Poly(Methyl Methacrylate)



# Physical Constants

$$\begin{array}{ll} \text{Speed of Light} & c_0 = 2.997\,924\,58 \times 10^8 \text{ m s}^{-1} \\ \text{Planck constant} & \hbar = 6.626\,070\,04 \times 10^{-34} \text{ m}^2 \text{ kg s}^{-1} \end{array}$$



# List of Symbols

$a$	distance	m
$P$	power	W ( $\text{J s}^{-1}$ )
$\omega$	Raman frequency	$\text{cm}_{-1}$





## Chapter 1

# Introduction

Thermal dissipation and energy harvesting have become critical issues in the packaging and design of nanoelectronics, with increased efficiency requirements for ever smaller and faster electronic devices. Advanced cooling solutions and pragmatic designs require breakthroughs on chip and packaging levels. Sophisticated packaging and cooling technology materials are required to deliver high thermal transfer efficiency, well controlled heat transient behavior, environmental compatibility, low weight while achieving acceptable manufacturing costs. New concepts and materials for converting heat to usable electricity are also in high demand. Two dimensional materials (2DMs) and topological insulators (TIs) are good candidates to spread the heat or convert it into electricity, respectively. This chapter presents an outline of thermal challenges in advanced packaging technology as well as studied materials and their related physics that could help in the thermal management for future generation electronics [38].

### 1.1 Energy management

Each and every fresh generation of microelectronics and product systems, driven by demands for increasing performance, requires advances in electronic device processing and packaging. The market forces to drop the product prices, increase the user experience via miniaturized devices, wireless connectivity, and enhance battery life, making each generation of devices (commonly referred as nodes) ever more complex.[66]

Nowadays more than 50% of the energy used in microprocessors is lost in the production of heat. This is not going to change in the near future,

increasing device density leads to major increases in local heat production. Because it is mandatory to keep the temperature of the working chip relatively low, thermal management is a significant factor for new product designs for electronics. Catastrophic heat failure is generally the consequence of material breakdown of semiconductors due to overheating or thermal fracture of a mechanical component in the electronic package. Suitable heat management is therefore required to prevent heat failure but also to extend the electronic systems lifetime.

**Joule heating:** when a current  $I$  moves through a conductor it produces a Joule heating dissipation  $P = IR^2$ , where  $P$  is the dissipated power, and  $R$  is the resistance of the material.

This obviously implies that thinner, smaller conductors and finer pitch interconnections would result in high heat generation within the package. Careful design can effectively manage interconnection, which involves minimizing current concentration and spreading heat by selecting materials for thermal management.

The main objective of thermal design is thus to arrange the product's heat balance so that it operates consistently throughout its service life under specific environmental conditions. Typically, this is accomplished by taking into consideration all relevant variables:

- Optimizing the integrated circuit heat removal pathways.
- Selecting the best cooling methods via smart constructive designs such as heatsink, thermal vias (Fig. 1.1) and insulated metal substrates.
- Using of high-conductivity materials to reduce heat and interconnecting ability.
- Ensuring cost effectiveness and environmental compliance.

However, the problem of miniaturizing the interconnects is exacerbated by the fact that, as wires are reduced to nm-scale diameter, the surface disorder dominates, bulk transport becomes irrelevant, and the resistance of the wire increases at a very fast pace. The Joule dissipation increases much

faster than inversely proportional to the wire diameter. In addition, the increase of resistance of interconnects leads to slower response of the circuit, and the high concentration of wires to capacitive leakage.

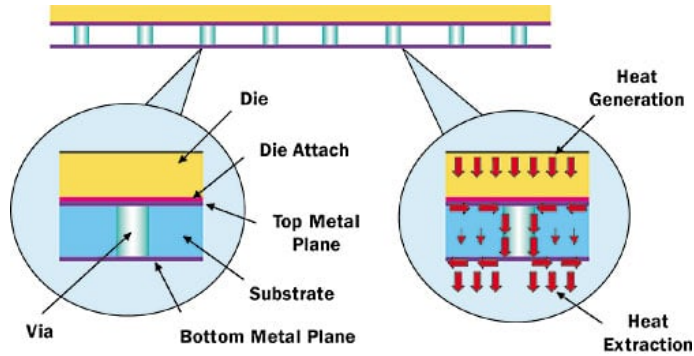


FIGURE 1.1: Thermal vias representation. Mechanically drilled through-hole-contacts (vias) are placed directly under the components yielding heat dissipation.

**Moore's law** - Modern electronics have experienced miniaturization and high-power densification significantly over the past century. That phenomenon is still continuing nowadays. Moore's law presents the theory that approximately every eighteen months the number of transistors by square area will double. Considerably, this estimate of electronics growth is directly related to thermal dispersion. Thermal design power (TDP) in industrial use is described as the highest quantity of heat a chip can produce in its working condition. The Figure 1.2 represents the thermal design power and number of transistor of Intel microprocessors as a function of the year introduced in the market with the overall goal to reduce the first one and increase second [41, 91].

Therefore, collecting data on materials and component mechanisms failure is a requirement in the heat design operations. Detailed information are required to prevent a bad impact on the product's functionality and efficiency. On the one hand, design can be effective in improving heat dissipation, although it has limitations and new materials are constantly evaluated. On the other hand, there is always going to be large quantities of Joule heating being created, thus it is becoming more and more important to find ways to take advantage of that heat and design uses that harvest the

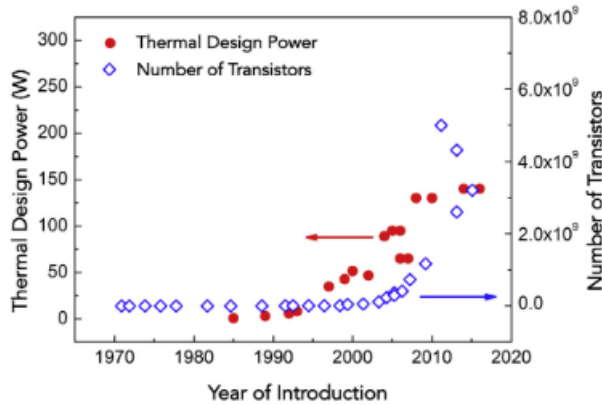


FIGURE 1.2: Thermal design power and number of transistors for the case of Intel microprocessors vs. year of introduction.

associated energy. This thesis explores unique type of materials that might assist in the future adequate of thermal management and thermoelectric energy harvesting. The materials investigated include two dimensional materials (2DMs) and topological insulators (TIs).

On the one hand, 2DMs have drawn outstanding interest for heat processing, in particular graphene and hexagonal boron nitride (hBN) due to their superior thermal properties. On another hand, TIs have a huge potential in electronics and magnetism. Their boundary states are topologically robust against non-magnetic impurities and defects of their boundary states, making them, in principle highly conducting even when their dimension is reduced to nm scales. They are also great thermoelectric materials, which in overheated environments can be very beneficial.

## 1.2 Two-dimensional materials

Since the isolation of atomically-thin layers of graphene in 2004 by Geim and Novoselov, graphene research has grown tremendously. In large part graphene research has been driven by exciting possibilities for device applications, which span from electronic to optoelectronic, thermoelectronic

and sensing devices. This flurry of research has been accompanied by the subsequent emergence of other 2DMs exhibiting metallic, insulating, semi-conducting, superconducting and ferromagnetic behaviors, which have fostered a paradigm shift in materials science owing to their rich underlying physics and multitude of novel phenomena. Further progress in the field on a pace with advances in sample fabrication have enabled to combine such 2DMs in complex heterostructures with engineered properties. Such van der Waals heterostructures are a new class of artificial materials formed by a controlled assembly of atomically thin crystals in which properties can be borrowed among the constituent materials [30, 71].

In this thesis we have studied three 2DMs as potential systems for future thermal management: graphene, hexagonal boron nitride (hBN) and transition metal dichalcogenides (TMDCs).

Graphene is the basic structural element of other allotropes such as 0-dimensional fullerenes, one-dimensional carbon nanotubes and three-dimensional graphite. It is a zero-gap material made of a single atomic layer of carbon atoms arranged in two triangular lattices forming  $\sigma$  bonds from  $sp^2$  in-plane hybridization of the valence electron orbitals. Particularly relevant for thermal management is its large thermal conductivity measured in freely-suspended membranes of single-layer ( $\sim 2000$  W/m K) [11, 27, 52, 100] and bilayer graphene ( $\sim 600$  W/m K) [75], which are significantly higher than that of conventional bulk materials used as heatsinks such as aluminium ( $\sim 240$  W/m K) and copper ( $\sim 400$  W/m K).

hBN, on the other hand, is the most typical 2D insulator material, which has a similar structure to graphene where nitrogen and boron atoms are arranged in an hexagonal lattice bounded by covalent forces [26]. It has an atomically smooth and chemically inert surface free of dangling bonds and charge traps, providing an excellent insulating substrate for electronics [21]. It has been predicted to exhibit a high thermal conductivity of about 550 W/m K at room temperature [44]. First studies on hBN bulk thermal conductivity reported values ranging from 200 to 400 W/m K [44, 89] in its pristine form, whereas in controlled boron isotope concentration layers the thermal conductivity can be enhanced up to 550 W/m K [106].

TMDCs are established by the chemical formula  $\text{MX}_2$ , where M is for the transition metal from the 4th, 5th, or 6th group of the periodic table and X represents a chalcogen, such as S, Te or Se (Figure 1.3). Owing to their semiconducting character, these materials offer potential for advanced devices and an alternative to graphene. We have focused our studies to Molybdenum disulfide ( $\text{MoS}_2$ ), that is one of the best examined TMDCs. As to the thermal properties, its thermal conductivity is significantly lower than that of graphene with reported values of  $\sim 35 \text{ W/m K}$  for monolayer [103] and  $\sim 50 \text{ W/m K}$  for bilayer suspended samples [102].

The figure shows a standard periodic table of elements. The transition metals, which are the elements in the d-block (groups 3-10) and the f-block (lanthanides and actinides), are highlighted in red. This includes elements from Scandium (Sc) to Zinc (Zn) in the first row of transition metals, and from Scandium (Sc) to Mercury (Hg) in the second row. The lanthanide and actinide series are also highlighted in red.

FIGURE 1.3: Periodic table representation of the TMDCs

### 1.3 Topological insulators

TIs represent a non-trivial class of gapped materials whose band symmetry leads to conducting surface (or boundary states) states. Such states appear due to band inversion due to large spin-orbit coupling. Therefore typically TIs are composed of heavy elements. If the Fermi level lies in the gap, the bulk is insulating, which means that electrons can only travel along the surface of the material. Other type of band insulators can also have conductive surface states, but they are susceptible to disorder and electrons become localized and do not contribute to the transport. A unique property of TIs is that, as long as time-reversal symmetry is conserved, their surface states are protected against localization (backscattering is suppressed).

It is not by chance that TIs are also excellent thermoelectric materials. Indeed, a large thermoelectric figure of merit,  $ZT$ , is typically found in materials in which there is a large change of conductivity with energy (Fermi level) and that are bad thermal conductors. Because the gap of TIs cannot be larger than the spin orbit interaction (a few 100s of meV), TIs are in fact narrow gap semiconductors with necessary change in the electrical conductivity at room temperature as a function of energy. This first condition ensures a large thermopower (or Seebeck coefficient). In addition, because they are composed of heavy elements, thermal transport through phonons is typically suppressed. Many of the best thermoelectric materials known turn out to be topological insulators. However, because the existence of the topologically boundary states has been discovered recently, the influence on the thermoelectric properties of these materials is unexplored. In this thesis, the thermoelectric properties of a family of such materials  $(\text{Bi}_{1-x}\text{Sb}_x)_2\text{Te}_3$ , with  $0 \leq x \leq 1$  is re-examined (Chapter 4 and 5).





## Chapter 2

# Experimental Techniques

This chapter deals with the instrumentation and experimental techniques used in this thesis. In the first part, we describe Raman-based techniques for measuring the thermal conductivity of materials. Our survey on Raman spectroscopy does not intend to be exhaustive. We have omitted several unnecessary advanced concepts to the reader. In exchange, we present a more detailed description of the single and two-laser Raman thermometry techniques that we have used for measuring the thermal conductivity in thin films and freely-suspended membranes. In the second part, we summarize basic thermoelectric phenomena, with special emphasis on the Seebeck effect that shall be needed in the sequel. We then follow with a description of the experimental setup used for measuring the Seebeck coefficient in  $(Bi_{1-x}Sb_x)_2Te_3$  (BST) thin films.

## 2.1 Raman Spectroscopy

### 2.1.1 Background

Raman spectroscopy is a versatile contactless technique based on the study of vibrational modes of molecules and atoms of a medium. Unlike infrared (IR) spectroscopy, based on the absorption of electromagnetic radiation by molecules, Raman spectroscopy relies on analyzing the inelastically scattered radiation of a monochromatic beam of light (laser) that interacts with molecules. The oscillating electromagnetic field of the beam causes a periodic fluctuation in the electronic density of the molecules that conform the material, resulting in an induced oscillating electric dipole moment.

This electronic perturbation is then propagated and give rise to the scattering of light. The scattering mechanism can be separated into two classes: elastic and inelastic scattering. In the first one, called Rayleigh scattering, incident and scattered lights have the same frequency  $\nu_0$ , whereas in the inelastic process, also known as Raman and Brillouin scattering, light is scattered at a different frequency  $\nu$  compared to the incident one. The shift in frequency, known as Raman shift [79] and commonly express in  $\text{cm}^{-1}$ , is given by

$$\Delta\nu = \left( \frac{1}{\lambda_0} - \frac{1}{\lambda_R} \right), \quad (2.1)$$

$\lambda_0$  and  $\lambda_R$  being the wavelength of the excitation source and the Raman spectra, respectively.

Besides the elastic Rayleigh mode, the inelastic scattering process encloses two different modes in the Raman spectra known as Stokes and anti-Stokes peaks, with frequencies  $\nu_0 - \nu_{vib}$  and  $\nu_0 + \nu_{vib}$  respectively (see Fig. 2.1).

As each material has a set of characteristic atomic and molecular vibrations which depends on the crystalline structure and the nature of the chemical bonds, it is possible to use this technique as a tool of elementary and structural characterization of the materials. In addition, perturbations in the crystal structure induced by: embedded strain, thermal expansion, sample compositional and structural disorder, impurities and contamination of the sample as well as the presence of pseudo-phases and deformation of the material can be also detected using this technique [13, 67, 12, 19]. In the case of 2DMs, since the advent of graphene, and followed by a flurry of research on related layered crystals, Raman spectroscopy has positioned as a fundamental tool to extract key structural and electronic information on these materials such as the number of layers, the edge termination, or the effects of external perturbations including electric field, magnetic field and mechanical strain.[64, 65, 84, 35, 59, 17, 8].

### 2.1.2 Raman thermometry

Another particular application of Raman spectroscopy is the estimation of the local temperature of the material under analysis, and, consequently, its

thermal properties. The thermal conductivity  $\kappa$ , that quantifies how well a material conducts heat, is defined by the Fourier law

$$q = -\kappa\Delta T \quad (2.2)$$

where  $q$  denotes the heat flux density and  $\Delta T$  the temperature gradient. Increasing or decreasing the temperature of a material produces a displacement of atoms from their equilibrium positions, resulting in an overall volumetric expansion or contraction of the lattice. The enlargement (shrinkage) of the lattice leads to a change in the interatomic forces and, as consequence, a shift to lower (higher) wave numbers in the Raman modes as the temperature increases (decreases), so that  $\Delta\nu = \chi\Delta T$ . Similarly, the linewidth of the Raman spectrum is broadened (narrowed) as the temperature increases (decreases) as consequence of the temperature dependence of the phonon lifetime. In addition, owing to the temperature dependence of the phonon population the Stokes and anti-Stokes peaks have a different amplitude.

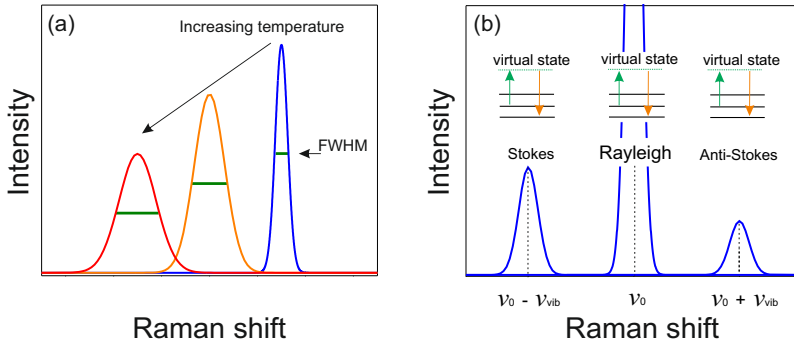


FIGURE 2.1: Schematic examples of Raman mode as thermometer. (a) Redshift, intensity decrease and broadening of the linewidth of an active Raman mode due to temperature increasing. (b) Raman spectrum showing the anti-Stokes, Rayleigh, and Stokes signal.

As schematically shown in Fig. 2.1, the local temperature of a sample can be probed using: (i) the shift in peak position, (ii) the change in the mode intensity, (iii) the broadening of the linewidth or (iv) the change in

the Stoke anti-Stoke amplitude ratio.

Figure 2.2 shows a schematic representation of simple application of Raman thermometry in suspended membranes.

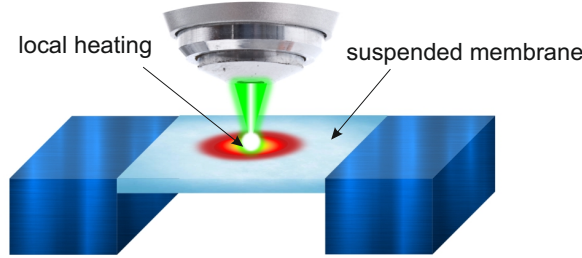


FIGURE 2.2: Artistic view of the Raman thermometry method applied in suspended thin films membranes

If one uses the red-shift of the Raman mode as a thermometer, the local temperature of a focused spot can be easily determined by fitting the spectral position of the observed Raman mode, given a previous calibration of its spectral position with temperature. Then, if a given material absorbs certain power arising from the laser source, an increase of the incident power leads to local heating and, thus, to a red-shift of the observed Raman signal. The temperature rise in the impinged region will depend on the intrinsic thermal properties of the investigated material. Alternatively, if the material is heated by an external source (*e.g.*, by passing an electrical current or illuminating with a second laser) it is possible to probe the temperature gradients driven by this source based on the red-shift of its Raman signal. Once the thermal map or the local temperature rise is measured, the thermal conductivity value of the sample can be extracted by solving the heat diffusion equation with boundary conditions given by the specific sample geometry. For bulk materials, the three-dimensional heat equation has to be solved considering a Gaussian power source [77]. For systems with thicknesses  $h$  much smaller than their lateral dimensions such as thin films and 2DMs, the heat diffusion equation can be approximated as [73].

$$-\nabla^2 T = \frac{P_{abs}}{2\pi h \sigma^2 \kappa} \exp\left(-\frac{r^2}{\sigma^2}\right) \quad (2.3)$$

where  $\sigma$  is the electrical conductivity, and  $P_{abs}$  is the power absorbed in the material.

For supported thin films, the solution to the heat equation is more complex due to the interface resistances between the film and the substrate [Huang2009, 39, 32], while for suspended membranes the analytical expression of the thermal conductivity  $\kappa$ , is given by

$$\kappa = \left( \frac{\partial \nu}{\partial T} \right) \cdot \left( \frac{1}{2\pi\hbar} \right) \cdot \left( \frac{\partial \nu}{\partial P_{abs}} \right)^{-1} \quad (2.4)$$

where  $\nu$  is the Raman peak position.

Measurements in Fig.2.3 are examples of temperature dependent Raman spectra of two different active phonon modes in few layers MoS<sub>2</sub> [83]. From the peak position as a function of temperature  $\kappa$  was estimated to be  $\kappa \sim 50$  W/m K.

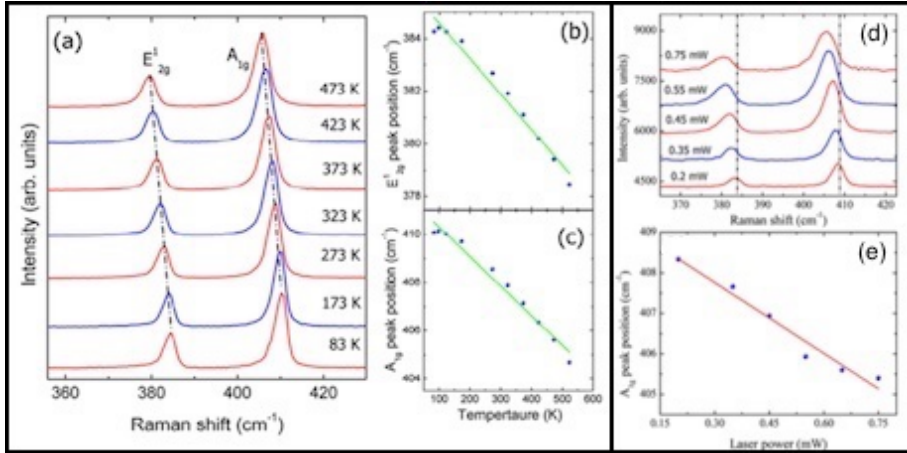


FIGURE 2.3: Raman thermometry in few layers MoS<sub>2</sub>. Left panel: (a) Raman spectra for different temperatures. Temperature dependence of the (b) E<sub>2g</sub> and (c) A<sub>1g</sub> Raman peaks. Right panel: (a) Raman spectra for different incident laser powers. (b) Power dependence of the A<sub>1g</sub> phonon mode. Figure adapted from [83]

### 2.1.3 Two-Laser Raman thermometry

The technique was developed in the Phononic and Photonic Nanostructures group and validated in a seminal work investigating the thermal properties of free-standing single crystalline Si membranes with thicknesses from 200 to 2000 nm. The technique is based on pump-probe measurements in which a thermal distribution of phonons is created using a heating laser, while a second laser is used to determine the local temperature through the spectral position of a Raman active mode. The schematics of the technique is shown in Fig. 2.4. The bottom laser with a continuous wavelength of  $\lambda_h = 405$  nm is used as heating source. The laser spot impinges on the material creating a Gaussian distribution of heat. A second laser with a continuous wavelength of  $\lambda_p = 532$  nm impinges on the sample from the top and probes the local temperature through the spectral shift of an active Raman mode. Pump and probe laser powers have a 10:1 ratio in order to avoid any additional perturbation in the sample.

Considering an isotropic membrane, the measured temperature profile is given by the solution to Eq. 2.2 with  $q = P_{abs}/A$ , where  $A$  the cross sectional area of the heat flux. In the case of freely-suspended membranes  $A = 2\pi rh$ , and considering a temperature independent  $\kappa = \kappa_0$ , the temperature profile is given by

$$T(r) = T_0 - \frac{P_{abs}}{2\pi h \kappa_0} \ln\left(\frac{r}{r_0}\right) \quad (2.5)$$

In this thesis, we have used two different Raman experimental setups depending on the samples to be characterized. The first setup, allows to measure  $\kappa$  and to perform thermal field mapping of freely-suspended membranes either using single or two-laser Raman thermometry. The lasers are focused using a long distance 50x optical objective with numerical aperture of  $NA = 0.55$ , enabling to measure  $\kappa$  under variable temperature conditions with a spacial resolution of  $\sim 500$  nm. The second setup, allows to determine the thermal expansion of supported thin films by measuring their temperature dependent Raman spectra. The laser is focused using a long distance 50x optical objective with  $NA = 0.5$  and spatial resolution of  $\sim 800$  nm. Additionally, the setup is endowed with or a short distance 100x objective with  $NA = 0.9$  providing a higher spatial resolution of  $\sim 400$  nm that has been used to measure high-resolution Raman spectra in BST thin

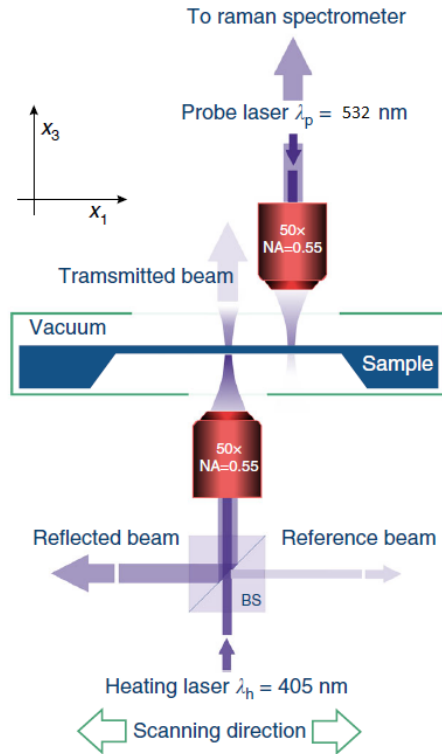


FIGURE 2.4: Schematic representation of the Two-laser Raman thermometry [36].

films.

## 2.2 Thermoelectric transport measurements

### 2.2.1 Thermoelectric effects

Thermoelectric effects encompass phenomena in which temperature differences are converted to electric voltages and viceversa. These classical effects have been observed in solids dating back to the XIX century [87, 74, 93]. Since then, thermoelectricity has become a major field of research in solid state physics, especially since the beginning of the integrated circuit



era, in which inefficient heat dissipation in ever smaller chips and interconnects may cause device failure [23]. Thus, nanostructured and low dimensional thermoelectric materials are gathering increasing attention as a means of managing heat in nanoscale structures [90, 24].

We consider first the Seebeck effect, in which a temperature difference  $\Delta T$  between the two ends of a material results in a voltage difference  $\Delta V$ .

$$\Delta V = S\Delta T \quad (2.6)$$

The magnitude of this effect is given by the Seebeck coefficient  $S$  of the material, also called thermopower. The Seebeck coefficient in metallic samples is well described by the semi-classical Mott relation [20, 29]

$$S_{Mott} = -\frac{\pi^2 k_B^2 T}{3 |e|} \left( \frac{d \ln \sigma(E)}{dE} \right)_{E=E_F} \quad (2.7)$$

where  $e$  is the electron charge,  $k_B$  the Boltzmann constant, and  $E_F$  the Fermi energy.

The density of states (DOS) at finite temperature is given by the Fermi-Dirac distribution

$$f_{FD}(E) = \left[ \exp\left(\frac{E - E_F}{k_B T}\right) + 1 \right]^{-1}.$$

(2.8)

with different number of states in the cold and hot sides of the material, as shown in Fig. 5.12. Owing to the dependence of the electrical conductivity  $\sigma$  with energy  $E$ , carriers in the hot side with higher energy will diffuse to the cold region. This heat flow is accompanied of a charge accumulation process that results in a thermoelectric voltage.

A second ubiquitous phenomenon in thermoelectricity is the Peltier effect, in which the flow of an electric current can either produce or absorb heat at the junction between two different materials. The Peltier heat generated at the junction between the two materials with Peltier coefficients  $\Pi_a$  and  $\Pi_b$  is given by

$$\dot{Q} = (\Pi_a - \Pi_b) \cdot I \quad (2.9)$$

where  $I$  is the current across the junction.

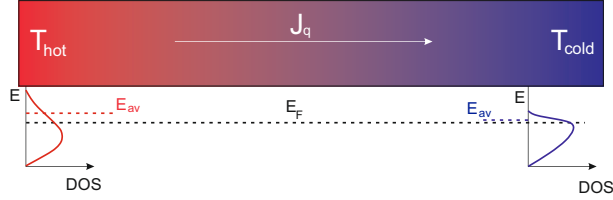


FIGURE 2.5: Schematics of the Seebeck effect. (a) A temperature difference across two reservoirs with temperatures  $T_{hot} > T_{cold}$  drives a heat current  $J_q$ , leading to a built-in thermoelectric voltage. (b) Carriers in the left reservoir have an average energy  $E_{av}$  larger than in the right reservoir, resulting in a net carrier diffusion from hot to cold end, building up a thermoelectric voltage

The Seebeck and Peltier effects are related by means of the second Thomson relation

$$\Pi = ST$$

The maximum efficiency of a thermoelectric device for both thermoelectric power generation and cooling efficiency is given by its figure of merit  $zT$ ,

$$zT = \frac{S^2 \sigma T}{\kappa} \quad (2.10)$$

where  $\kappa = \kappa_p + \kappa_e$ , with  $\kappa_p$  and  $\kappa_e$  the phononic and electronic thermal conductivity respectively, and  $\sigma$  is related with the carrier concentration  $n$  by the formula  $\sigma = ne\mu$ , with  $\mu$  the carrier mobility. The carrier concentration  $n$  of the sample can be varied in semiconductor-based compounds by controlling the doping level, which in principle could be used as a tune knob parameter for maximizing  $zT$ . Figure 2.6(a) shows the influence of  $n$  on  $zT$ ,  $\kappa$ ,  $\sigma$  and  $S$ , exhibiting a peak between in  $zT$  at concentrations  $n \sim 10^9$ - $10^{10} \text{ cm}^{-3}$ . From the temperature dependence measurement of  $zT$  for different n-type and p-type semiconductors (Figs. 2.6.b and 2.6.c) it can be deduced the high room-temperature performance of  $\text{Bi}_2\text{Te}_3$  ( $\text{Sb}_2\text{Te}_3$ ) as n-type (p-type) thermoelectric materials.

As detailed in Chapter 5, we have carried out thermoelectric measurements in thin films of BST as a function of temperature at different Sb

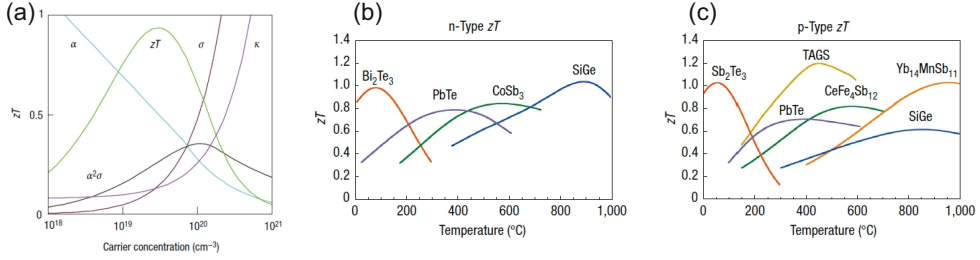


FIGURE 2.6: a) Maximization of figure of merit  $zT$  involves a compromise among  $\kappa$ ,  $\sigma$  and  $S$  parameters- Figure of merit for conventional (c) p-type and (d) n-type thermoelectric materials. Figure adapted from [90]

concentrations with the aim to look at the influence of topological surface states on their thermoelectric response.

## 2.2.2 Thermoelectric measurement set-up

Thermoelectric measurements have been carried out in a cryogen-free cryostat with a temperature operation range from 350 K down to 6.5 K and temperature stabilization better than 50 mK. The set-up allows to apply magnetic fields up to 0.7 T by means of an external electromagnet. The samples, placed in 24-pin socket inside the cryostat, are connected to the electronics using a Fisher connector. The electronics comprises a current pulse source (Keithley 6621) used for heat generation. Current pulses of 750 ms width and  $f = 0.2$  Hz are triggered to a nano-voltmeter (Keithley 2182A) that measures the d.c voltage that results from a temperature difference in the sample. The set-up is fully computer controlled using the Labview software interface.

The schematic of the measurement configuration and device are shown in Fig. 2.7(a) and 2.7(b). As explained below, the metal contacts attached to the sample act as voltage probes and thermometers.

The generation and quantification of the temperature gradient is as follows. The temperature gradient is generated by a current  $I_{heater}$  flowing through a microfabricated Pd heater that produces a Joule heating in the

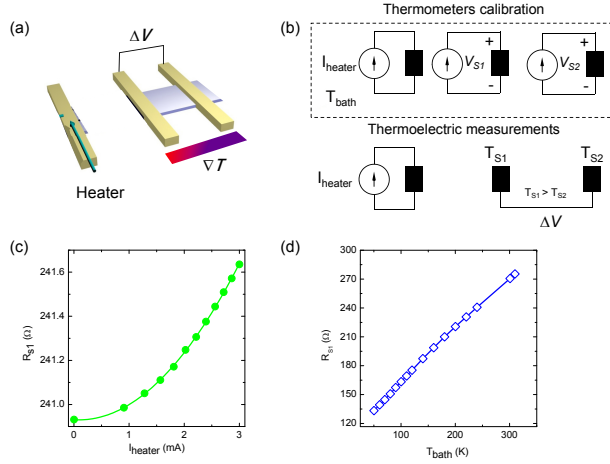


FIGURE 2.7: (a) Sample geometry and measurements configuration. (b) Schematics of the current bias configuration for calibration of the two thermometers (top panel) and for thermoelectric voltage measurements (bottom panel). (c) Resistance of sensor 1 as a function of the current in the heater measured at  $T_{bath} = 240$  K. The quadratic dependence is due to Joule heating. (d) Resistance of sensor 1 as a function of the bath temperature for calibration of the thermometers.

contacts. We quantify the temperature using two two resistive Pd thermometers attached to the sample. We monitor the resistance of both thermometers,  $R_{S1}$  and  $R_{S2}$ , with a standard four probe technique as a function of  $I_{heater}$  and obtaining  $R_{S1}$  and  $R_{S2}$  as a function of the dissipated power (Fig. 2.7(b) and 2.7(c)). Each thermometer has to be previously calibrated by measuring their resistance as a function of the bath temperature  $T_{bath}$ . As shown in Fig. 2.7(d) we have observed a linear relationship between  $T_{bath}$  and  $R_{S1,S2}$  down to 200 K. At lower temperatures we have observed a deviation from the linear scaling. Thus, the resistance-temperature conversion coefficient is obtained by a sixth-order polynomial extrapolation.



## Chapter 3

# Thermal conductivity of suspended 2D materials

The main goal of the current chapter is to study the thermal conductivity of crystalline two-dimensional (2D) materials, such as graphene, hexagonal boron nitride (hBN) and transition metal dichalcogenides (TMDC), and the possibility to use them as thermal management materials. Progress in the electronics industry has led to an increased need for novel thermal management (i.e. ability to control the temperature of a system) technologies to improve the system performance. Two-dimensional materials, and related heterostructures, are amongst the most intriguing prospects for future electronics and are being intensively investigated, gaining significant interest in nanoelectronic applications. They are relatively simple to produce in small scale and complex structures and can have outstanding thermal and electrical properties, and could present in metallic, semiconducting and insulating character. For example, the ability to reduce the thickness of the channel down to atomic scales would result into enhanced gate control, both relaxing the requirements on gate dielectrics and suppressing short-channel effects. However, the behaviour of the material in working conditions is still not well understood, and this includes how the heat dissipates from a hot spot (ballistically or diffusively). In this chapter, significant efforts have been invested in fine-tuning device fabrication parameters and protocols and to adapt measurement techniques to the peculiarities and constraints imposed by the selected materials. They include methods to transfer and fabricate few-layer suspended membranes by exfoliation and

deterministic transfer, and adapting the recently developed two-laser Raman thermometry (2LRT) for determining heat propagation and the thermal properties of the systems.

In this chapter we demonstrate the fabrication of suspended 2D materials such as: CVD graphene, MoS<sub>2</sub> and MoSe<sub>2</sub> (TMDCs) and hBN. These delicate membranes, comprising few monolayers, were placed in 20 μm diameter holes to perform two-laser Raman spectroscopy measurements. The relatively large diameter of the holes was necessary to achieve enough lateral resolution in heat spreading, given the size of the laser spot (around 1.0 μm) and the relatively large thermal conductivities of investigated materials. As described in Chapter 2, the advantage of the use of two-laser Raman is to avoid any assumptions in the flow of heat, as the actual local temperature is directly measured. We measured the thermal conductivity of monolayer CVD graphene of, 300 W/(m.K), which is one order of magnitude smaller than the values reported for exfoliated graphene. This discrepancy could be attributed to grain boundaries and disorder. Similar measurements were also carried out in multilayer MoS<sub>2</sub> and MoSe<sub>2</sub>. The thermal conductivity measurements in the former were estimated to be 24 W/(m.K), several orders of magnitude larger than in the polycrystalline version of the material. In regards to MoSe<sub>2</sub> the thermal conductivity of an 8-layer membrane was about 60 W/(m.K), very close to that reported with bilayer MoSe<sub>2</sub>. The larger value in comparison to MoS<sub>2</sub> is currently not fully understood and must be further investigated. In addition a heterostructure out of hBN and MoS<sub>2</sub> was fabricated. The heat was released in MoS<sub>2</sub>, using a laser with energy surpassing its bandgap (2 eV) but not that of hBN (6eV), and then the change of the overall thermal conductivity between bare MoS<sub>2</sub> and hBN/ MoS<sub>2</sub> was evaluated. This experiment roughly recreates the Joule heating in an MoS<sub>2</sub> device surrounded by hBN dielectric material. Notably, the bilayer exhibited about a factor 8 increase in the effective thermal conductivity, demonstrating not only the capacity of hBN to transport heat but also of heat transfer between the two materials.

Note that the demonstrating thermal conductivity measurements on 2D materials single crystals using 2LRT was a main goal of this thesis. This

explains the effort dedicated to fabrication of the samples. Indeed, as mentioned in Chapter 2, 2LRT was first implemented to measure the conductivity of Si membranes. The large size of these membranes (in the range of  $100\ \mu$ ) allows to minimize heat transfer to the substrate and generate large measurable temperature gradients with Raman, with a first laser focused in its center, to induce the gradient, and a second scanned laser to measure the temperature [80]. The technique was later on successfully implemented in membranes of polycrystalline  $\text{MoS}_2$ . The suspended membranes were smaller, but the thermal gradients that could be generated were still large due to the low thermal conductivity  $k$  of these membranes, which is of the order of  $1\ \text{WmK}^{-1}$ .

In the samples studied in this thesis, the size of the membranes is limited by the lateral dimensions of the flakes, that is, few 10s of  $\mu\text{m}$ . In addition, the thermal conductivity of the materials of interests is orders of magnitude larger than that of polycrystalline  $\text{MoS}_2$ . This results in a reduced thermal gradient, making more difficult their direct measurements. It was thus not obvious that two-laser thermometry would be sensitive enough to be implemented with small crystals with high  $k$  and small lateral dimensions.

### 3.1 Fabrication of the 2D material based suspended membranes

In this first section, the process to fabricate suspended 2D materials is presented in detail. This includes methods to transfer and fabricate few-layer suspended membranes by exfoliation and deterministic transfer. A detailed and systematic description of the fabrication steps can be found in Appendix C.

#### 3.1.1 Mechanical exfoliation of 2d materials

The 2D materials research was triggered by the ability to separate and manipulate very thin layers from bulk crystals. Graphene was the first 2D material to be isolated. The method was very simple by repeatedly thinning down the thick layers of graphite with adhesive tape. This method is called "mechanical exfoliation". Since then, other methods were invented,



one of the most frequently implemented being chemical synthesis and liquid exfoliation. Graphene-based on chemical synthesis was initially shown to be of inferior quality compared to exfoliated flakes in terms of carrier mobility. Nowadays, it is possible to fabricate high-quality graphene over large areas using chemical vapor deposition (CVD). Therefore it becomes paramount to investigate its transport properties. CVD graphene is polycrystalline and a main goal is to understand the relevance of impact of grain size, grain boundaries and disorder in its transport properties.

On the other hand, the focus of recent fundamental research has been shifted to other 2D materials. In particular, transition metal dichalcogenide (TMDC) can be semiconductors. Their composition is of the type  $MX_2$ , with M as a transition metal atom (Mo, W, etc.) and X is a chalcogen atom (S, Se, or Te.). These materials exhibit attractive electronic, optoelectronic and mechanical properties.

**Graphene exfoliation.** "Mechanical exfoliation" method was used to obtain thin and long graphene flakes (details are described in Appendix C). Mechanical exfoliation, was the method discovered initially by Andre Geim and Konstantin Novoselov, and uses an adhesive tape to cleave graphite into graphene. Achieving single-layer graphene typically requires multiple exfoliation steps. This exfoliation method, in principle, can be used for any layered van der Waals material, as described below. The inspection of the exfoliated flakes was done using optical microscopy and, more precisely, by using Raman spectroscopy. Raman spectra presents a definite change in its peak position depending on the number of layers.

**hBN exfoliation.** hBN monolayer flakes are very harder to exfoliate than graphene. The hBN's crystal source is small (around 1mm) and every exfoliation reduces not only its thickness but also the lateral area, becoming then very difficult to have larger monolayer flakes. hBN flakes are often used as an intermediate between  $SiO_2/Si$  or other 2D materials to achieve an atomically smooth and inert substrate ( $SiO_2$  has nm roughness and trapped charges). The thinnest layers (1L to 3L) can also be used as a tunneling barrier.

**TMDCs exfoliation.** Similar exfoliation methods are used for the TMDCs. This thesis only focuses on MoS<sub>2</sub> and MoSe<sub>2</sub>. TMDC exfoliation can be done with PDMS. To obtain large monolayer of TMDCs that contain Sulfur gold can be deposited onto it. This method has been implemented in MoS<sub>2</sub>. The Sulfur atoms have a strong interaction with the gold which will enable a controlled exfoliation.

**TIs film exfoliation** It is also possible to exfoliate film topological insulators grown by the MBE.[47] Since the TIs are sensitive to oxidation thus great care needs to be taken. Such surface oxidation is the origin of the degradation of topological surface states, and typically these materials are capped in ultrahigh vacuum to avoid oxidation.

### 3.1.2 Fabrication of the suspended membranes

A prerequisite to properly estimate the thermal conductivity of 2D materials is to measure them suspended to avoid any interaction with the substrate. A non-destructive technique like Raman thermometry allows obtaining the thermal conductivity without the need of electrical contacts. Yet, to limit the risk of damaging the 2D materials requires that the suspended area is not too large. After performing several tests, we selected holes with diameters from 10 $\mu$ m to 20 $\mu$ m. A larger diameter would lead to a very small yield of membranes, as they would break in the transfer and release process. In addition, multiple substrates and hole were tested during this thesis to optimize the measurements.

Initially, simple substrates were designed by spin coating polymer on top of glass slide and then the holes were defined by lithography. However, heat spreading at the border of the suspended flake was unreliable, it also raised problems due to reflections in the glass. To avoid this issues, a 200  $\mu$ m silicon substrate was used with tubular holes all the way though. Unfortunately, the geometry had the drawback that transmission of the light through the holes required perfect focus and an alignment. Even then, the light was reflected in the hole walls and the hole behaved like as a cavity. In the final design, the 2D membranes were deposited on wholes made on thin Si layers (much thinner than the width of the holes). This was achieved

with Silicon-on-Insulator (SOI) wafers.

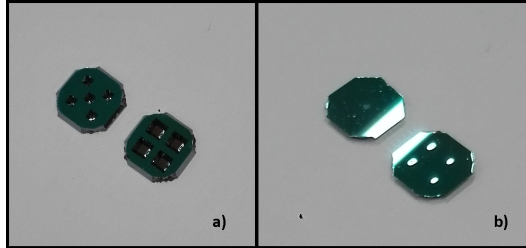


FIGURE 3.1: a) Picture of the suspended Silicon membrane from a) bottom view and b) top view.

Figure 3.1 shows pictures of SOI chips in which Si membranes were designed by etching a) bottom view and b) top view. The membranes were designed with different areas. There are 5 membrane sizes around  $70 \times 70 \mu\text{m}$  on the left a) and 4 membranes were made around  $130 \times 130 \mu\text{m}$  on the right b). The membranes were fabricated at the national Center for Microelectronics (CNM) using a recipe developed by us. Briefly it consisted in depositing a layer of silicon nitride that would be used as a wet-etching mask, photolithography to followed by reactive ion etching (RIE) of silicon nitride to define the windows in which the membranes would be placed, and finally wet potassium hydroxide etching (KOH) to remove the handle of the SOI wafer. The Si oxide (box) can then be removed using a hydrogen fluoride (HF) solution. This leaves the so call silicon (a few micrometers thick) membranes suspended.

As a final step, circular hole were carved in the membrane with a Focused Ion Beam (FIB). Several sizes were first used but finally we settled for holes with diameters of  $10 \mu\text{m}$  and  $20 \mu\text{m}$ . Figure 3.1 b) shows a picture taken with scanning electron microscope (SEM) of one of the holes.

In the next step, the selected 2D material is picked up from a substrate in which it was exfoliated, or directly exfoliated on a stamp, and subsequently transferred on top of the hole.

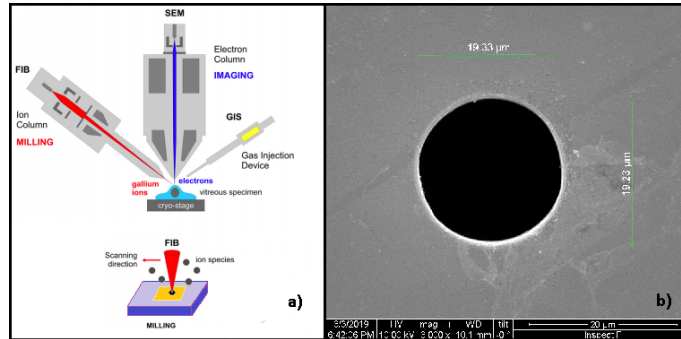


FIGURE 3.2: a) Schematic representation of the FIB [82] and b) SEM picture of a hole in the Silicon membrane.

### 3.1.3 Transferring of 2D materials onto the membranes

Several transfer techniques were used in this thesis. Some of them are novel while others were adapted from techniques in the literature. The main goal was to design and fabricate heterostructure based on the stacking of 2D materials. It is possible to control the position and so create complex van der Waals heterostructures based devices which can lead to novel phenomena. The most common technique for stacking is the all-dry transfer method that involves a viscoelastic stamp and wet chemistry step.

**Transfer set-up.** To transfer exfoliated 2D materials, an optical microscope with XYZ stage was used to find the flakes, characterized roughly their thickness and then aim to the location of transfer. The second part is the stamping stage that can also move in different directions. A glass slide is attached to the stamping stage with the viscoelastic stamp with materials on top.

If the exfoliation of the flake was not implemented directly on a transferred stamp then there is an additional step consisting of picking up the materials from a substrate by either etching or stamping. The foregoing section summarizes the different types of transfer.

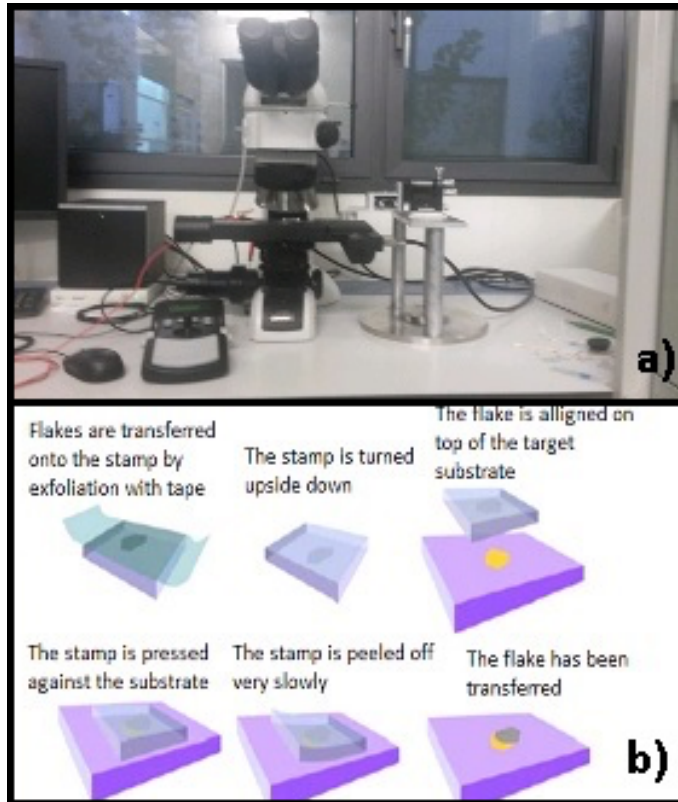


FIGURE 3.3: a) On the right, picture of the Nikon with the stamping stage and the left. b) Utilization of viscoelastic stamping technique.

**Transfer using PDMS, all dry viscoelastic transfer.** The PDMS transfer refers to the technique releasing 2D materials without any added polymer on top [16]. This is the most common technique after exfoliating on top the PDMS transfer the identified flake where it is needed. One issue with this technique is that the polymer is transparent and it is difficult or even impossible to observe thin layers of hBN on top, due to its large band gap (6 eV). Graphene can be glanced with the highest magnification(100X objective) but it is difficult to transfer it at a wanted position.

**Transfer using PDMS, capillary-force assisted transfer.** This transfer technique uses the capillarity force created by evaporating water on top of the PDMS. The problem with this technique is that the flakes may break during the transfer. A more secure way to transfer is then to use a polymer on top of the PDMS.

**PPC or PMMA Transfer.** By adding an extra layered polymer, this technique allows to create clean 2D heterostructure materials. Typically, some 2D flakes are hard to remove from the substrate due to a strong adhesion to it. Fortunately, it is possible to handle the in-between flakes without touching any polymer. This process can be referred as the van der Waals pick-up/transfer with the assistance of, typically, a hBN flake. The larger van der Waals interaction between the 2D material and hBN, allows to remove the flakes from the substrate. This enables the creation of very clean 2D materials heterostructure [76].

There are two highly efficient polymers that can be used on top of the PDMS, Polypropylene carbonate (PPC) and Poly(methyl methacrylate) (PMMA). The difference between the them is their melting point temperature. PPC is employed to pick up graphene from SiO<sub>2</sub>/Si and PMMA can help pick up monocrystals of CVD graphene from copper [5]. In the Appendix C, all steps involved on this technique are described.

**PLLA Transfer.** This transfer method was commonly used for structures with different dimensions and various surface properties [56]. It can be easily transferred on hydrophobic, hydrophilic and flexible substrate.

**Wet Transfer of CVD graphene.** In this case, the CVD graphene is first grown on copper and then transferred with fishing technique on a substrate. This process is described as a wet chemical transfer. It uses PMMA as a temporary support during the etching of the copper by etchants like iron chloride (FeCl<sub>3</sub>), hydrochloric acid (HCl) or ammonium persulfate (NH<sub>4</sub>)<sub>2</sub>S<sub>2</sub>O<sub>8</sub> [57] [49]. The process results in graphene membranes with larger impurities than the dry transfer described above, but it allows much larger flakes and higher reproducibility.

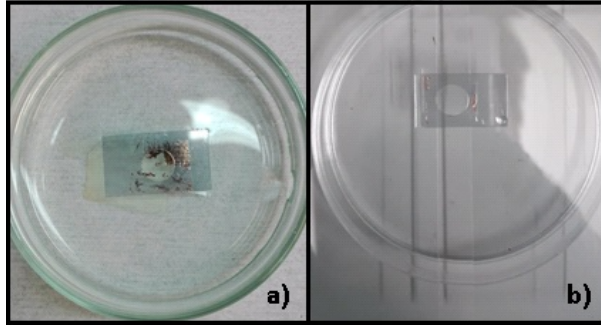


FIGURE 3.4: Picture a) is a stamp of CVD graphene/PMMA/PDMS with hole in the etching solution. b) Dry-etching of the CVD graphene/PMMA membrane

In the case of suspended membranes, some extra steps were added to avoid wet processes. Suspended membranes are very fragile. For example, to remove the PMMA, it is not possible to simply dip the substrate in acetone, because of surface tension when the acetone evaporates, the membranes systematically break. To fix this problem, it is possible to use a Critical Point Dryer. Such system uses the fact that along the boundary between the liquid and vapor phases it is possible to choose a particular temperature and pressure, where liquid and vapor co-exist and surface tension is minimized. Typically the original liquid (in this case water or acetone) is replaced with liquid CO<sub>2</sub> and the temperature then raised to above its critical temperature. When the liquid CO<sub>2</sub> changes to vapour, its density is constant and no tension is generated. Afterwards the gas is pumped away. This technique helps to preserve the sample morphology and avoiding damaging effects [48].

### 3.2 Measurements of Graphene thermal conductivity

In many 2D materials, heat is carried primarily by phonons due to the absence of high density of free electrons. Graphene is a semi-metal and has a strong covalent sp<sup>2</sup> bond between the carbon atoms, also in this scenario, phonons are the main heat carriers. ZA phonons are dominant in thermal conduction for graphene or hBN [58]. This type of phonons dominate the heating transport in the in-plane direction [51]. In order to understand the

thermal transport of graphene, it is important to study the role of different phonons in thermal conduction regime.

The measured thermal conductivity of exfoliated graphene is in the range 3000 - 5000 Wm<sup>-1</sup>K<sup>-1</sup> at room temperature [4], [53]. While graphite has approximately 2000 Wm<sup>-1</sup>K<sup>-1</sup> at room temperature, still among the highest of any known material. However some discrepancies in the thermal conductivity values can be found in the literature for example Faugeras et al. measured a thermal conductivity of 600 Wm<sup>-1</sup>K<sup>-1</sup>. This discrepancy may be attributed to the techniques used to measure thermal conductivity or to the quality of graphene. Nevertheless, thanks to the excellent heat conductivity, graphene has the potential for use in thermal management applications. As previously stated, here we do not focus on exfoliated graphene but on CVD graphene instead, given the promise of large scale production.

Figure 3.5 shows Raman and the thermal maps of 7 μm × 7 μm suspended few-layer CVD graphene obtained by 2LRT. The Raman spectroscopy equipment used for 2LRT is provided by Horiba.

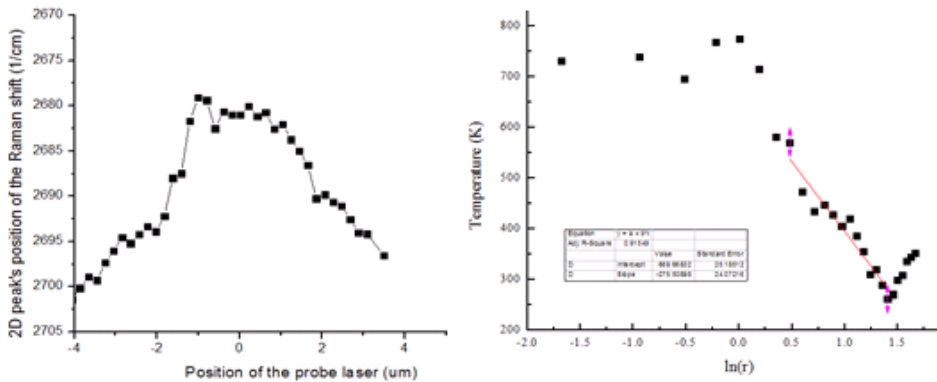


FIGURE 3.5: 2LRT suspended CVD graphene depending on the laser position (left) and temperature conversion based on the logarithm of the laser position (right)



Using the following equation:

$$T(r) = T_0 - \frac{Q}{2\pi dk} \ln\left(\frac{r}{r_0}\right)$$

one can calculate the thermal conductivity of suspended CVD graphene by using these formula:

$$k = \frac{P_{abs}}{2\pi d * Slope\left(\frac{T}{\ln(r)}\right)} = \frac{P_{inc} * 2.3\%}{2\pi(0.34nm) * Slope\left(\frac{T}{\ln(r)}\right)}$$

Where  $d$  is the thickness of the monolayer,  $P_{abs}$  is the power absorbed by the graphene which absorbs 2.3% of the incident power  $P_{inc}$ . The slope of  $\left(\frac{T}{\ln(r)}\right)$  was extracted from the Figure 3.5.

We obtained a thermal conductivity for our suspended CVD graphene of  $305 \text{ Wm}^{-1}\text{K}^{-1}$ , which is lower than in exfoliated graphene as reported in the literature.

This discrepancy could be attributed to quality of the CVD graphene and some polymer residues from the fabrication process. It was also shown that the polymer residues can increase the phonon scattering on the surface [46]. Figure 3.6 evidences the presence of the residues resting on top of the membrane..

The size of the membrane is also an important parameter, and implies that the domain size can have an effect on thermal properties. In an ideal case where only "Umklapp scattering" inhibits heat transfer. Graphene could exceed the bulk limit if the flake domain size is a few micrometers [70]. For suspended pad measurement, the thermal conductivity keeps increasing logarithmically [101]. A theoretical study emphasizes that for a size of  $30 \mu\text{m}$  that would give larger values [69].

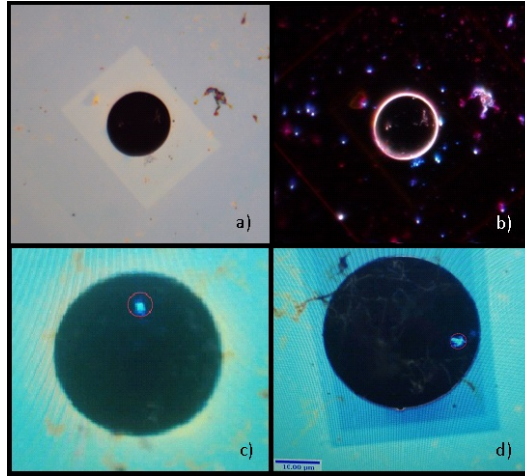


FIGURE 3.6: Optical microscope images after transfer the suspended graphene on a silicone membrane with an of hole of 10  $\mu\text{m}$  a) bright light and b) dark-field mode. Different samples are shown with hole diameter of 20  $\mu\text{m}$  and d) 30  $\mu\text{m}$ .

### 3.3 $\text{MoS}_2$ and $\text{hBN}/\text{MoS}_2$ heterostructures thermal conductivity

Molybdenum disulfide,  $\text{MoS}_2$ , belongs to a class of materials called 'transition metal dichalcogenides' (TMDCs). Due to its suitability for future applications in electronic, piezoelectric and optoelectronic devices [99] [98].  $\text{MoS}_2$  has attracted increasing research interest. The fabrication of few-layer to single layer sample is rather simple with mechanical cleavage technique. Large area are also possible to be prepared by CVD technique [43].

In addition, a tunable bandgap structure in  $\text{MoS}_2$  is relevant for next generation of devices. For example, mono-layer or bilayer of  $\text{MoS}_2$  has a direct bandgap of 1.8 eV [63], it can therefore be used as a nano-transistor channel with an on/off ratio [78]. However, from bilayer to bulk  $\text{MoS}_2$  has an indirect bandgap of 1.3 eV [2] [25]. This thickness bandgap dependence characteristic could hold a possibility for optoelectronic and photo-detection applications [61].

Here, the thermal conductivity of a few layer MoS<sub>2</sub> samples is reported and also one sample measured after the transfer of few layer hBN on a previously tested MoS<sub>2</sub> flake.

Figure 3.7 shows the optical picture of a 4-layer thickness MoS<sub>2</sub> flake on top of 10  $\mu\text{m}$  hole. Two holes can be seen on the picture, in the one on the left the membrane is fully suspended and in the one on the right is broken. Only the perfectly suspended membrane was used. This sample will be referred has SAMPLE A.

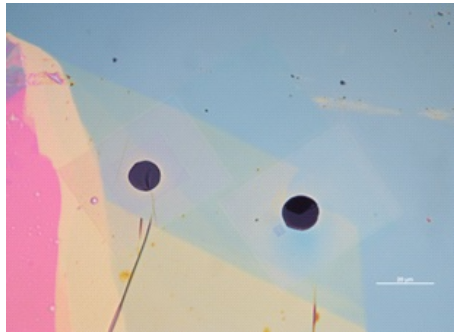


FIGURE 3.7: SAMPLE A - Optical microscope picture of 10  $\mu\text{m}$  suspended MoS<sub>2</sub>

We tried to implement two-laser Raman spectroscopy on this sample. However, we realized that the membrane size was too small to achieve a measurable temperature gradient. This result help us establish a minimum whole size of 20  $\mu\text{m}$  for such measurements. This also implied that very thin flakes were more difficult to suspend over such wholes, and thicker membranes had to be measured. In any case, we used one-laser Raman thermometry as explained in Section ?? . Figure 3.8 shows such measurements from which a thermal conductivity of 23.3 W/(m K) was obtained.

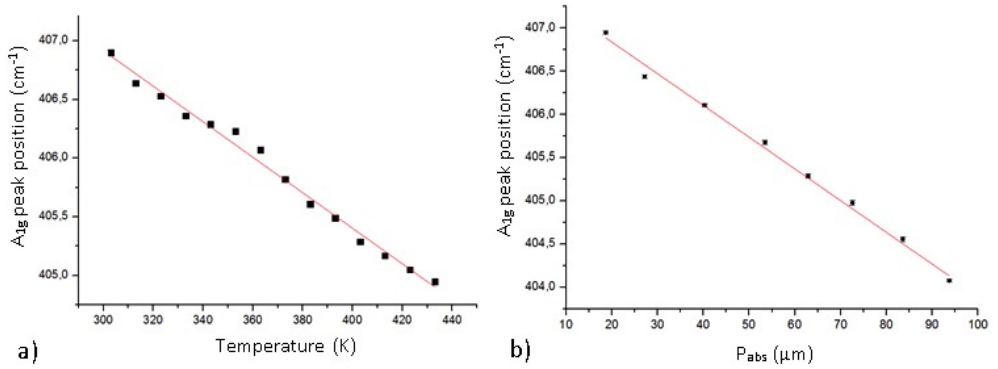


FIGURE 3.8: SAMPLE A - Graphics of 10 $\mu$ m suspended MoS<sub>2</sub>

### 3.3.1 Two laser Raman thermometry of MoS<sub>2</sub>

In subsequent attempts, MoS<sub>2</sub> flakes were transferred onto larger holes in order to achieve larger temperature gradients. Larger temperatures are also achieved by the larger thermal impedance from the center of the membrane to the walls of the hole in which it rests.



FIGURE 3.9: SAMPLE B - Optical microscope picture of suspended 7-layer MoS<sub>2</sub>

Figure 3.9 shows a flake of 7-layer MoS<sub>2</sub> transferred on a 20  $\mu$ m hole. This sample is referenced as SAMPLE B and it was made with simple PDMS transfer technique ( 3.1.3). In this case, with a larger membrane, it was possible to demonstrate the suitability of the 2LRT method [80].

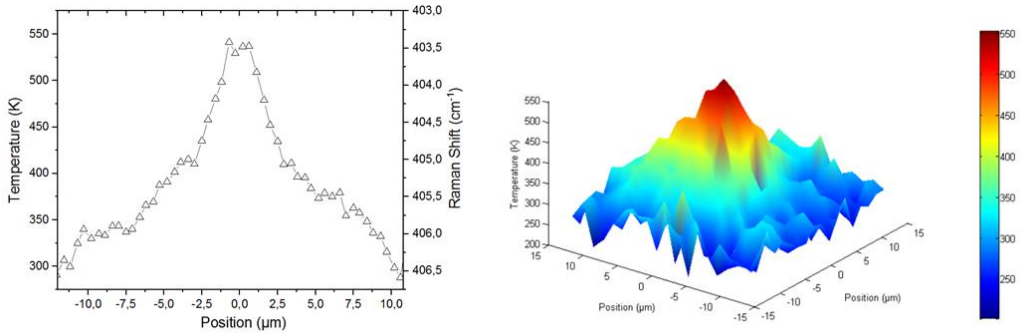


FIGURE 3.10: SAMPLE B - 2LRT scan and 3D map

Figure 3.10 (left) shows the measured temperature increase (left axis) as a function of position, when the heating laser is focused on the center of the membrane. The right axis reveals the Raman shift of the  $A_{1g}$  peak. Here, the heating laser is  $\lambda_h = 405$  nm and the scanning probe is  $\lambda_s = 532$  nm. The heating absorbed power was  $39.8 \mu\text{W}$  measured by different power meters. Figure 3.10 (right) shows a 3D heating map of the same membrane. This measurement reveals that a small wrinkle, which can be distinguished in 3.10, has not a major effect on the thermal measurement. The thermal conductivity of this membrane was estimated to be around  $12 \text{ W/m.K}$ . The model is described in detail in the Appendix A and uses the software COMSOL ® to implement it.

Similarly, a second  $\text{MoS}_2$  membrane was produced on a  $20 \mu\text{m}$  hole (SAMPLE C). In this case the flake had a 20-layer thickness. Figure 3.11 provides the picture of SAMPLE C (a) and the Raman spectra of the  $\text{MoS}_2$  membrane in the top left inset. Figure 3.11 (b) and (c) show 2D maps of the membrane for a laser wavelength of  $\lambda = 488 \text{ nm}$ .

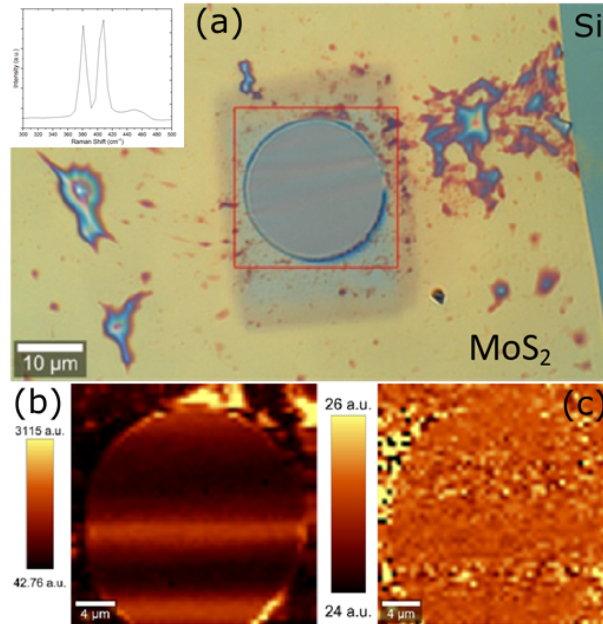


FIGURE 3.11: SAMPLE C - Optical microscope picture of  $20\ \mu\text{m}$  suspended  $\text{MoS}_2$  and 2D Raman maps made with Witec Raman.

Finally, Figure 3.12 shows the 2RLT scan, and is equivalent to Figure 3.10. The signal obtained with SAMPLE C is larger than in SAMPLE B due to the larger number of layer in the former. In this case, the absorbed laser power was also significantly larger  $425\ \mu\text{W}$ . A small asymmetry is distinguished in the thermal scan (left panel) that is due to the laser position not being exactly in the center of the membrane. The position of the heating laser is done manually and the sample is under vacuum. A shift of the order of a micrometer in the laser position off-center is therefore not surprising. The model in the Appendix A supports this hypothesis. The model takes into consideration such a shift and the fit is in a very close agreement with the experiments (Appendix A). The obtained thermal conductivity is  $24\ \text{W/mK}$ .

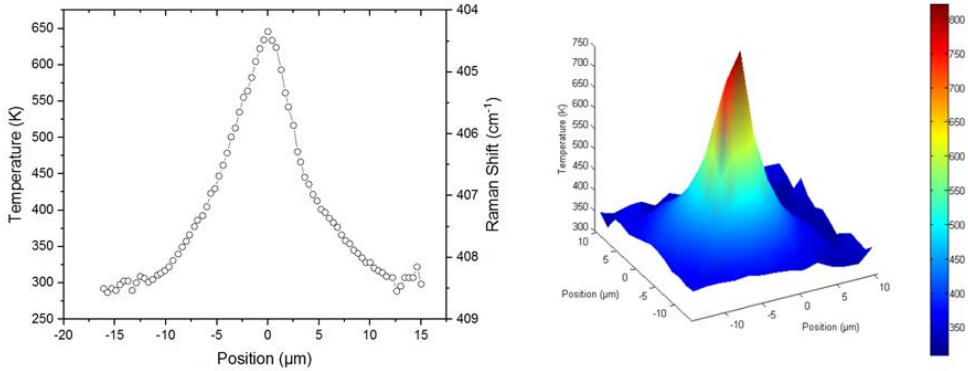


FIGURE 3.12: SAMPLE C - 2LRT scan and 3D map.

### 3.3.2 Two laser Raman thermometry of hBN/MoS<sub>2</sub> heterostructure

Using 2D van der Waals heterostructure new physical phenomenon can emerge including intra-layer phonon modes and inter-layer charge transfer. New phenomena can be observed in such heterostructures that are not found in bulk crystals. Phonons modes can appear due to the vertical bonding and lattice distortion between the 2D crystals [72]. TMDCs have showed layer breathing phonon modes with the support of ultralow frequency Raman spectroscopy Raman breathing modes' intensity are correlated with the suppression of photoluminescence. This results from the interlayer charge transfer. It is important to ensure clean surfaces to observe the layer breathing mode. The orientation between the layers is also very important as the frequency will be impacted. These type of heterostructure are either fabricated by PDMS transfer or generated by CVD growth.

Here we focus on hBN/MoS<sub>2</sub> in order to evaluate the change change of the thermal conductivity of the stack in comparison with MoS<sub>2</sub> alone. Note that photon energy of the laser that heats the sample is lower than the band gap of hBN thus the heat is deposited only on hBN. Therefore a change of the effective conductivity indicates a large conductivity of hBN and an efficient heat transfer from MoS<sub>2</sub> to hBN. In order to make a proper

comparison, the the  $\text{hBN}$  flake was transferred *onto* a previously characterized  $\text{MoS}_2$  membrane (SAMPLE C). We call the  $\text{hBN}/\text{MoS}_2$  stack SAMPLE D. Figure 3.13 shows SAMPLE D, the thickness of  $\text{hBN}$  was determined to correspond to 11-layers. The dash line in Figure 3.13 indicates the perimeter of the  $\text{hBN}$  flake. The top right inset shows the Raman spectra with the characteristic peak of  $\text{hBN}$ . The intensity of the  $\text{hBN}$  peak is found to be less intense than the corresponding ones for  $\text{MoS}_2$  (it was captured with the Witec equipment).

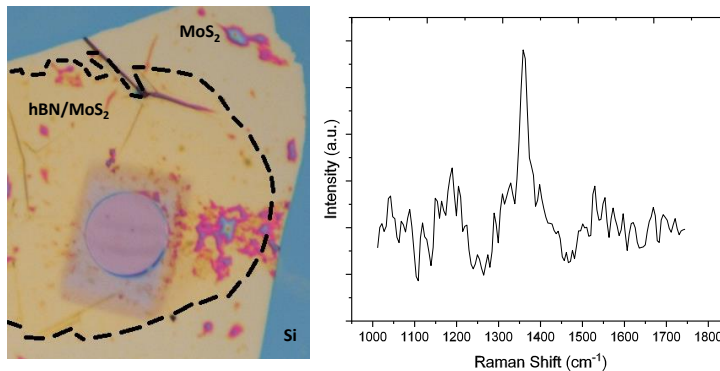


FIGURE 3.13: SAMPLE D - Optical microscope picture of Sample C with a transferred flake  $\text{hBN}$  on top

The 2LRT (Horiba Raman) was then carried out to obtain the thermal conductivity of this heterostructure. Figure 3.14 shows the scans from which the temperature is obtained. Then by using the model described in the A), the measured thermal conductivity was  $185 \text{ W/m.K}$ . For this measurements the input power was increased due to the larger thermal conductivity in the system.

This result demonstrates a significant increase from the thermal conductivity of  $\text{MoS}_2$  to that of the  $\text{hBN}/\text{MoS}_2$  heterostructure. Indeed, the effective thermal conductivity of the latter has increased by a factor 8. This in turn demonstrates the presence of heat transfer from  $\text{MoS}_2$  to  $\text{hBN}$  and the subsequent behaviour of  $\text{hBN}$  as an efficient thermal dissipator. Unfortunately, the temperature of  $\text{hBN}$  could not be resolved, further experiments with more sensitivity on this aspect could be used to map the temperature of both  $\text{hBN}$  and  $\text{MoS}_2$ . In this scenario, it would be possible to



determine the heat transfer between them.

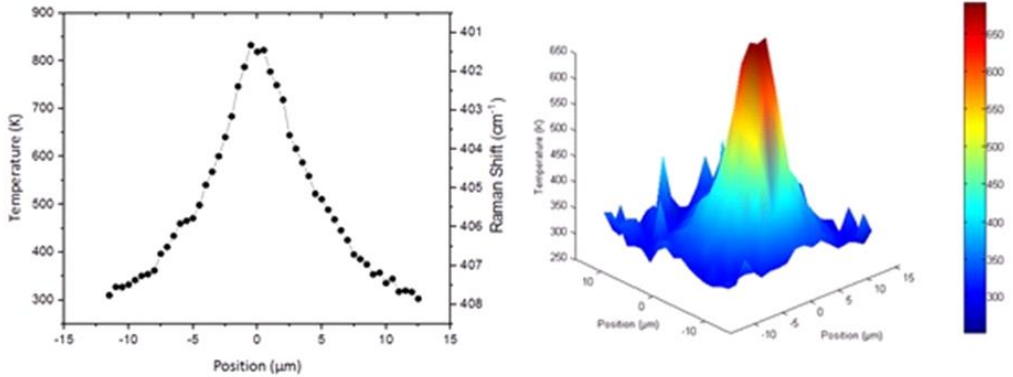


FIGURE 3.14: SAMPLE D - 2LRT scan and 3D map

### 3.3.3 Layer thickness and thermal conductivity

After having determined the thermal conductivity of different membranes, which have different thicknesses, it appears that the thermal conductivity is thickness dependent. The table below summarizes the results obtained with the different samples in this thesis. Using 2LRT, we found that the thermal conductivity is smaller in the thinner membrane ( $k = 12$  W/mK in the 7-layer SAMPLE B versus  $k = 24$  W/mK in the 20-layer SAMPLE C). Prior studies studies have found a reduction of the thermal conductivity of MoS<sub>2</sub> with the decreasing of the number of layers [105].

Note that  $k = 23.59$  W/mK in the 4-layer SAMPLE A does not follow this trend. However, these measurements were carried out with one-laser Raman thermometry (1LRT). As explained in Chapter 2, this method uses one laser to both heat and measure the local temperature of the membrane. As the temperature as a function of position cannot be obviously determined with this technique, then the temperature gradient is unknown. This requires assumptions on the temperature of the membrane in contact with the hole boundary and also the position of the laser. The typical assumption is that the boundary temperature is equal to ambient. However, this depends on the thermal contact between the flake and the substrate.

If the contact is poor and the temperature higher than assumed, then the temperature gradient would be overestimated. In contrast, if the laser is off-centered, the temperature at the center would be smaller than expected. These artifacts are difficult to evaluate and obvious drawbacks of the 1RLT. Whenever possible the 2RLT should be used.

Sample	Nb Atomic Layer	k(W/m.K)	Diameter	Technique
A MoS <sub>2</sub>	4	23,59	10 $\mu$ m	RT
B MoS <sub>2</sub>	7	12	20 $\mu$ m	2LRT
C MoS <sub>2</sub>	20	24	20 $\mu$ m	2LRT
D hBN/MoS <sub>2</sub>	11/20	185	20 $\mu$ m	2LRT

TABLE 3.1: Summary of studied MoS<sub>2</sub> samples

Figure 3.15 shows the thermal conductivity of MoS<sub>2</sub> (black circles) and hBN (red circle) obtained in this thesis in comparison with recent results found in the literature for MoS<sub>2</sub> (left panel) [83] [104] [1] [45] [108] [3] [105] and hBN (right panel) [96] [10] [46]. The comparison permits to conclude that the conductivity of the heterostructure is dominated by hBN. Indeed, the obtained  $k$  in hBN is much larger than any values of  $k$  for MoS<sub>2</sub> and is very similar to the conductivity of a hBN layer of similar thickness. If we take as a reference the thermal conductivity from Insun Jo *et al.*[46] that has the same number of layers, we can recognize a relative small influence of the MoS<sub>2</sub> flake. This observation represents further confirmation that heat transfer from MoS<sub>2</sub> to hBN is very effective.

Figure 3.15 also shows not clear trend in  $k$  as a function of thickness when all the results in the literature are taken into account. However, several of those measurements are carried out with 1LRT, which as explained above, can suffer from artifacts. One could speculate that the scattering of the data might be associated to the measurement technique and inadequate assumptions (such as the boundary condition at the perimeter). The comparison could also suggest that other parameters are in play. For example, the size of the suspended membrane, their quality or the presence of polymer residues, which can have an impact in the reduction or the increase of the thermal conductivity. The scatter of the data calls for

systematic studies that take into account all of these parameters.

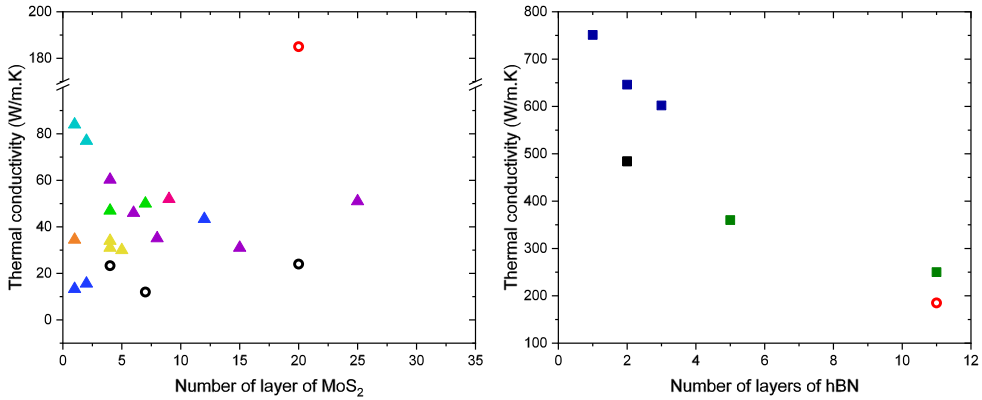


FIGURE 3.15: Thermal conductivity of different number of layer for MoS<sub>2</sub> (left) [83] [104] [1] [45] [108] [3] [105] and hBN (right) [96] [10] [46] layers

### 3.4 Measurements of MoSe<sub>2</sub> thermal conductivity

As a final example of the measurement of thermal conductivity using Raman thermometry [83], we measured the conductivity of a MoSe<sub>2</sub>, another 2D material member of TMDC family which as MoS<sub>2</sub> is a semiconductor. These material exhibits a highly anisotropic thermal behavior, with a much larger thermal conductivity in-plane than out-of-plane [18] but has been barely investigated. At the moment, it is not yet well understood how the thickness of the layer affects the thermal transport. Exfoliation with PDMS and dry transfer were used for fabrication.

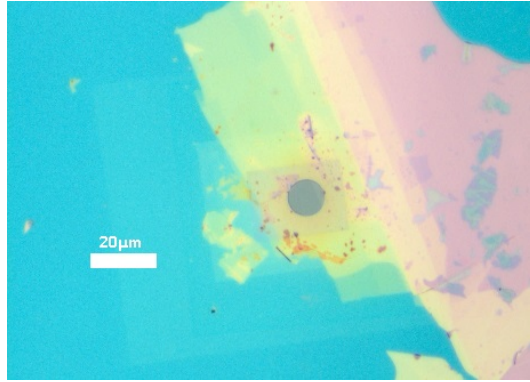


FIGURE 3.16: Optical microscope picture of MoSe<sub>2</sub> suspended 8-layer flake

We could then measure the flake shown in Figure 3.16 which has a thickness of 8-layers. Representation of the experimental results are shown in Figure 3.17. A first measurement was performed to calibrate the MoSe<sub>2</sub> material with the Raman shift of A<sub>1g</sub> peak for the bulk a) and for the suspended 8-layer flake b) depending on the ambient temperature. The Raman spectra of A<sub>1g</sub> peak can actually be seen in 3.17 d). Next, owing to the small size of the membrane, 1LRT was carried out with the increase of the laser power for  $\lambda = 532$  nm while measuring the absorbed power. Using finite element simulations, we could extract a steady state thermal conductivity of  $k=63$  W/(m.K). This value is in close agreement to the obtained in monolayer and bilayer MoSe<sub>2</sub> [108]. However, the dependence of the thermal conductivity on the thickness has never been measured. Yet, some improvements are worth noticing in our experiments: such as a larger suspended MoSe<sub>2</sub> membrane, the measurement being performed in vacuum to reduce the convection phenomenon and, finally, the direct measurement of the power absorbed  $P_{abs}$ .

### 3.5 Summary

In this work, we have developed the process to fabricate suspended 2D materials and measure their in-plane thermal conductivity  $k$ . A large number of transfer methods using different polymers and processes were developed and implemented to maximize the quality of the suspended flake and minimizing the amount of residues to a minimum. We have used both one and two laser Raman thermometry (1LRT and 2LRT). The latter being implemented in small membranes of high thermal conductivity for the first time. Because the local temperature is directly measured, we argue that the determination of  $k$  this technique is more accurate. This will allow therefore systematic investigations of the thermal properties of 2D materials and heterostructures as a function of thickness, interface properties, the component materials and the degree of disorder. As a proof of the capabilities of the 2LRT technique we measured  $k$  of graphene, and of 7-layer and 20-layer MoS<sub>2</sub> resulting in  $k$  equal to 12 W/(m.K) and 24 W/(m.K), respectively, which suggests a larger  $k$  for thicker membranes. There is however a discrepancy in the conductivity of a thinner layer. Indeed, 1LRT measurements resulted in  $k$  of 23.3 W/(m.K) for 4-layer membrane. The discrepancy can be simply due to some inaccuracies of the 1LRT technique. It could also be due to changes in the sample quality and its level of contamination. Unfortunately, during the course of the thesis we could not measure  $k$  using both techniques in the same sample. This is possible in the larger membranes and would have allowed us to carry out an accurate comparison between the techniques and probably help us identify (and correct) artifacts (if any) in the 1LRT method. An additional sample was fabricated in which a 11-layer hBN flake was stacked on top of a previously studied MoS<sub>2</sub> flake. The effective conductivity of the heterostructure increased by nearly a factor 8, when compared with bare MoS<sub>2</sub>. This indicates that hBN is, not surprisingly, an effective material to spread heat and that the transfer of heat from the MoS<sub>2</sub> to hBN is also very effective. This is a promising result to combine TMDCs with hBN for digital electronics.

Further attempts were carried out to obtain large and thin layers of MoS<sub>2</sub> and graphene. The results were mixed, while it was possible to transfer large membranes there were still some residues on top. Figure 3.18 shows the optical picture of a 4-layer suspended flake on a 20  $\mu\text{m}$  hole

after removing the PLLA polymer with acetone, then isopropanol and finally the use of the critical point dryer. Some remaining residues can be seen and will affect the thermal conductivity; these could be identified if thermal gradients are found to be asymmetric. The polymer residues affect the phonon propagation but can also heat up and burn the membrane. This is why the PDMS dry transfer is so far the best even though also leaves some contaminants on top of the 2D material.

It is possible to treat the PDMS in order to have less compounds [42] but this will affect the exfoliation part to have large flakes. In contrast, the main difficulty of the dry transfer technique for large and thin flakes would be due to the interaction with the substrate. The FIB technique helps make the hole but can also contaminate the surroundings. To overcome this difficulty we were able to imprint holes with photolithography and subsequent reactive ion etching. Figure 3.19 shows the optical images of these holes under reflected light a) and transmitted light b).

Finally, we were able to transfer a very thin flake of  $\text{MoSe}_2$  on top of two holes (Figure 3.20) made by photolithography. Unfortunately, the holes were not completely etched which prevent us to performed 2LRT. However, this is a very promising result to obtain large thin membranes of 2D materials suspended.

The above discussion demonstrates that there is room to improve the transfer process and to achieve suspended membranes of a variety of 2D materials to determine accurately their conductivity with the reliable method of 2LRT. This is demonstrated by the several materials that were characterized in this thesis, which hope the door for systematic studies to investigate

heat propagation in heterostructures and for optimizing it for applications.

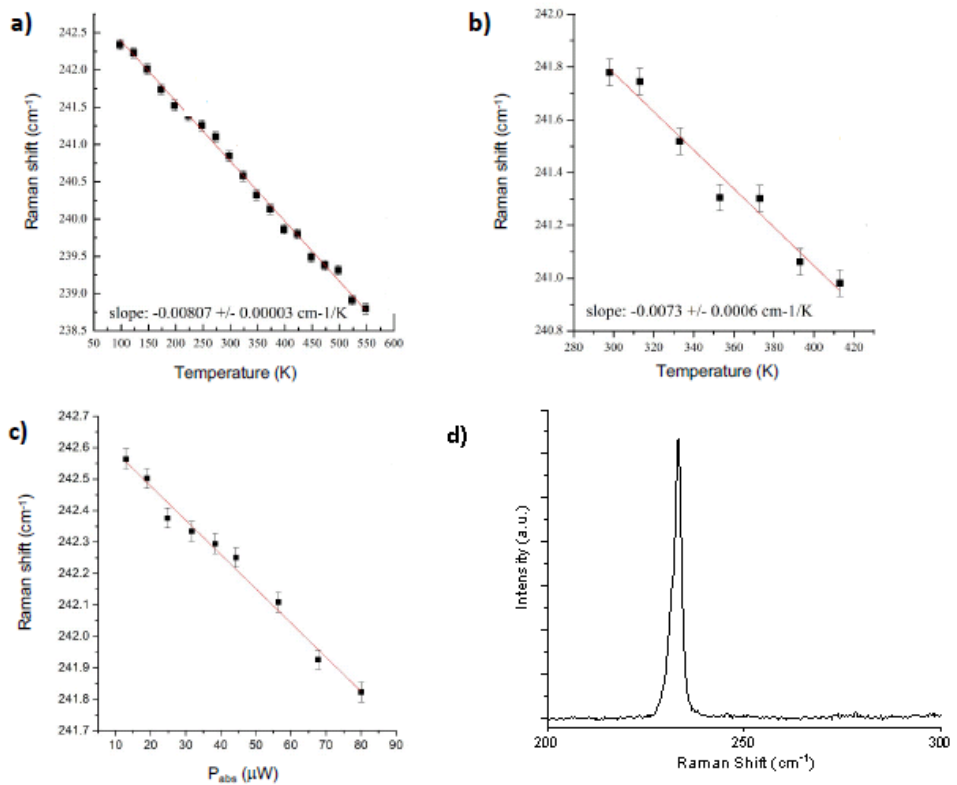


FIGURE 3.17: Raman shift versus temperature for a) bulk or b) suspended MoSe<sub>2</sub> and c) versus absorbed power. d) MoSe<sub>2</sub> Raman spectra



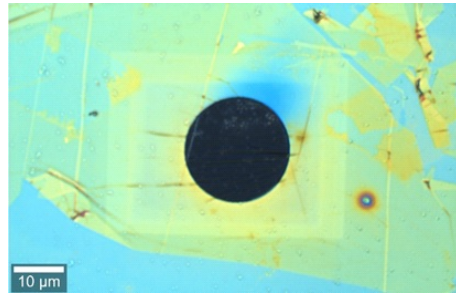


FIGURE 3.18: Optical image of 20  $\mu\text{m}$  suspended 4-layer MoS<sub>2</sub> flake with visible polymer residues

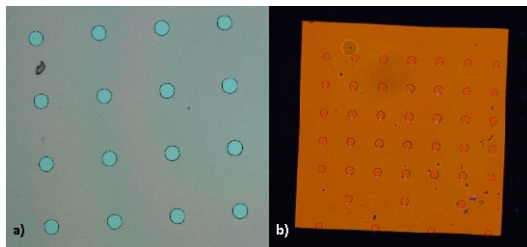


FIGURE 3.19: Optical image of holes made by photolithography under reflection a) and transmission b) mode.

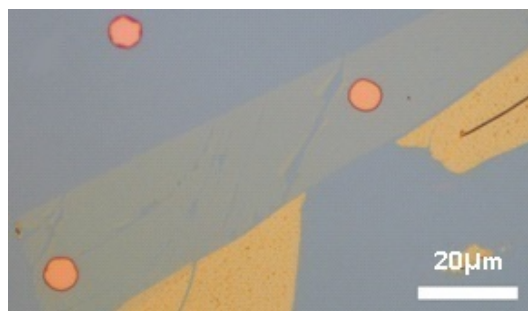


FIGURE 3.20: Optical image of very thin layer of MoSe<sub>2</sub> on top of (around) 10  $\mu\text{m}$  hole.

## Chapter 4

# Thermal expansion and Raman spectra of $(\text{Bi}_{1-x}\text{Sb}_x)_2\text{Te}_3$ alloys

In this Chapter, the Raman spectra of topological insulator  $(\text{Bi}_{1-x}\text{Sb}_x)_2\text{Te}_3$  (BST) are investigated. The films, with variable  $x$ , were prepared by molecular beam epitaxy (MBE) on  $\text{BaF}_2$  substrates, in a chamber fully dedicated to the growth of such films. Details on the film growth and subsequent preparation can be found in Chapter 5. First the Raman spectra of this type of material is introduced. In particular, the temperature dependence of the Raman spectra of BST films with different concentration of bismuth and antimony were investigated. The Raman peaks are observed to shift with the thermal expansion of the alloy due to the temperature change but only active Raman modes are observed. However, as the laser power is increased new peaks develop, which are associated to non-active Raman modes. Such peaks are observed below the threshold at which the films are damaged. Although the origin of the peaks remains unknown, we provide evidence that their study will provide a deeper understanding of the microstructure and vibration modes for this type of thermoelectric films.

### 4.1 Raman Characterization

The Raman active modes of BST films are equivalent to those in  $\text{Bi}_2\text{Te}_3$ ,  $\text{Bi}_2\text{Se}_3$  and  $\text{Sb}_2\text{Te}_3$  alloys. They all correspond to  $R\bar{3}m$  space group with four Raman modes of  $E_g$  and  $A_{1g}$ . The BST alloys differ in the Sb and

Bi concentration and are expressed in term of percentage. In the notation adopted across this thesis, the percentage refers to the amount of Sb, thus  $\text{Bi}_2\text{Te}_3$  is at 0% of Sb to  $\text{Sb}_2\text{Te}_3$  at 100% of Sb.

Figure 4.1 (a) is the crystal representation of  $\text{Bi}_2\text{Te}_3$ . The reason why the Raman modes are not modified with Sb concentration is that Sb atoms directly substitutes the Bi atoms in the lattice. The primitive unit cell contains five atoms which is going to give 15 lattice vibration modes [81]. At the Brillouin zone,

$$\Gamma = 2A_{1g} + 3A_{1u} + 2E_g + 3E_u$$

where there are 3 acoustic phonons  $A_{1u} + E_u$  and 12 optical phonons

$$2A_{1g} + 2A_{1u} + 2E_g + 2E_u$$

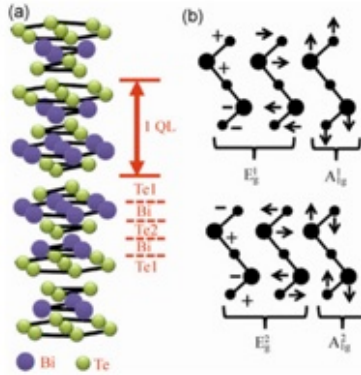


FIGURE 4.1: (a) Crystal structure representation of  $\text{Bi}_2\text{Te}_3$  and (b) Raman active modes of  $\text{Bi}_2\text{Te}_3$  [97].

Figure 4.2 show the Raman spectra for specific Sb concentrations using a laser power of 250uW. At this power laser heating effects are observed to be negligible. In these spectra the Raman active peaks  $E_g^2$  and  $A_{1g}^2$  dare clearly identified. Note that besides  $E_g^2$  and  $A_{1g}^2$ , there are actually 2 other Raman active modes  $E_g^1$  and  $A_{1g}^1$ . However, thee two modes are not observed due to the filter of the laser in our set-up.

The peaks positions were determined by fitting the spectra with Lorentzians (using the software Peak-o-mat). By following their evolution with temperature it is possible to characterize the thermal expansion of these alloys.

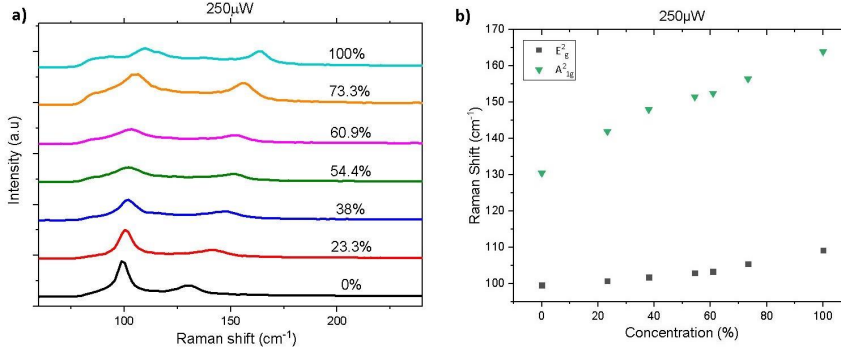


FIGURE 4.2: Two graphics of a) Raman spectra of  $(\text{Bi}_{1-x}\text{Sb}_x)_2\text{Te}_3$  and b) is the peak position of  $E_g^2$  and  $A_{1g}^2$  based on different concentration.

## 4.2 Thermal transport

BST films have long attracted a interest due to their extraordinary thermoelectric properties. Indeed they are some of the best performing room temperature thermoelectrics with a temperature-independent figure-of-merit, ZT, of about 1.0 in bulk form. Furthermore, reports in thin multilayer systems claim ZT values of up to 2.4 Besides being excellent thermoelectric materials, it has been recently demonstrated that BST films can also be topological insulators (TI). The TIs are characterized by being insulating in the bulk and by having robust metallic surface states. The latter being a consequence of the band topology of the material. The presence of the surface states was not taken into account in the original thermoelectricity studies on these materials. Because they can play a dominant role in determining their transport properties, specially when the films are thin, it is necessary to revisit the interpretation, and perhaps origin, of the large ZT values. Several studies predict that the contribution of the surface states can have an impact on the electrical transport which would lead to further

improvement on the ZT. Changes in the efficiency can be due to the reduction of the thermal conductivity depending on the surface phonon dispersion and the quantum confinement. Thus, it is first necessary to investigate the effect of the temperature on the material.

#### 4.2.1 Thermal expansion

The measurement was performed with the Witec Raman Spectrometer under vacuum to avoid heat convection. On top of microscope stage a cryostat was placed that allowed us to control the sample temperature. The evolution of the Raman  $E_g^2$  peak in MBE-grown BST was investigated as a function of temperature for several Sb concentrations and a film thickness of 10 nm.

The  $E_g^2$  is more intense than the  $A_{1g}^2$  one and its position can be determined more precisely. Figure 4.3 shows the Raman shift as a function of temperature, from 300 to 480 degrees Celsius. In this temperature range a linear decrease is observed with temperature, with a slope that is largely independent of the Sb concentration. The laser power was 200  $\mu\text{W}$ , the acquisition time was 120s, for a laser wavelength of 488nm.

The slope values are listed in Table ???. As a reference, the results from Duanhui Li *et al.* are also shown. Note that the thermal expansion in those samples are similar even though they are orders of magnitude thicker (around 4  $\mu\text{m}$ ) and they have used a laser with wavelength of 533 nm.

Concentration of Sb (%)	Thermal expansion $\text{cm}^{-1}/\text{K}$	Reference
0	-0,0169	In this work
23,3	-0,0154	In this work
60,9	-0,0171	In this work
73,3	-0,0236	In this work
100	-0,0197	In this work
0	-0,0137	[55]
75	-0,0156	[55]

TABLE 4.1: Thermal expansion values of BST films for different concentration

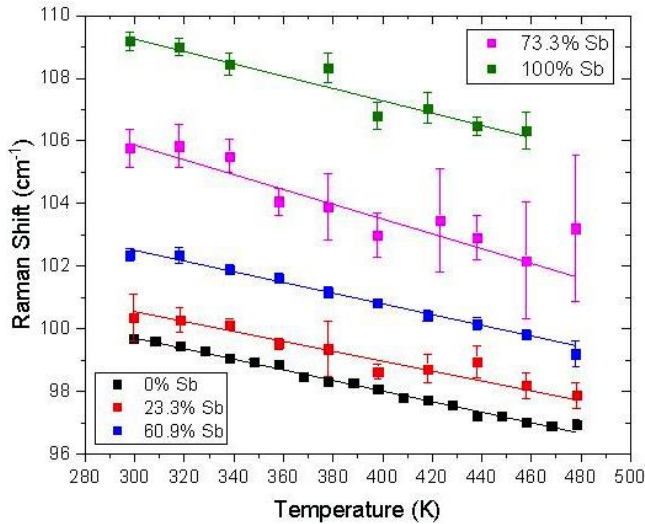


FIGURE 4.3: Temperature dependence of the  $E_g^2$  peak position of BST films.

#### 4.2.2 Determination of the absorption coefficient

Here we investigate the dependence of the reflectance and the transmittance of the light in our films as a function of wavelength in the visible region. Figure 4.4 a) shows typical film transmittance and reflectance results for the indicated Sb concentrations. The curves close to 0 are the measured transmittances and those around 0.3 to 0.6 are the measured reflectances. Figure 4.4 b) shows reference measurements using the bare  $\text{BaF}_2$  substrates (with no films grown onto them). Various substrates were used to calibrate the absorption of the films.  $\text{BaF}_2$  is a salt-like type of substrate, which is transparent and does not absorb light. However, Figure 4.4 b) shows that the transmittance is well below 1, which means that the light is partially scattered and reflected.

Figure 4.5 is a schematic representation of the different  $\text{BaF}_2$  substrates investigated. The first one is double side polished and is expected to present a large transmission and an absorption close to 0. The films were grown on

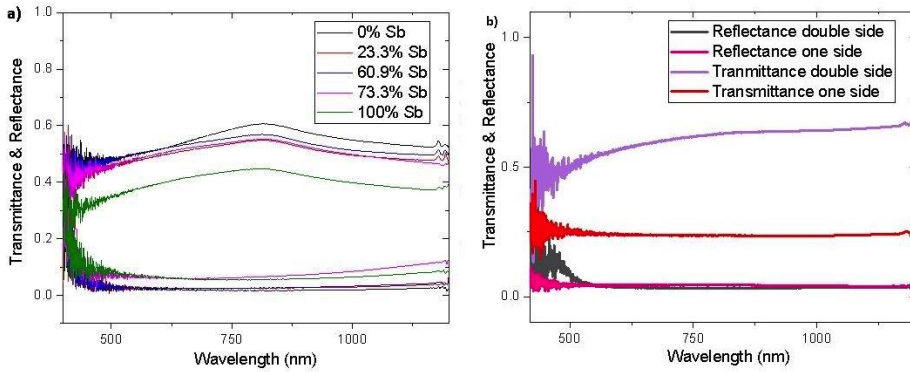


FIGURE 4.4: a) Reflectance and Transmittance of the films for different concentration. b) Reflectance and Transmittance on reference  $\text{BaF}_2$  substrates.

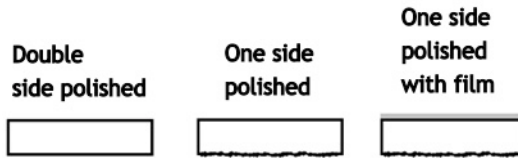


FIGURE 4.5: Schematic different  $\text{BaF}_2$  substrate.

one side polished substrates that scatter the light and reduce the transmission. It is observed that even though the double side polished substrate has a better transmission than the one side polished, in both types of substrates the transmission is significantly suppressed.

Once thermal expansion parameter is known, the thermal conductivity could in principle be obtained. This would allow the determination of the temperature profile as a function of laser power. For that, the absorption coefficient of each film is required. The reflectance and transmittance will give the absorbance and the absorbance is linked to the absorption of the material. Unfortunately, because of the uncertainty introduced by the substrate light scattering, it has not been possible to precisely determine the absorption and therefore the thermal conductivity of the films.

### 4.3 Evolution of the Raman spectra with laser intensity

Even though the thermal conductivity is unknown, it is still possible to investigate the evolution of the Raman spectra when the laser power increases and deposits heat at a localized position. Below  $500\mu\text{W}$  the spectra remains largely unchanged. Notably, once laser power is increased to  $500\mu\text{W}$  additional new peaks start to appear for  $\text{Sb}_2\text{Te}_3$ . They can be seen in Figure 4.6 and they are numbered from 1 to 5.

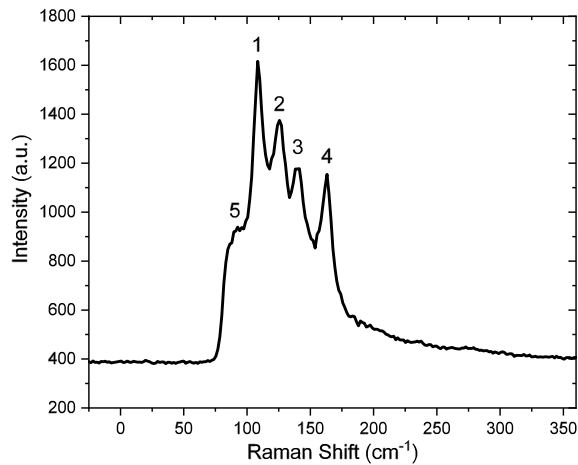


FIGURE 4.6: Raman Spectra of  $\text{Sb}_2\text{Te}_3$  for a power of  $500\mu\text{W}$ .

Similar behaviour is observed for different Sb concentrations, however, the dependence on laser power is strongly material dependent. As observed in Figure 4.7, the additional appearance of peaks and their intensity are strongly dependent on Sb concentration are appearing for the different laser power. While the peaks in  $\text{Sb}_2\text{Te}_3$  are well developed at  $500\mu\text{W}$ , they are not observed in any of the other concentrations with the same power. For the films in which the Fermi level is within the bulk gap (54.4%), the peaks are only distinguished in the  $3000\mu\text{W}$  measurements;  $\text{Bi}_2\text{Te}_3$  (0% Sb) never develops new peaks.



The laser power at which the crystal structure is affected or changed is also material dependent. Such changes are identified by the appearance of irreversibility when the power is cycled. For  $\text{Sb}_2\text{Te}_3$ , and a laser wavelength of 488nm, the threshold is below  $2000\mu\text{W}$ , after which the material is damaged and the low-power spectra is never recovered. For the other concentrations, the irreversibility arises beyond  $3000\mu\text{W}$ , at  $4000\mu\text{W}$  the films are clearly damaged (burnt). The damage can be seen directly with naked-eye as a black spot on the material.

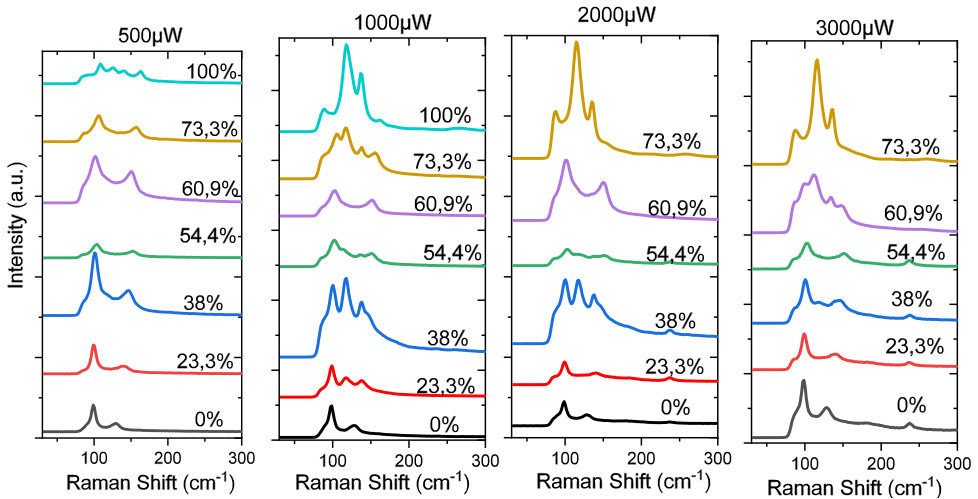


FIGURE 4.7: BST Raman Spectra for different concentration at  $500\mu\text{W}$ ,  $1000\mu\text{W}$ ,  $2000\mu\text{W}$  and  $3000\mu\text{W}$ . The region around  $80\text{cm}^{-1}$  is not shown due to the laser filter cut off.

The evolution of the Raman Shift at the different power and material are summarized in Figure 4.8, Figure 4.9 and Figure 4.10 for a laser power of  $500\mu\text{W}$ ,  $1000\mu\text{W}$  and  $2000\mu\text{W}$ , respectively.

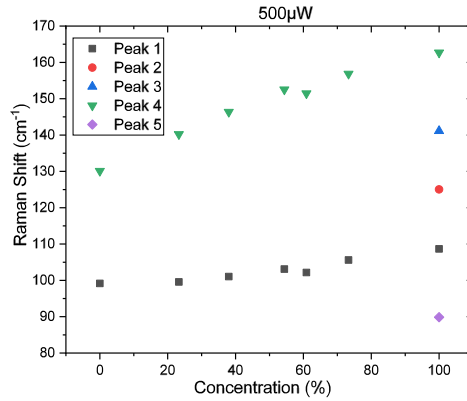


FIGURE 4.8: Raman Shift position for different concentration at  $500\mu W$ .

The increase of the laser power at  $1000\mu W$  reveals the new peaks for all the concentration of Sb expect at 0% Sb. In Figure 4.9 the red circles represents peaks that are "shoulder" of another peak next to them with a higher intensity. These peaks can be fitted even though they are not clearly expressed. The purple circle is the dispersion of the  $E_g^2$  peak (Peak 1) could be to the advantage of the identified  $A_u$  peak (Peak 2).

The extinction of the  $E_g^2$  is using a first sign for non reversibility. At this power for  $Sb_2Te_3$ , it is still reversible but for higher ones it will not be the case. The Figure of 4.10 is the Raman Shift position for different concentration without 100% Sb because the film is already damaged.

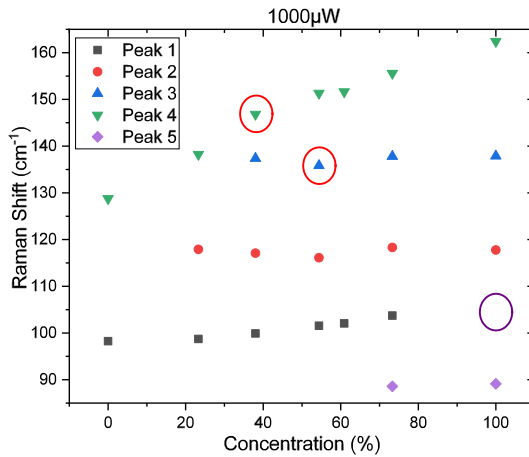


FIGURE 4.9: Raman Shift position for different concentration at  $1000\mu\text{W}$ .

Once again, Figure 4.10 is the Raman Shift position at  $2000\mu\text{W}$  where peaks appeared and others disappeared. The purple circle represents the extinction of some peaks in favor of others. At 73.3% Sb, the new peaks took over Raman active mode peaks found in lower power. The green circle is there to represent the idea that at 23.3% Sb Peak 3 and Peak 4 could be at the same position. It is then impossible to distinguish which one there is. On another hand, it is also interesting to point out that the band gap is changing with the concentration.

The Raman spectra expression of the BST films for different powers have shown the appearance of new peaks in favor of normal Raman-active modes. So now it is also possible to change other parameters that can have an effect the Raman Spectra. Figure 4.11 is the Raman spectra for variable laser focus at the previous studied laser power for a concentration of 73.3% Sb. The change in the laser focus impacts the development of the new peaks. The spectra in previous figures were obtained in the focused situation, implying maximum power density, which will be referred as the 0 position. As the stage changes the focus position, say to  $0.5\mu\text{m}$ , the spectra evolves due to the change in power.

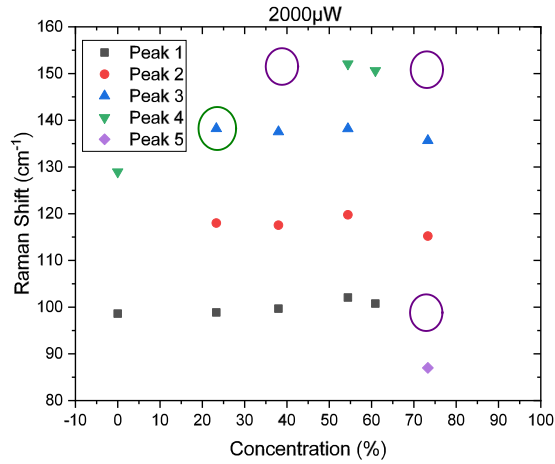


FIGURE 4.10: Raman Shift position for different concentration at  $2000\mu\text{W}$ .

The measurement were performed by first increasing the z-position. Then in a second part, the z-position was decreased and focused more on the substrate. It is possible to see the peak of the  $\text{BaF}_2$  increase with the reduction of z-position. At  $1000\mu\text{W}$ , the 0 position the new peaks show maximum intensity. But once the position is increased or decreased, taking the laser out of focus, the intensity of the Raman active modes are clearly dominant. Once the laser focus is far enough, the new peaks disappear.

At  $3000\mu\text{W}$ , the film starts to burn and the Raman is no longer reversible. It is enticing to modify the laser wavelength. Figure 4.12 repeats the above experiments but with a wavelength of  $633\text{nm}$ . The z-position variation changes is  $1\mu\text{m}$  and the two new peaks start only to appear at  $3000\mu\text{W}$  and for that particular case, the film is not damaged.

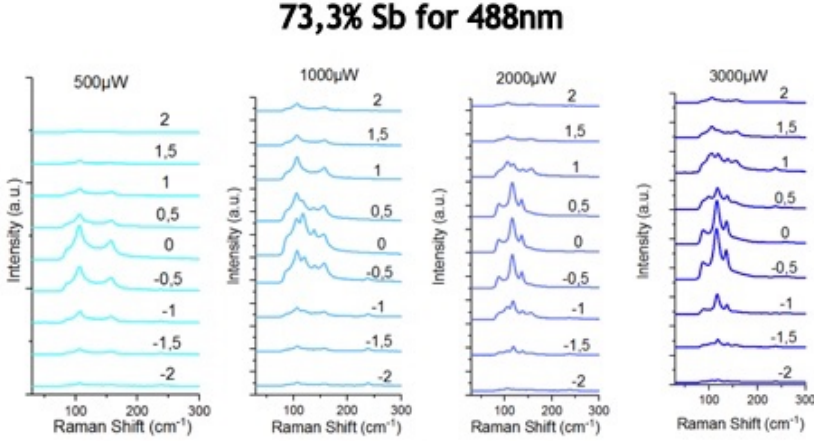


FIGURE 4.11: Raman Spectra for distinct z-position laser focus and for a wavelength of 488nm at  $500\mu\text{W}$ ,  $1000\mu\text{W}$ ,  $2000\mu\text{W}$  and  $3000\mu\text{W}$ .

## 4.4 Discussion

The new Raman peaks observed in our experiments are most likely deriving from Infrared Raman modes. Indeed, they can be identified as [81]: 1:  $E_g^2$ ; 2:  $A_u$ ; 3:  $A$ ; 4:  $A_{1g}^2$ ; 5:  $E_u$ . These new vibrational modes can originate from quantum size effects and symmetry breaking of the crystallographic structure. For higher laser power, the symmetry breaking of the structure will happen when the Raman spectra are no longer reversible. However, it is still surprising the fact that the same peaks are observed even though no irreversibility is detected.

Chunxiao Wang *et al.* [97] observed new vibrational modes by changing the layer thickness of their  $\text{Bi}_2\text{Te}_3$  films and interpret their observations as being related to surface phonon modes. For very thin two quintuple layer (QL), they observe a shoulder on the  $E_g^2$  peak which they attribute to surface phonons, which occur at the surface of solids for structural abrupt crystal termination. These type of phonons can give important amounts of information on surface relaxation but also on the quantity and type of defects present in the surface. The surface phonons are important since they can couple with electrons thus impact the electrical and optical properties

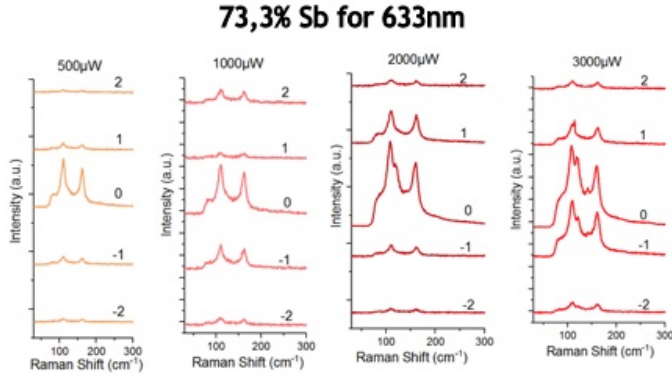


FIGURE 4.12: Raman Spectra for distinct z-position laser focus and for a wavelength of 633nm at  $500\mu\text{W}$ ,  $1000\mu\text{W}$ ,  $2000\mu\text{W}$  and  $3000\mu\text{W}$ .

of semiconductor devices. In our case study, the films are around 10 QL. It is then hard to associate the arising new peaks to surface phonons. Surface phonons can also appear at lower temperature due to the symmetry breaking [9] or with the presence of surface carrier pockets. This also suggests the possible existence of density waves of surface charging and associated collective electron excitations including phasons and amplitudons [14].

Crystal symmetry breaking has been taken into consideration to explain the presence of similar modes [6] in several reports. Shahil *et al.*[88] found that  $\text{Bi}_2\text{Te}_3$  presents a phonon mode  $A_{1u}$ , which is not Raman active. They also calibrate the intensities ratios  $I(A_{1u})/I(E_g^2)$  and  $I(A_{1g}^2)/I(E_g^2)$  that they correlate to the number of QLs. Furthermore, German *et al.*[31] observed new Raman modes for  $\text{BiSbTeSe}_2$ , from 6K to room temperature, and associated them to a local inversion symmetry breaking space group going from  $R\bar{3}m$  and locally turning into  $R3m$ .

In our experiment, the change in concentration is to perform band engineering to reduce the bulk transport in the topological insulator. The aim is to achieve dominant transport at the surface states and a strong insulating bulk (Chapter ??). Figure 4.7 shows the different Raman spectra indicating

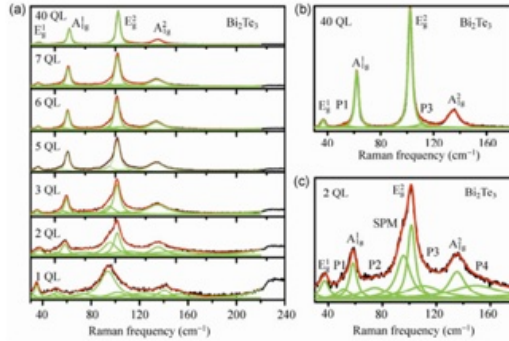


FIGURE 4.13: Raman spectra of  $\text{Bi}_2\text{Te}_3$  for different thicknesses [97].

that the intensities and the peaks are impacted differently by the concentration of Sb. With already these previous studies it is interesting to point out the affect by the phonons and the electrons and their interaction electron-phonon. That interaction could lead to anomalies in the observed Raman spectra.

In the work of Bera *et al.*[7], some form of pressure is used to create a transition from band to topological insulator in  $\text{Sb}_2\text{Se}_3$ . So, the pressure is going to induce a sharp change in the electronic topology which can impact the electron-phonon anomalies seen in the Raman spectra. Conducting surface state on 3D TIs were investigated by helical Raman scattering for  $\text{Bi}_2\text{Se}_3$  [33]. The impact of the surface conductive states are masked by the bulk contribution. Electronic surface contribution could be observed by electronic resonance and symmetry constraint in the case of the Raman scattering. These two previous experiments can be expressed by the theory of surface optical and Raman conductivity [85]. It is difficult to measure the surface conductivity effect due to the fact that the bulk electrons are also going to contribute to the conductivity.

So, let's take  $\Delta_g$  the inverted band characteristic of TI and  $\mu$  the chemical potential. If there is  $\mu > \Delta_g$  then both the bulk and the surface conduct, the main contribution will be given by the bulk. For the case of  $\mu < \Delta$  the bulk will have no effect and the conductivity will be given by the gapless

surface states. Raman scattering can then be a good technique to evaluate the surface conductivity. For that to happen the laser frequency must be smaller than the TI gap and larger than the chemical potential. That give the following relation  $\Delta_g > \delta_g > \mu$  where  $\delta_g$  is the frequency of the laser.

Here, the laser wavelength is 488nm, converted it is 2,54 eV which is much larger than the gap, that is around 0,3eV. The conditions are there to cancel the bulk contribution. It can also be found that the different Raman spectra do not have any background noise that could be representative of a metallic behavior.

The surface and the interface of the films are probed by the Raman scattering. In the their experiment Humlicek *et al.*[40] studied the modification of the surface by intense illumination. The exciting laser light affects the accumulation of the tellurium at the surface. However in this study, the spectra can have new peaks and be reversible, thus the peaks are not likely related to changes in the Te distribution. The penetration depth of the light is important in this context for this type of films. They used spectroellipsometric measurements to obtain response functions.  $\text{Bi}_2\text{Te}_3$  and  $\text{Sb}_2\text{Te}_3$  are interesting elements for optical properties from ultraviolet to near infrared. The light absorption can be linked to plasmonic resonances related to the excitation of free charge carriers and dielectric Mie resonances based on optical interferences [94]. The dielectric function is express by  $\epsilon = \epsilon_1 + i\epsilon_2$ . For topological insulators  $\epsilon_1$  value is negative. Their resonance was initially called plasmonic. However, the resonance is not caused by the excitation of free charge carriers but by the excitation of strong interband transitions, maybe with the conducting states of the TIs for some cases. More experiments like the ellipsometric measurement will be needed to help understand the true nature of these modes and maybe their role for other properties such as thermal transport.

## 4.5 Summary

In this chapter, the thermal expansions of  $(\text{Bi}_{1-x}\text{Sb}_x)_2\text{Te}_3$  films was investigated together with the evolution on Sb concentration. When the laser power was increased over certain threshold, which is Sb-concentration dependent, non active Raman modes developed. The modes are observed in a range of power where no irreversibility appears, thus no damage in the



films is detected. Below we summarize the different parameters that are relevant for the observation of this fascinating new physical phenomena

- The Sb concentration has an impact on the Raman spectra. Even though at low powers the observed peaks are equivalent in all films, the peaks appear at different powers depending on Sb concentration.
- Z-plane focus height could be changed and is revealing or not the infrared modes, which also is well explained by the local laser intensity.
- The laser wavelength affects the development of the new modes probably due to the difference in terms of absorption.
- The electronic properties of these compounds appears to be relevant as the peaks are never observed when the Fermi level is tuned in the bulk band gap
- Sb seems to have a primary role, as the nonactive peaks are not observed in  $\text{Bi}_2\text{Te}_3$

Distinct causes has been discussed to explain the appearance of the non-active Raman modes. The laser power could affect the atomic structure of the films changing the crystal symmetry. However, this process can be discarded, as it is likely irreversible. At low thickness surface phonons or some contribution of the surface conductivity from the complex electronic properties of these compounds. However, the films are too thick for the phonon modes to dominate, while the surface states are dominant when the Fermi level is in the band gap, a situation in which the peaks disappear. The Raman line shape can be affected by the mass gap. Therefore, Raman scattering technique could give possibilities on topological properties of TIs and be complementary to ARPES study on the topological protected surface states. More experiments are needed to understand how the light is absorbed by the films, how the concentration and the electronic surface states could have an impact or not on the revelation of these new Raman modes.

## Chapter 5

# Seebeck measurement of $(\text{Bi}_{1-x}\text{Sb}_x)_2\text{Te}_3$ alloys

This chapter explores the thermopower measurements of 3D topological insulator,  $(\text{Bi}_{1-x}\text{Sb}_x)_2\text{Te}_3$ , thin films with different Sb concentrations. Recent evidence suggests that by tuning the Sb composition topological insulators with ultra-low carrier concentration and surface dominant transport can be grown. When the Sb composition is about 60%, the bulk electron density is reduced and the electrical transport is dominated by surface states. While various experiments were based on the electrical transport and spectroscopic methods, only two studies have attempted to investigate the surface states' contribution to the thermoelectric effect. Thus, there is very little scientific understanding of the topological coupling to the thermoelectric effect. The major objective of this study was to investigate this coupling. The final chapter of this dissertation is divided into two parts. The first part deals with the BST growth process, followed by electrical transport, Hall effect, and angle-resolved photoemission spectroscopy (ARPES) characterization. The second part moves on to describe in greater detail the thermopower measurements in specially designed devices at selected Sb concentration, as a function of temperature.

### 5.1 Growth characterization

Molecular beam epitaxy (MBE) is the selected growth method. MBE allows full control of the thickness and composition of the material, therefore allowing it to address the influence of bulk carriers. The growth is carried

out in ultrahigh vacuum (UHV) and using ultra-pure materials (6N purity). The base pressure of the chamber is in the range of  $10^{-10}$  mBar.

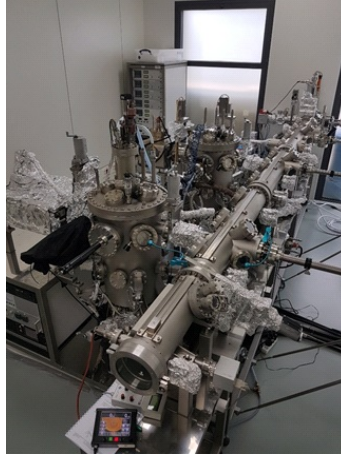


FIGURE 5.1: Picture of the Molecular Beam Epitaxy system.

The MBE chamber own by the PEND group has two reactors. One is fully dedicated to the growth of TIs, with effusion cells of Bi, Sb, Se, and Te. The other combines effusion cells and electron-beam evaporators. This reactor is used for low-vapor pressure materials (Al, Co, Py Al) and insulators (MgO, EuS), etc. The chambers are connected with a UHV transfer chamber, thus films grown in one chamber can be transferred to the other without breaking vacuum. This is used for example to protect TI films from oxidation. It has been found that 2 nm of Al, which forms aluminum oxide when exposed to air, protects the surface of the TI efficiently.

For the films used in this thesis, the growth and parameter calibration were performed by Dr. Frederic Bonell and Dr. Adriana Figueroa. The quality and the growth rates of the thin films are characterized in situ using reflection high-energy electron diffraction (RHEED). This method to characterize the films is widespread in the MBE community and is typically the first information that is obtained about the quality of the film. Briefly, for RHEED an electron source is a high-energy electron source is used in combination with a photoluminescent detector. The electron "gun" produces

a beam of electrons that the sample at a relative (small) angle on the surface. The diffraction of the electrons from the surface generates patterns on the detector, which provide information on the surface crystalline properties and the growth dynamics (e.g. crystalline vs poly-crystalline vs textured vs amorphous structure and two-dimensional vs three-dimensional growth). Figure 5.1 shows a typical example for the RHEED for a  $\text{Bi}_2\text{Te}_3$  film.

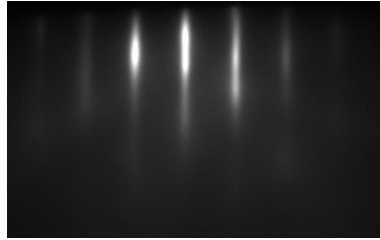


FIGURE 5.2: RHEED pattern for  $\text{Bi}_2\text{Te}_3$ .

The TIs at the PEND group on  $\text{BaF}_2$  substrates are arguably amongst the TIs with best crystalline quality available worldwide. They are characterized by a very small density of structural defects, in particular in regards to planar twins. Twins are large planar defects that are believed introduce bulk doping. Indeed, as discussed below the PEND pristine untwinned films of  $\text{Bi}_2\text{Te}_3$  are only slightly n-doped when with the Fermi level well in the bandgap. Unfortunately, when removed from UHV and after processing the  $\text{Bi}_2\text{Te}_3$  films become highly n-doped (due most likely to band bending or Te out-diffusion due to required heating or etching) and the introduction of Sb is required to counteract such change.

The atomic concentrations of all present elements that form the TI was measured with X-ray photoelectron spectroscopy (XPS), which was used as a means of calibration. After growth optimization,  $\text{Bi}_2\text{Te}_3$  is perfectly stoichiometric and then the growth of TIs with specific Sb concentrations is carried out. As observed in Figure 5.3, the intensity of Bi and Sb peak changes with the film composition which allows to verify the deposition calibration.

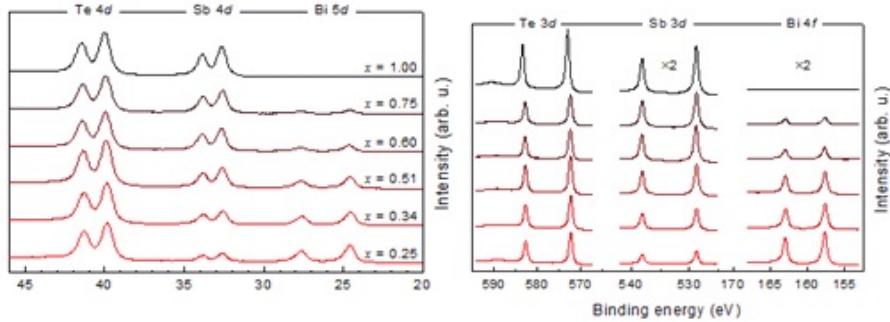


FIGURE 5.3: X-ray photoelectron spectroscopy of  $(\text{Bi}_{1-x}\text{Sb}_x)_2\text{Te}_3$  thin films for different Sb concentrations.

Once the concentration of Bi and Sb is established, the films are studied by means of angle-resolved photoemission spectroscopy (ARPES), which is necessary to carry out band gap engineering and bring the doping concentration down back to minimum values. ARPES allows the observation of the electrons in the reciprocal space to gain information on the energy and the momentum of an electron, and the Fermi surface and band dispersion. ARPES is a surface sensitive technique and, as such, is a very direct method to observe the electronic structure for the surface of solids. Figure 5.4 presents the ARPES results for TIs films with different Sb concentration. As discussed above the Fermi level is well within the bandgap in  $\text{Bi}_2\text{Te}_3$ . The inset shows a detail of the Dirac cone associated to the surface states, which are very well resolved. By simply adding 25% of Sb, the films become highly p-doped.

The films are also characterized using electronic transport both using sheet-resistance and Hall measurements. Figure ?? shows typical sheet-resistance measurements and the evolution from n-type to p-type doping when the concentration of Sb increase.

A drop in the resistance when lowering the temperature is typically ascribed to a metallic behavior (highly doped material). However, around 50% Sb, the slope reverts and the resistance increases with decreasing temperature, which is typically attributed to an insulating behavior. In this case, an incipient maximum and subsequent decrease in the sheet resistance is observed at about and below 100K. The maximum is commonly interpreted as a transition when the surface transport becomes dominant

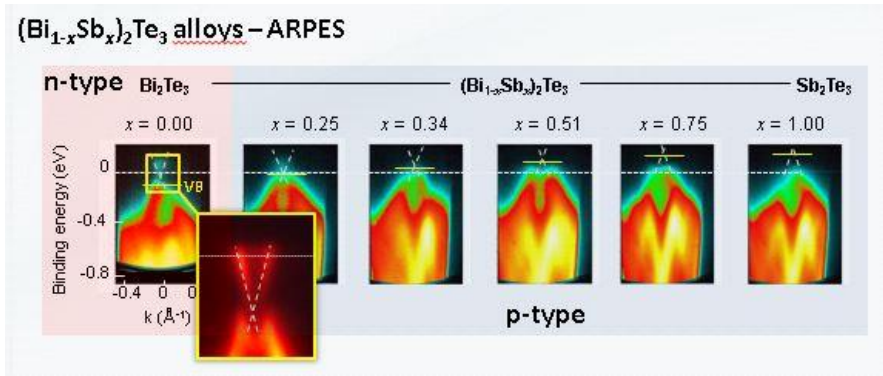


FIGURE 5.4: ARPES measurements of the grown BST films.

against the bulk. At lower temperatures, the decrease in the resistance would then be due to an increase in the mobility of the carriers flowing in the surface. Note that  $\text{Bi}_2\text{Te}_3$  behaves as a metal and that the change from n to p doping occurs at much higher Sb concentrations than those deduced from ARPES. As mentioned above, when the films are removed from UHV and processed into devices, the doping level changes dramatically making necessary the characterization with transport, ideally in the devices identical to those designed for other experiments (e.g., thermal or thermoelectric).

## 5.2 Nanofabrication process

To measure the thermoelectric properties of the TIs, and obtain their corresponding Seebeck coefficients, it is necessary to develop specific nanofabrication protocols. These thermoelectric devices require the fabrication of heaters, and thermometers to generate and measure, respectively, temperature gradients. Their implementation has to be compatible with electronic transport and Hall devices. A key objective is to fabricate devices for all of these purposes, during the same process, using different regions of the same TI films. This approach ensures the most accurate determination possible of the carrier nature, density (the Fermi level position) and mobility, which will later on help interpret the thermopower results and the trends

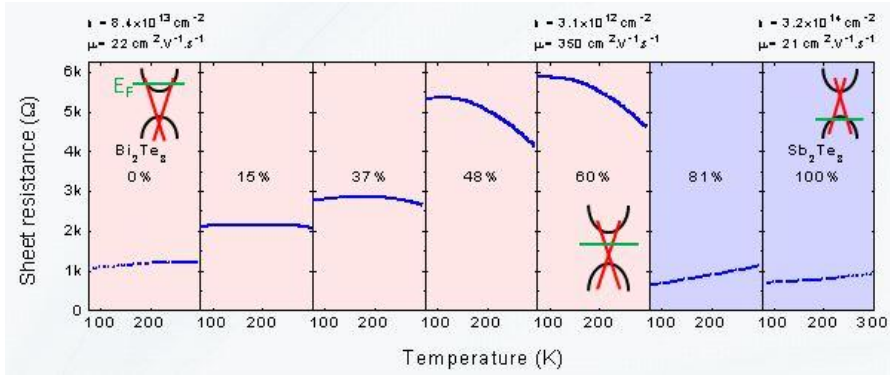


FIGURE 5.5: Characteristic sheet resistance vs temperature for variable Sb concentration.

observed in Seebeck coefficient as a function of Sb concentration.

The TIs and the  $\text{BaF}_2(111)$  substrates, are very sensitive to chemicals used on standard nanofabrication and handling protocols, which lead to significant damage of the structures. For example,  $\text{BaF}_2$  is sensitive to water and typically cannot be in contact with any aqueous solution, although this is used to our advantage. In addition, metal films easily peel from the  $\text{BaF}_2$  substrate, which is also extremely brittle, thus even a simple step such as wirebonding has to be revisited. Therefore the fabrication and handling protocols, which are described below and summarized in Figure 5.6, were developed exclusively for this thesis and have required significant optimization. The main steps are as follows:

1. Spin coating of MMA (EL 6) layer at 2500rpm for the 40s followed by baking for 1 minute at  $180^\circ\text{C}$ . Another layer of negative resist is also spin coated on top at 2000rpm for the 60s and baked for 2 minutes at  $85^\circ\text{C}$ .
2. Electron-beam lithography is then used to define the TI structure that will remain in the device. The structure is patterned using the negative resist, which will act as a mask for etching, thus the developer

only acts on it. The rest of the TI film is etched away using a two-step process. First, the exposed MMA after development is removed using O<sub>2</sub> plasma and then the TI using Ar-ion plasma.

3. In order to deal with the wirebonding issues, the contacts to the TIs, heaters and thermometers, were implemented in a two step process. First a lithography step is performed to expose only the large contact pads onto which the bonding is made. This process required the following steps. Spin coating of MMA at 2500rpm for the 40s; baking for 1 minute at 180°C. Two other layers of PMMA (A4) are added at 5000rpm for the 40s, subsequently baked during 1 minute and then 5 minutes at 180°C. A thin layer of AR PC 5090 is spin coated at 2000rpm for the 60s and baked at 85°C for 2 minutes. The BaF<sub>2</sub> is then place in deionized water for 3 minutes.
4. Spin coating of AR PC 5090 charge remover to carry out a second lithography step to pattern the small features of the devices and connections from the bonding pads to the TI structures. In this step water exposure is avoided. The devices are completed by the deposition of contact electrodes and bonding pads using an electron-beam evaporator: 4 nm of titanium and 50 nm of palladium finished by the lift-off.



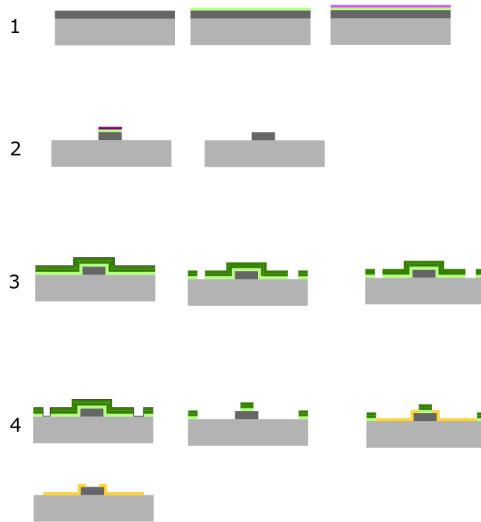


FIGURE 5.6: Schematic representation of the nanofabrication process.

The addition of a lithography step for bonding pads, followed by water, is implemented to improve the addition of the Ti/Pd films. This is necessary otherwise wirebonding proved to be a highly irreproducible process. The layer of AR PC 5090 is required to minimize charging build-up during electron beam lithography.

Figure 5.7 shows corresponding optical images of typical Hall bar (left) and thermopower characterization (right) devices. The Hall device comprises six contacts that allows us to characterize both the sheet resistance and the Hall response of the TIs. A current is applied horizontally using the far left and far right electrodes. For the sheet resistance measurements, the voltage is measured between either the top two or the bottom two remaining electrodes. For the Hall measurements, the voltage is measured between one top electrode and the bottom electrode right below.

The thermopower is measured across the small rectangular TI island at the center of the right image in Figure 5.7. The TI is contacted by two long horizontal Ti/Pd pads that also act as thermometers. The temperature is determined by the calibrated resistance of these pads with a four probe measurement technique. The large pattern at the bottom of the image running parallel to the thermometer pads, and perpendicular to the TI length, is the heater, which has four electrodes to further characterize its resistance as a function of temperature. The dimensions of the heater is selected to be much larger than any other structure (the TI and thermoemeters) so as to achieve a uniform temperature oriented in the vertical direction.

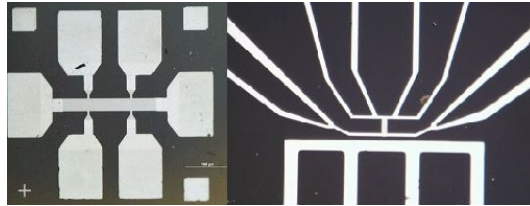


FIGURE 5.7: Optical microscope picture of a Hall bar device (left) and thermoelectric device (right). The width of the wire in the Hall bar and the length of the TI wire for thermoelectric measurements are  $10\ \mu\text{m}$  by  $3\ \mu\text{m}$ .

### 5.3 Thermopower and Seebeck coefficient estimation

In this section we describe the results obtained for the Seebeck coefficient in our topological insulator thin films. However, prior to measuring the thermopower, we have characterized the transport properties of the films. Figure 5.8 shows the resistance of the films as a function of temperature for selected Sb concentrations. The concentration of Sb was varied from 0% to 100%. These measurements shows that the transition from n to p doped films occurs at about 50% Sb. Indeed for 54,4% Sb, the response is clearly that of an insulator, with low doping and the Fermi level in the bandgap. The resistance increases sharply from room temperature down to 100 K. As previously reported at 100 K the resistance reaches a maximum and then at lower temperatures start to decrease, which is believed to be a hallmark of the dominant transport by the surface states.

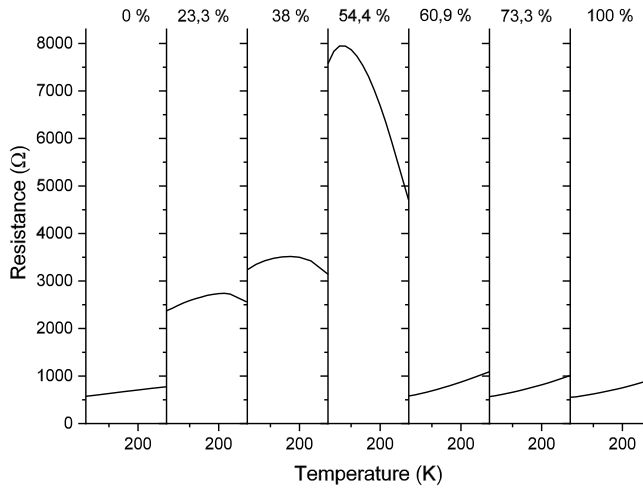


FIGURE 5.8: TI resistance vs temperature for selected Sb concentrations, going from no Sb (left) to 100% Sb (right).

The nature, density and mobility of the carriers can in principle be extracted from Hall measurements. Nevertheless, although the interpretation is straightforward when there is only one type of dopant, the existence of multiple dopants, and the coexistence of electrons and holes, make the interpretation significantly more complex. In any case, Hall experiments allows us to easily establish the nature of the *dominant* carriers and demonstrate the transition from electron to hole transport at about 50% antimony. In addition, as observed in Figure 5.9, the carrier concentration drastically drops from  $|n| \sim 4 \times 10^{14} \text{ cm}^{-2}$  for  $\text{Bi}_2\text{Te}_3$  and  $\text{Sb}_2\text{Te}_3$  down to  $|n| \sim 1 \times 10^{13} \text{ cm}^{-2}$  for  $(\text{Bi}_{1-x}\text{Sb}_x)_2\text{Te}_3$  with Sb concentrations of 38% and 60.9% ( $x = 0.38, 0.609$ ).

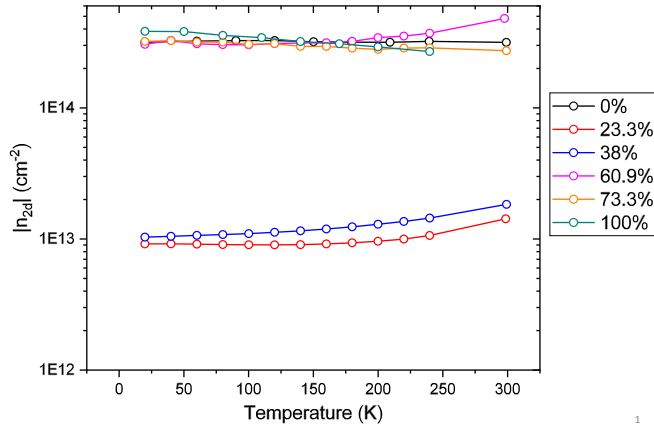


FIGURE 5.9: Carrier concentration in TI thin films with different Sb concentration, as estimated from Hall measurements assuming one type of carriers

The mobility also is seen to change, Figure 5.10 indicates that as the decrease in the carrier concentration is accompanied by an increase in the mobility, in accordance with the increasing relevance of the surface states in the transport and the suppressed back scattering.

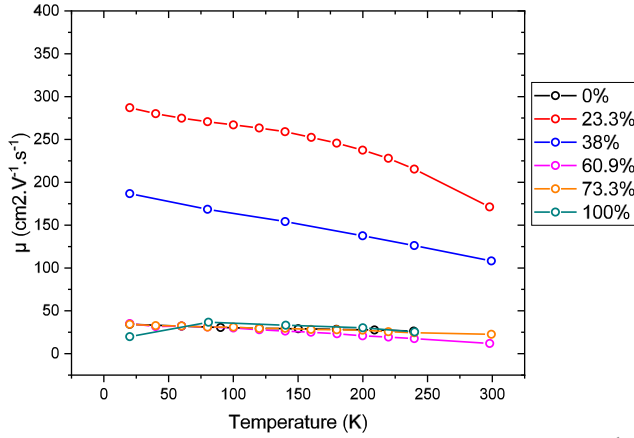


FIGURE 5.10: Carrier mobility in TI thin films with different Sb concentration, as estimated from Hall measurements assuming one type of carriers

The carrier densities of the binary alloys are too large for them to be just located at the surfaces. However, it is possible that for Sb concentrations of 38% and 60.9%, the Fermi level is in the gap above and below the Dirac point to the surface states, respectively. The carrier density and mobility for 54.4%Sb are not shown Figures 5.9 and 5.10. The reason for this is the difficulty to estimate their values stemming from the non-trivial coexistence of electron and hole carriers in this material. The character of the dominant carrier, however, can be obtained, yielding interesting results.

Figure A.3 (left panel) shows the Hall resistance,  $R_{xy}$ , versus out-of-plane magnetic field  $B$  at different temperatures from room temperature (300 K) down to 140 K. While at room temperature the dominant carriers are hole-type, their character switches to electron type at 210 K and below. This is reflected in the change of slope in  $R_{xy}$  versus  $B$  from negative to positive, which occurs at about 220 K (see right panel). At low temperatures, the transport is clearly dominated by n-type carriers, which would indicate that the Fermi level is slightly above the Dirac point of the topological surface bands. Assuming one type of carriers, the carrier concentration

at 50 K per surface is found to be as low as  $|n| \sim 1 \times 10^{12} \text{ cm}^{-2}$ , with a mobility that is larger than any of the other films ( $\mu > 350 \text{ cm}^2/\text{Vs}$ ) at all temperatures.[68]

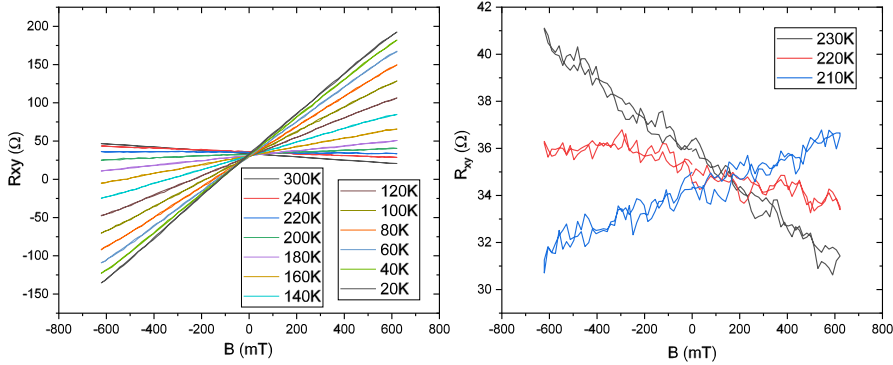


FIGURE 5.11: Hall resistance  $R^{y/x}$  for 54.4%Sb at different temperature

Having characterized the nature of the carriers as a function of Sb concentration, we now concentrate on the behavior of the thermopower. The experimental set-up is described in Chapter 2, together with the fundamental concepts of the data acquisition. Figure 5.12 summarizes the main results. There, the Seebeck coefficient is shown for different Sb concentration as a function of temperature. The sign of the coefficient directly correlates with the type of carriers, when one of the carries is clearly dominant, changing from negative to positive when from n-type to p-type carriers.

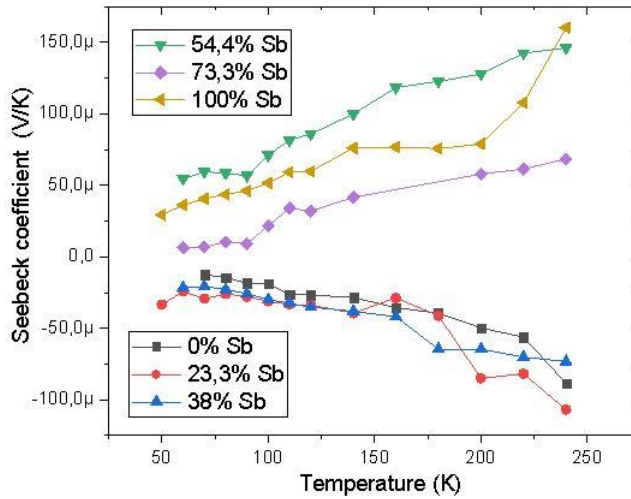


FIGURE 5.12: Seebeck coefficient at different temperature for various concentration

Remarkably the largest Seebeck coefficient is observed in the optimally-doped TI with 54.4% Sb. However, the sign does not follow the trend observed with the other films. Indeed, even though the Hall measurements in Figure A.3 suggest n-type transport, below 210 K, the Seebeck coefficient remains positive all the way down to the lowest temperatures measured (60 K). This is not unusual, as electronic and thermal transport are governed by different physical phenomena. For example, while electronic transport is characterized by the conductivity, the thermoelectric coefficient instead follows the derivative of the conductivity in energy, as per the well-known Mott relation. In addition, the Seebeck coefficient seems to reach a plateau below 100 K, when the electronic transport is dominated by the n-doped surface states. However, the current sensitivity of our measurements does not allow us to make any claims.

Overall, the general trend is that the Seebeck coefficient increases (in magnitude) both for electrons and holes when approaching the charge neutrality point. Such a behaviour agrees very well with that expected in a Dirac material. Furthermore, the results observed with our MBE grown

films are in close agreement with those reported in nanowires of the same materials, which were interpreted as being dominated by surface states [37].

The nanowires, with a thickness of from 30 to 190 nm and different Sb concentration, were synthesised with a vapor-liquid-solid (VLS) method. The agreement includes the magnitude of the Seebeck coefficients as a function of Sb concentration, as well as the change in sign at about 50% Sb, and the tendency to increase nearby the charge neutrality point. The only significant discrepancy between our results with those of Ref. [37] is that the nanowires in Ref. [37] do not *present any signature* of surface-dominated transport in the conductivity measurement; their conductivity is observed to always increase monotonically all the way down to 50 K.

The observations in the previous paragraph seems to suggest that surface states might not play a dominant role in the magnitude of the Seebeck coefficient. In other words, surface transport does not dominate the conductivity in the nanowires of Ref. [37]. Even though in our films, which are significant thinner (9 nm), this has been achieved, the change is not reflected in the Seebeck coefficient, which follow the same trend in both studies. The lack of correlation between surface transport and the Seebeck coefficient is further supported by the lack of correlation between the carriers that dominate the two phenomena. In our devices, the surface carriers appear to be electrons, but the thermopower is generated by holes.

## 5.4 Summary

The growth of  $(\text{Bi}_{1-x}\text{Sb}_x)_2\text{Te}_3$  with different concentration of antimony was made. The films were processed into thermoelectric and Hall bars devices. The Seebeck coefficient was measured as well as the Hall the nature of the carriers, using Hall measurements. The thermoelectric study of TIs with the position of the Fermi level indicates a lack of correlation between Seebeck coefficient and surface electric transport. Overall this indicates that the implications of the surface states on the Seebeck coefficient are not straightforward. These observations lead us to conclude that scaling down the thickness to improve the thermoelectric response does not necessarily



represents a good approach. First, surface and bulk thermoelectric properties might be optimum at different Fermi levels. Second, the Seebeck coefficient for surface transport is expected to be negative for our optimal TI but, in contrast, the actual Seebeck coefficient is positive. Surface states might be therefore suppressing the total thermopower that is dominated by the bulk. Our results are almost identical to those obtained with much thicker nanowires, which are a factor 3 to 20 thicker than our films. This further indicates that surface states are perhaps not playing a dominant role. It might be necessary to carry out experiments with just a few quintuple layers, that is, films of 5 *nm* or less in order to reveal the signatures of surface states in the Seebeck coefficient. Another approach is the fabrication of super-lattices as those in Ref. [95], where a record large thermoelectric figure of merit *ZT* of 2.4 was reported but never reproduced. Future studies on the current topic are therefore recommended.

## Chapter 6

# Conclusion and perspective

With the rapid development of electronic and optoelectronic devices, thermal management has become a field of critical importance over the last two decades. The heat generated by a microprocessor accounts for more than 50% of its power usage and thus only half of it is employed in useful logical operations. In a broad sense, thermal management involves two aspects, the first is the dissipation created by the electronics, the second is the use of the heat that currently is just wasted. This thesis deals with topics that are related to these two main challenges from a material and material characterization perspective. Two-dimensional (2D) materials have exceptional electrical, optical, mechanical, thermal and thermoelectric properties, they also offer numerous opportunities for future electronic, optoelectronic and other devices. However, their integration into electronics will face major challenges. Most notably, they include scaling to mass produce them, but also developing methods to characterize their properties both when isolated and as a part of heterostructures. Because of the limitation to obtain high quality single crystals beyond a few tens of micrometres, and because they have very high thermal conductivities the use of established properties to measure their thermal conductivity might not be straightforward. In addition, 2D thermoelectric materials based on bismuth and antimony chalcogenides have been discovered to be also topological insulators (TI), with intriguing topological surface states. However, it is still unknown if the surface states influence the thermoelectric properties of these materials, specially when the thickness is scaled down and the surface states dominate the electric transport. Furthermore, 2D materials give us an opportunity to study some interesting thermal phenomena that are novel or are hard to observe in bulk materials.

In this work, we focused on a recently developed technique at ICN2 to measure the thermal properties of suspended membranes. Such a method, dubbed two-laser Raman thermometry, uses a laser to heat the central part of the membrane. Then a second is scanned over the membrane to measure the local temperature (using Raman spectroscopy). It was first used in large (100  $\mu\text{m}$ ) suspended membranes of Si, and on small (10's of  $\mu\text{m}$ ) membranes of poly crystalline MoS<sub>2</sub>, which has very low thermal conductivity. However, it was not obvious that this technique could be translated to small membranes of 2D single crystals that are expected to have some of the largest known thermal conductivities, as thermal gradients could turn out to be too small to measure. Therefore, on this thesis efforts were directed to i) fabrication techniques and sample design protocols and ii) investigate the thermal conductivity using tw-laser Raman thermometry in different 2D materials and compare with available literature (which is rather scarce). After establishing suitable sample fabrication protocols, we first measured the thermal conductivity of CVD graphene, which was found to be  $k = 305 \text{ W}/(\text{m}\cdot\text{K})$ . This value is one order of magnitude smaller than the reported exfoliated graphene which can be explained by the grain boundaries and disorder. The polymer residues from the transfer technique can also have an effect on the heat transport. Large membranes of CVD graphene have been processed with always some remaining polymer residues on top. Some new techniques allow us to reduce the impact of the polymer by using anthracene (or PMMA) as a sacrificial layer. The process enables the dry removal of the sacrificial layer at temperatures below 150 °C in combination with annealing in air and in the presence of Pt catalyst achieve a cleaner CVD graphene [107]. Future investigation should focus on the degree of disorder (density of grains and defects), they can even be focused on the influence of high temperature resistive polymers, which could affect the phonon heat transport in an anisotropic fashion; for example chemical modification of graphene can be obtained by photopolymerization with styrene [92].

We were also able to measure the thermal conductivity of MoS<sub>2</sub> membranes, of variable thicknesses. Using two-laser Raman we observed and increased thermal conductivity as a function of thickness,  $k$  at room temperature from 12 W/m.K for a 7-layer membrane to 24 W/m.K for a 20-layer one (suspended on a 20  $\mu\text{m}$  hole). However, more samples are needed

to establish this trend. In addition, an even thinner membrane of a 4-layer MoS<sub>2</sub> (10 μm hole) was characterized with one-laser Raman thermometry obtaining  $k = 23,6 \mu\text{m}$ , similar to the 20-layer membrane. However, this may indicate that in this case the  $k$  is overestimated due to additional heat transport to the substrate in the small hole, which is difficult to quantify. With the same technique (and hole size) a flake of MoSe<sub>2</sub> was measured with thermal conductivity of 63 W/m.K. Note that it was not possible to use two-laser Raman thermometry on these latter two samples because, being the membrane too small, the thermal gradients were suppressed and the spatial resolution limited. However, the demonstration of both techniques on similar suspended membranes opens the door for investigating and establishing the advantages and disadvantages of using two or one-laser Raman thermometry in membranes larger than 20 μm. Although, an interesting and rather straightforward goal to aim at, it was not possible to achieve it thoroughly in this thesis due to the sample degradation.

Finally, one MoS<sub>2</sub> sample was stacked, after being characterized, with a hBN flake after measurement to create a MoS<sub>2</sub> /hBN van der Waals heterostructure. This type of heterostructure is attracting increasing attention because of new properties that cannot be achieved with the materials individually and the potential applications deriving from them. In this case MoS<sub>2</sub> is a candidate for digital electronics (transistors) while hBN is a dielectric that could also help dissipate heat. Indeed, we demonstrate that the addition of the hBN flake increases the thermal conductivity from 24 W/m.K MoS<sub>2</sub> to 185 W/m.K hBN/MoS<sub>2</sub>, which shows the potential impact of layer assembly can have for heat managing. Heat generated (or in our case deposited by the laser) in MoS<sub>2</sub> can be taken away from the hot spot by hBN. This result is in agreement with recent studies addressing the thermal conductivity of hBN and its interface with MoS<sub>2</sub>. Indeed, the thermal conductivity in a similar 11-layer hBN membrane was reported to be of 360 W/m.K [46], whereas the interface thermal conductance of MoS<sub>2</sub> /hBN was found to be  $17 \text{ MW}^{-2}\text{K}^{-1}$ , which is lower than the graphene hBN interface  $52 \text{ MW}^{-2}\text{K}^{-1}$  [60]. Such a result illustrates a strong transfer of heat from hBN/MoS<sub>2</sub>. Further, systematic studies must therefore focus on the interfacial coupling, the phonon modes involved in the heat transfer, and in finding ways to optimize it. A key parameter to vary is the respective thickness of all the layers in the heterostructure to separate

the bulk from the interfacial effects. Further in the future, effects like heat rectification can be investigated, as described for Si with phonon mean free paths comparable to a specific hole arrays [86]. For 2D materials, this can perhaps be achieved with holes or even changes in the layer thickness.

In addition to thermal properties, we investigated energy harvesting by means of thermoelectricity. Here the goal was to evaluate whether the thermoelectric properties of BTS materials were affected by their intrinsic topological surface states. BST thin films have been grown by molecular beam epitaxy and had a nominal thickness of 10 nm, thin enough to observe electronic transport dominated by surface states. The films were grown with controlled thickness of Bi and Sb in order to vary the Fermi level. We first demonstrated with our films, using electrical conductivity, Hall measurements and ARPES that the carrier nature continuously changes from electron to hole when the concentrations of Sb goes from 0 to 100%. This is in agreement with literature results. We also found that at about 50% aSb the Fermi level is in the gap, in the fabricated devices, and that the conductivity is dominated by surface states, also in agreement with literature. We then investigated the thermoelectric properties of the *same* films. Surprisingly, we have found no correlation between the dominant carriers for electronic transport and the thermoelectric properties. For example, while electronic transport in the surface states presents electron character, the thermoelectricity presents hole character. Moreover, the transition between surface to bulk transport occurs at a threshold temperature of about 100 K. This results in a peak on the resistivity at that temperature (at lower temperatures the carrier mobility in the surface is enhanced). The distinct character of the carriers in the surface and bulk suggests that not only surface states do not enhance the thermopower, but they might even suppress it by opposing the bulk contribution. Further studies must address the optimization of the contributions of the bulk and surface states, as they might be optimal at different temperatures or Sb concentrations. Our results leave little hope for enhance thermoelectric properties of bare films using surface states; perhaps multilayers might offer a promising route, but this has been not studied yet, specially taking into consideration the topological states. To separate the surface state contribution from that of the bulk, we recommend using thinner films.

Lastly, the characterization of BST thin films using Raman thermometry revealed Raman shifts that correlated with the concentration of Sb. The increase in laser power revealed the appearance of the non-active Raman peaks, which can indicate the presence of broken structural symmetries, surface phonon modes or other effects such as plasmonic resonances. The interesting response is worth for further investigation, using complementary techniques such as ellipsometry. even though the results are worth mentioning in this thesis, they have not been central to it.



## Appendix A

# Thermal conductivity modélisation

Some specifics of the simulation procedure for fitting the two-laser Raman thermometry experiments: The simulations have been made using a finite element method commercial software (COMSOL). We have assumed an effective medium model that simulate the temperature spatial profile over the circular membranes volume aiming to mimic the two-laser Raman thermometry experiment. As input parameters we use the absorbed power (distributed in a Gaussian profile, which can be shifted from the centre of the membrane by an amount parametrized as  $x_0$ ), the effective thickness and radius of the membrane (the temperature of the edges of the membrane, i.e., where the MoS<sub>2</sub> contacts the substrate, is kept to be 300K), a temperature-independent thermal conductivity ( $k_0$ ) and the relative spatial shift between the centre of the heating laser and the probe laser ( $y_{\text{shift}}$ ). The latter means that, when doing the line profile, the probe laser does not exactly pass over the heating laser, the minimum distance between them being  $y_{\text{shift}}$ . In particular we have simulated spatial profiles for a wide range of values for  $x_0$ ,  $k_0$  and  $y_{\text{shift}}$  (having the other parameters fixed to the values measured experimentally) with the objective of minimizing the difference between the experimental and simulated temperature curves. The figures reported afterwards reflect the results of this study, putting a special focus on the results obtained for the set of parameters that generate a simulated temperature profile that fits better to the experimental results. The COMSOL model was made by Dr. Daniel Navarro Urriós.



Absorbed Power= 39.8  $\mu\text{W}$

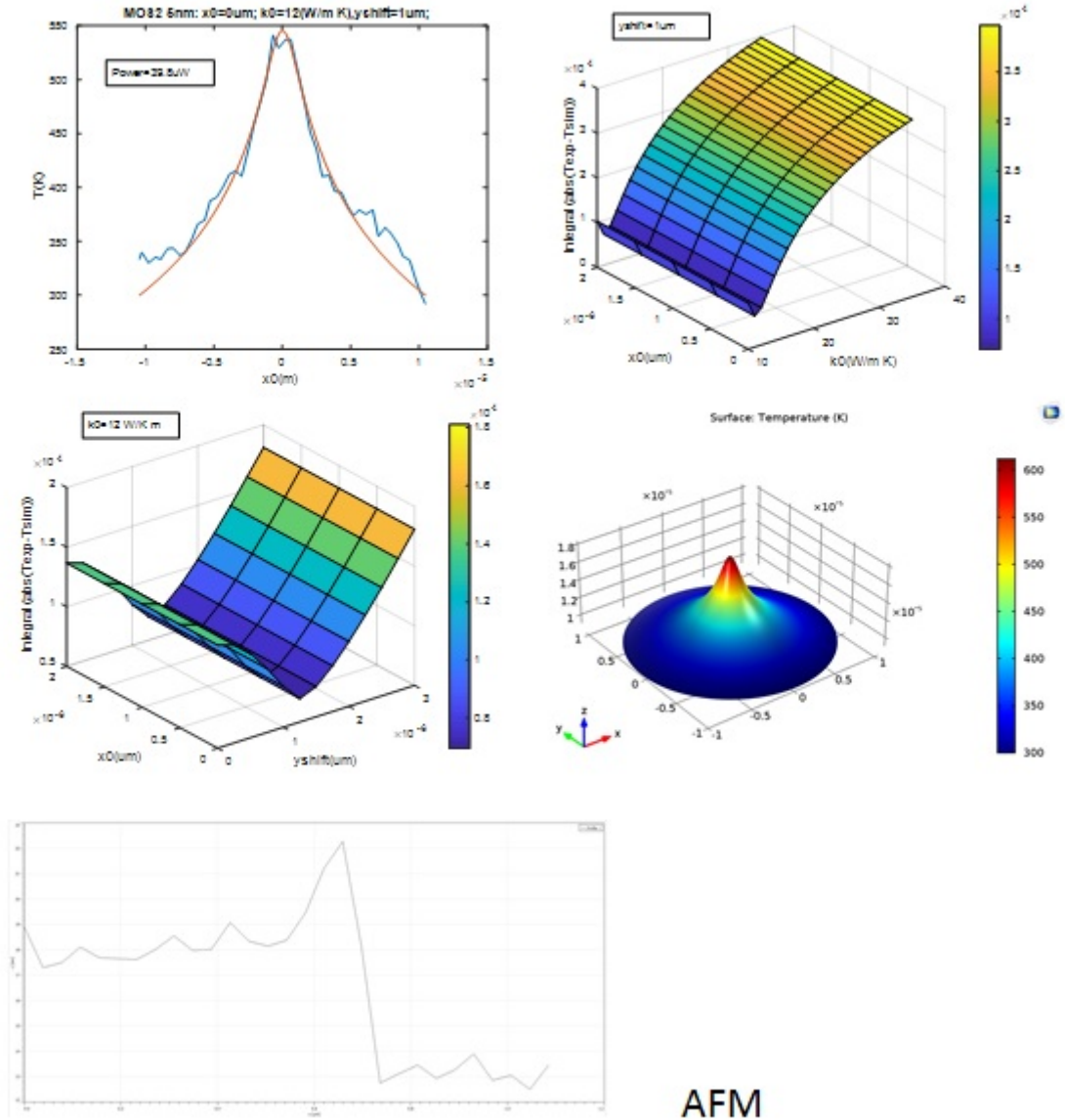


FIGURE A.1: Seebeck coefficient at different temperature for various concentration

Absorbed Power= 425.38  $\mu$ W

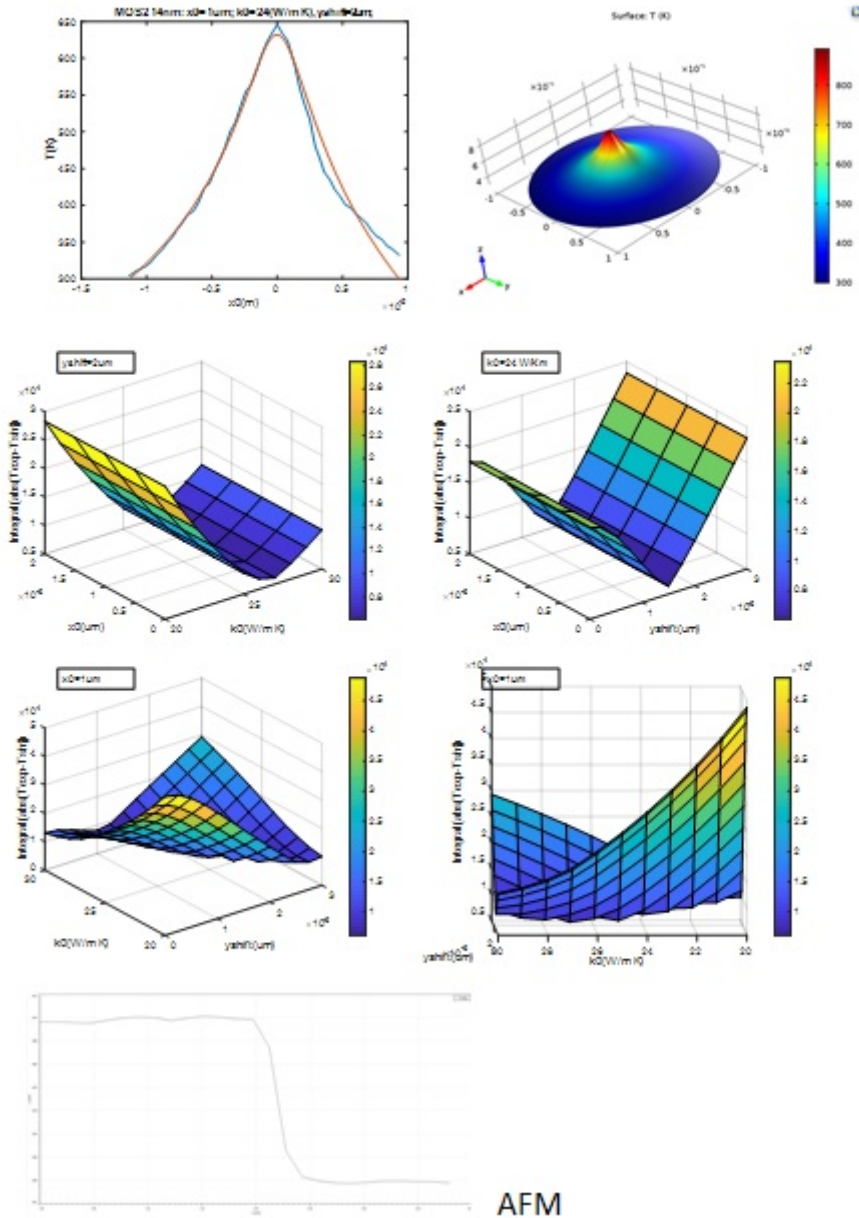


FIGURE A.2: Seebeck coefficient at different temperature for various concentration

Absorbed Power= 7078.21  $\mu\text{W}$

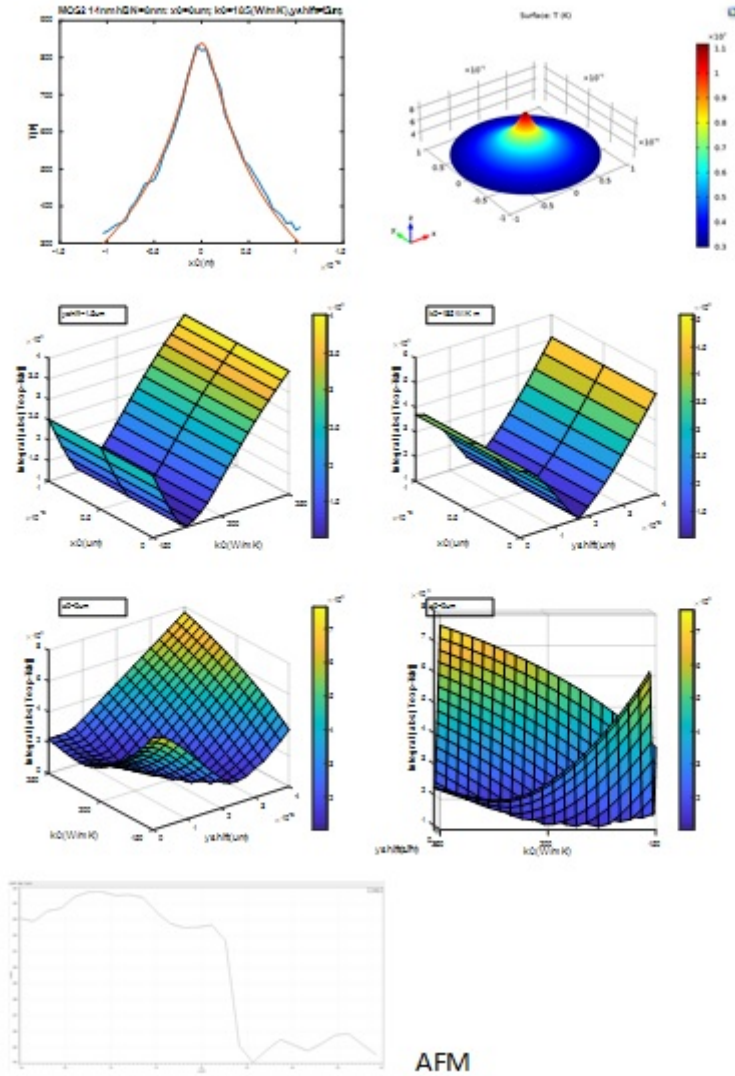


FIGURE A.3: Seebeck coefficient at different temperature for various concentration

## Appendix B

# Raman parameters and BST concentration

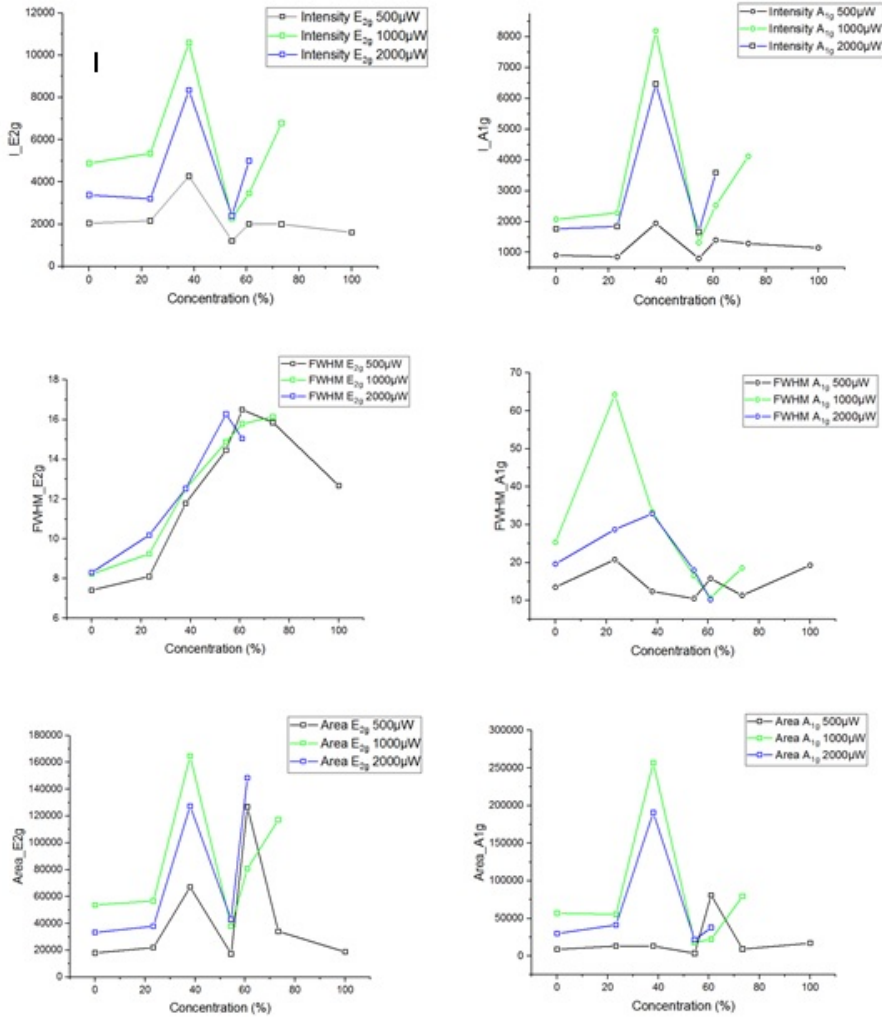


FIGURE B.1: Intensity, Full width at half maximum and Area of Raman peak spectra for different concentration.

## Appendix C

# Exfoliation and transfer technique

### Graphene exfoliation

1. The first thing to do is to start exfoliating with the "blue tape" by placing the bulk graphite on it. After applying some pressure the bulk materials is removed.
2. The residues of the bulk materials are then repeatedly exfoliated between tapes. After some times, the materials on the tape look thin (brighter color).
3. This step is made to clean the Si/SiO<sub>2</sub> substrate with oxygen plasma at 400 and 50 rpm during 5 minutes.
4. Put into contact the substrate and the tape that possesses some graphene flake on top.

### hBN exfoliation

The work of Gorbachev et al. [34] shows that the Raman shift can be caused by the strain applied to the hBN layer. Below two methods of exfoliation are described depending on the desired thickness.

Thicker and large layer: This technique will help to have large layers more than  $100 \mu^2$  with thickness around 10 nm. For that, we need to use viscoelastic silicone polymer also known as Polydimethylsiloxane (PDMS).

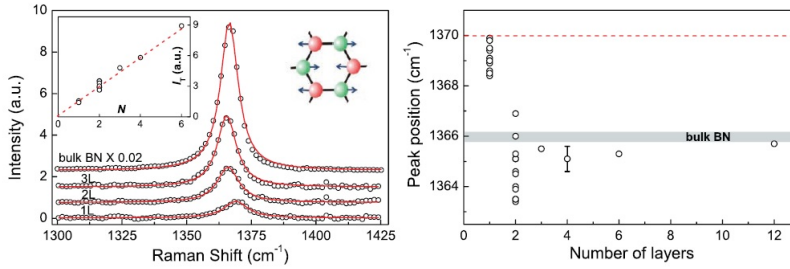


FIGURE C.1: a) Raman spectra as a function of the number of hBN layers. Insert, peak intensity vs the number of layers. b) Raman shift position function of the number of layers.

1. First take cut several pieces of PDMS from ®Gel-pak - WF - with a retention level of X4.
2. This PDMS is encapsulated with two covers, one being thinner than the other one.
3. Place a hBN crystal on top of the PDMS press on with another one.
4. Remove the crystal and repeat the exfoliation between the PDMS polymer. New PDMS can be added to the exfoliation in order to get uniform and large flakes.

Thin and small layer: This method is quite similar to the exfoliation of graphene because it is using a substrate of  $\text{SiO}_2/\text{Si}$ . This time, the oxide layer is of 90 nm. This allows a better identification of thin layers.

1. It's possible to exfoliate thin layers with PDMS or blue tape. The idea is to repeat the exfoliation and end up by pressuring the exfoliated crystal on top of a 90 nm  $\text{SiO}_2/\text{Si}$  substrate.
2. hBN crystal is placed on top of a blue tape and the other side of the tape is placed on top. The goal is to exfoliate by creating lines of hBN.
3. For the exfoliation with PDMS we use DGL films X4 from ®Gel-pak. Cut a small piece and place it on a glass slide. Exfoliate two PDMS several times that have some hBN flakes.

4. Pressure the tape or the PDMS on top of the substrate.
5. Final step is the inspection of the hBN flakes under the microscope.

**TMDCs exfoliation:**

Similar to hBN exfoliation methods described above we use for the TMDCs exfoliation. This thesis only focuses on MoS<sub>2</sub> and MoSe<sub>2</sub>.

TMDC exfoliation with PDMS:

- The first step is to exfoliate for the bulk source with a tape. Place the tape onto the crystal and remove it leaving some crystal.
- Put the tape on the table and stick to it.
- Take some SVP244 (yellow tape) tape to exfoliate again.
- Put the PDMS WF X4 from ®Gel-pak on the tape that has exfoliated materials.
- Remove it slowly and check under the microscope with the transmission mode.

MoS<sub>2</sub> exfoliation with gold: This technique can be used to have large monolayer of TMDC that contain Sulfur atoms. The Sulfur atoms are going to have a strong interaction with the gold which will allow control exfoliation [22].

1. Exfoliation some MoS<sub>2</sub> on blue tape.
2. Evaporate gold on top of MoS<sub>2</sub>/tape.
3. Place Thermal releasing tape (TRT) on top of the gold.
4. Put the MoS<sub>2</sub>/gold/TRT on top of the desired substrate.
5. Remove the TRT.
6. Use gold etchant to remove the gold.

Residues of gold can remain in this type of exfoliation. The picture below shows it is possible to get monolayer MoS<sub>2</sub>.



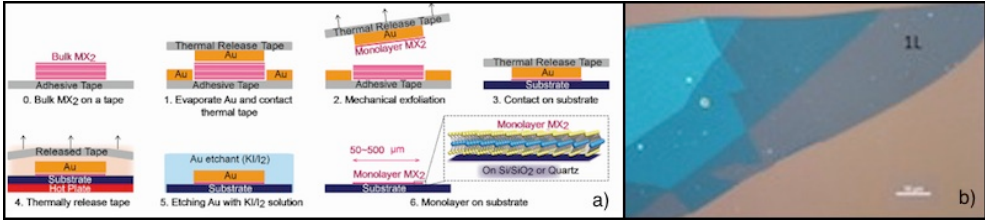


FIGURE C.2: a) MoS<sub>2</sub> gold exfoliation step [desai2016gold]. b) Example of a monolayer MoS<sub>2</sub> exfoliated with gold resting on a 90 nm SiO<sub>2</sub>/Si

### TIs film exfoliation:

It is also possible to exfoliate film topological insulators grown by the MBE.[47] Since the TIs are sensitive to oxidation thus great care needs to be taken. Such surface oxidation is the origin of the degradation of topological surface states.

1. Spin coat PMMA at 5000 rpm during the 40s, at least 5 times to make it thick on top the TI/BaF<sub>2</sub>.
2. Stick the substrate and use TRT tape to take off some of the materials.
3. Release the materials by putting in on as substrate at temperature around 90 C during 15 minutes.

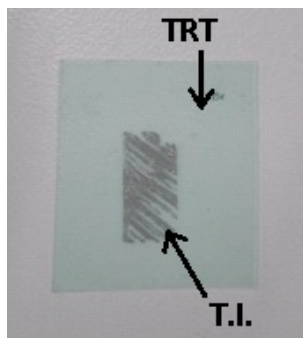


FIGURE C.3: Picture of exfoliated Topological Insulator material from BaF<sub>2</sub> with PMMA and TRT [47].

### C.0.1 Transfer of 2d materials on the membranes

All dry viscoelastic transfer: This is the most common technique after exfoliating on top the PDMS transfer the identified flake where it is needed. One issue with this technique is that the polymer is transparent and it is impossible to see thin layers of hBN on top, due to its large band gap (6 eV). Graphene can be glanced with the highest objective (x100) but it is then almost impossible to transfer it at a wanted position. The TMDCs are the perfect candidate for this technique, they have indirect to direct band gap small enough to be looked at with the transmission mode of the microscope.

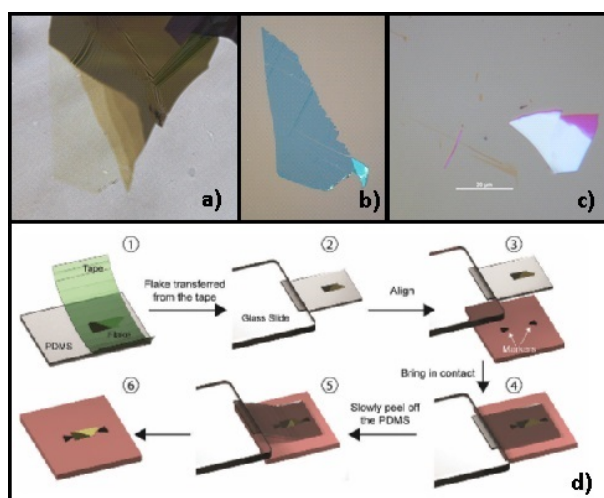


FIGURE C.4: Picture of an MoS<sub>2</sub> flake a) on top of PDMS film b) on 90 nm SiO<sub>2</sub>/Si. c) Picture of an graphene flake with an flake of MoS<sub>2</sub> on top. d) Schematic representation of the transfer technique with a WF PDMS film [28].

The figure ?? shows the identification of monolayer MoS<sub>2</sub> exfoliated on PDMS, and transferred on 90 nm SiO<sub>2</sub>/Si.

Capillary-force assisted Transfer: This transfer technique is using the capillarity force created by evaporating some water on top of the PDMS. The figure C.5 a) is the schematic representation of this method. And in the figure C.5 b) it is shown a twisted triangle of MoS<sub>2</sub> grown on Sapphire by the company 2Dlayer. The problem with this technique is that the flakes may break during the transfer. A more secure way to transfer is then to use a polymer on top of the PDMS.

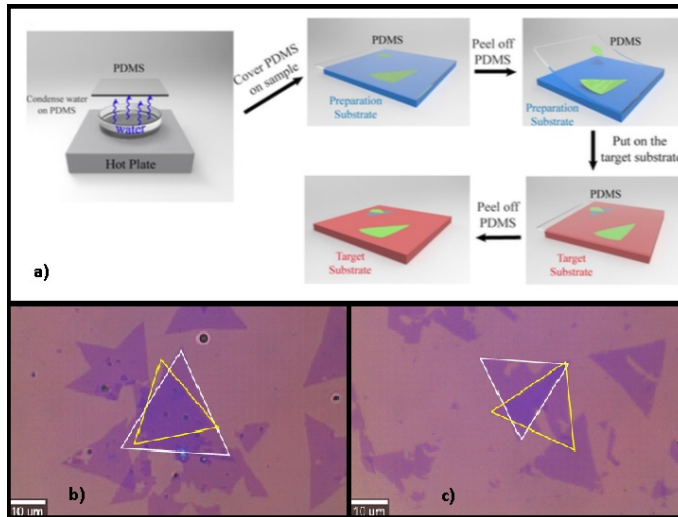


FIGURE C.5: Schematic representation a) of the capillarity transfer [62]. Optical picture of twisted CVD MoS<sub>2</sub> triangle flakes picked up from sapphire and transfer twice onto 90 nm SiO<sub>2</sub>/Si

### PPC or PMMA Transfer:

By adding an extra layered polymer, this technique allows to create clean 2d heterostructure materials. Typically, some 2d flakes are hard to take from the substrate due to a strong adhesion to it. Fortunately, it is possible

to handle the in-between flakes without touching any polymer. This process can be referred as the van der Waals pick-up/transfer with the support of typically a hBN flake, the interaction of van der Waals between different 2d materials are lifting the flakes that is on the substrate. This enable to create clean 2d materials heterostructure [76].

There are two highly efficient polymer that can be used on top of the PDMS, Polypropylene carbonate (PPC) and Poly(methyl methacrylate) (PMMA). The difference between the two polymer is their melting point property. PPC is employed to pick up graphene from  $\text{SiO}_2/\text{Si}$  and PMMA can help to manage to pick up monocrystal of CVD graphene from copper [5].

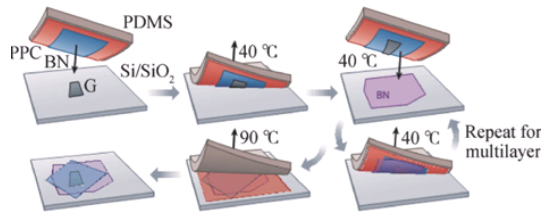


FIGURE C.6: Transfer method using PMMA/PDMS or PPC/PDMS stamp [54]

The figure C.6 is representative of the different steps of the van der Waals transfer technique. A flake of hBN needs to pick up from  $\text{SiO}_2/\text{Si}$  to PPC/ PDMS stamp. Then hBN/PPC/PDMS is brought in contact with the intended flake and is removed slowly with the new flake attached to it. The stack can be then aligned on a new substrate and put in contact to then being released. It is also possible to take only some part of flake, then rotate it with a desired angle [50]. This kind of transfer helps to make heterostructure where the angle between the layers is taking into aspect and can have an important impact of physics properties of the structure. Twisted angle of graphene superlattices has an effect on superconductivity [15].

### PLLA Transfer:

This transfer method was commonly used for structures with different dimensions on various surface properties [56]. It can be easily transferred on hydrophobic, hydrophilic and flexible substrate.

The first step of this transfer method is to spin coat the PLLA polymer previously made *concentration* at 2000rpm for 20s. The polymer is going to be spread all around the sample and only has to be pick-up. Therefore, a cut in all around the polymer edges is needed to lift the full stack. A PDMS polymer is placed on top of the PLLA and a drop of water is used to detach the PLLA/PMMA stamp from substrate. It is then possible to release the PLLA from the PMMA by heating the substrate/PLLA/PMMA to 90° C and gently remove the PDMS.

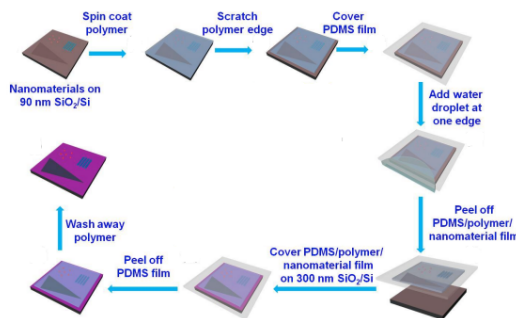


FIGURE C.7: Transfer method using PLLA/PDMS stamp [56]

### CVD graphene:

In this case, the CVD graphene is first grown on copper and then transferred with fishing technique on a substrate. This process is considered has a wet chemical transfer and it uses PMMA as a temporary support during the etching of the copper by etchants like iron chloride (FeCl<sub>3</sub>), hydrochloric acid (HCl) or ammonium persulfate (NH<sub>4</sub>)<sub>2</sub>S<sub>2</sub>O<sub>8</sub> [57] [49]. This transfer is using the following step :

1. Spin coating of PMMA on the chosen graphene side. The copper is placed on a PDMS WF x4 to effectuate the spin coating.

2. The back side of the unwanted CVD graphene is etch either by  $O_2$  or chemically.
3. Then etching of the Cu foil followed by several cleaning steps under deionized water.
4. The PMMA/graphene stack is "fished out" off the water and transferred on a substrate.
5. Removal of PMMA by putting it in acetone and cleaning with isopropanol.

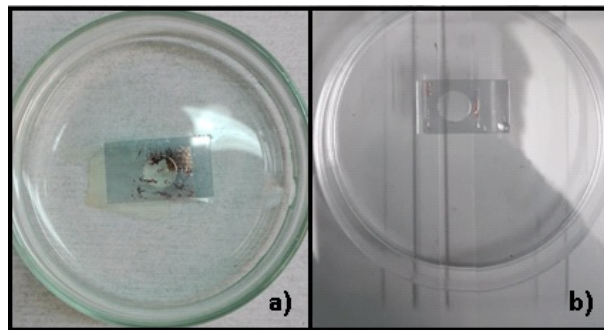


FIGURE C.8: Picture a) is a stamp of CVD graphene/PMMA/PDMS with hole in the etching solution. b) Drying of the CVD graphene/PMMA membrane



# Bibliography

- [1] Adili Aiyiti et al. "Thermal conductivity of suspended few-layer MoS<sub>2</sub>". In: *Nanoscale* 10.6 (2018), pp. 2727–2734.
- [2] Can Ataca, Hasan Sahin, and Salim Ciraci. "Stable, single-layer MX<sub>2</sub> transition-metal oxides and dichalcogenides in a honeycomb-like structure". In: *The Journal of Physical Chemistry C* 116.16 (2012), pp. 8983–8999.
- [3] Jung Jun Bae et al. "Thickness-dependent in-plane thermal conductivity of suspended MoS<sub>2</sub> grown by chemical vapor deposition". In: *Nanoscale* 9.7 (2017), pp. 2541–2547.
- [4] Alexander A Balandin et al. "Superior thermal conductivity of single-layer graphene". In: *Nano letters* 8.3 (2008), pp. 902–907.
- [5] Luca Banszerus et al. "Ultrahigh-mobility graphene devices from chemical vapor deposition on reusable copper". In: *Science advances* 1.6 (2015), e1500222.
- [6] Sophie L Benjamin et al. "Compositionally tunable ternary Bi<sub>2</sub>(Se<sub>1-x</sub>Te<sub>x</sub>)<sub>3</sub> and (Bi<sub>1-y</sub>Sb<sub>y</sub>)<sub>2</sub>Te<sub>3</sub> thin films via low pressure chemical vapour deposition". In: *Journal of Materials Chemistry C* 6.29 (2018), pp. 7734–7739.
- [7] Achintya Bera et al. "Sharp Raman anomalies and broken adiabaticity at a pressure induced transition from band to topological insulator in Sb<sub>2</sub>Se<sub>3</sub>". In: *Physical review letters* 110.10 (2013), p. 107401.
- [8] A. Berkdemir et al. "Identification of individual and few layers of WS<sub>2</sub> using Raman Spectroscopy". In: *Sci Rep* 3 (2013), p. 1755.
- [9] Ibrahim Boulares et al. "Surface phonons in the topological insulators Bi<sub>2</sub>Se<sub>3</sub> and Bi<sub>2</sub>Te<sub>3</sub>". In: *Solid State Communications* 271 (2018), pp. 1–5.



- [10] Qiran Cai et al. "High thermal conductivity of high-quality monolayer boron nitride and its thermal expansion". In: *Science advances* 5.6 (2019), eaav0129.
- [11] Weiwei Cai et al. "Thermal Transport in Suspended and Supported Monolayer Graphene Grown by Chemical Vapor Deposition". In: *Nano Letters* 10 (2010), p. 1645. DOI: [10.1021/nl19041966](https://doi.org/10.1021/nl19041966).
- [12] J. Camassel, L. A. Falkovsky, and N. Planes. "Strain effect in silicon-on-insulator materials: Investigation with optical phonons". In: *Phys. Rev. B* 63 (2000), p. 035309. DOI: [10.1103/PhysRevB.63.035309](https://doi.org/10.1103/PhysRevB.63.035309). URL: <https://link.aps.org/doi/10.1103/PhysRevB.63.035309>.
- [13] I. H Campbell and P. M Fauchet. "The effects of microcrystal size and shape on the one phonon Raman spectra of crystalline semiconductors". In: *Solid State Commun.* 58 (), p. 739.
- [14] D Campi, M Bernasconi, and G Benedek. "Ab-initio calculation of surface phonons at the Sb<sub>2</sub>Te<sub>3</sub> (111) surface". In: *Surface Science* 678 (2018), pp. 46–51.
- [15] Yuan Cao et al. "Unconventional superconductivity in magic-angle graphene superlattices". In: *Nature* 556.7699 (2018), p. 43.
- [16] Andres Castellanos-Gomez et al. "Deterministic transfer of two-dimensional materials by all-dry viscoelastic stamping". In: *2D Materials* 1.1 (2014), p. 011002.
- [17] Biswanath Chakraborty et al. "Layer-dependent resonant Raman scattering of a few layer MoS<sub>2</sub>". In: *Journal of Raman Spectroscopy* 44.1 (2013), p. 92. DOI: [10.1002/jrs.4147](https://doi.org/10.1002/jrs.4147).
- [18] Catalin Chiritescu et al. "Ultralow thermal conductivity in disordered, layered WSe<sub>2</sub> crystals". In: *Science* 315.5810 (2007), pp. 351–353.
- [19] Emigdio Chávez et al. "Structural analysis of nanocrystalline BaTiO<sub>3</sub>". In: *Journal of Molecular Structure* 984 (2010), p. 131. URL: <http://www.sciencedirect.com/science/article/pii/S0022286010007520>.
- [20] Melvin Cutler and N. F. Mott. "Observation of Anderson Localization in an Electron Gas". In: *Phys. Rev.* 181 (3 1969), pp. 1336–1340. DOI: [10.1103/PhysRev.181.1336](https://doi.org/10.1103/PhysRev.181.1336). URL: <https://link.aps.org/doi/10.1103/PhysRev.181.1336>.

- [21] Cory R Dean et al. "Boron nitride substrates for high-quality graphene electronics". In: *Nature nanotechnology* 5.10 (2010), p. 722.
- [22] Sujay B Desai et al. "Gold-mediated exfoliation of ultralarge optoelectronically-perfect monolayers". In: *Advanced Materials* 28.21 (2016), pp. 4053–4058.
- [23] Francis J. DiSalvo. "Thermoelectric Cooling and Power Generation". In: *Science* 285.5428 (1999), p. 703. DOI: [10.1126/science.285.5428.703](https://doi.org/10.1126/science.285.5428.703).
- [24] M.S. Dresselhaus et al. "New Directions for Low-Dimensional Thermoelectric Materials". In: *Advanced Materials* 19.8 (2007), p. 104.
- [25] Jason K Ellis, Melissa J Lucero, and Gustavo E Scuseria. "The indirect to direct band gap transition in multilayered MoS<sub>2</sub> as predicted by screened hybrid density functional theory". In: *Applied Physics Letters* 99.26 (2011), p. 261908.
- [26] Aleksey Falin et al. "Mechanical properties of atomically thin boron nitride and the role of interlayer interactions". In: *Nature communications* 8 (2017), p. 15815.
- [27] Clement Faugeras et al. "Thermal Conductivity of Graphene in Corbino Membrane Geometry". In: *ACS Nano* 4 (2010), p. 1889. DOI: [10.1021/nm9016229](https://doi.org/10.1021/nm9016229).
- [28] Riccardo Frisenda et al. "Recent progress in the assembly of nanodevices and van der Waals heterostructures by deterministic placement of 2D materials". In: *Chemical Society Reviews* 47.1 (2018), pp. 53–68.
- [29] H. Fritzsche. "A general expression for the thermoelectric power". In: *Solid State Commun.* 9 (1971), p. 1813.
- [30] A. K. Geim and I. V. Grigorieva. "Van der Waals heterostructures". In: *Nature* 449 (2013), p. 419.
- [31] Raphael German et al. "Phonon mode calculations and Raman spectroscopy of the bulk-insulating topological insulator BiSbTeSe<sub>2</sub>". In: *Physical Review Materials* 3.5 (2019), p. 054204.
- [32] A.P. Gerytch et al. "Thermal properties of thin films made from MoS<sub>2</sub> nanoflakes and probed via statistical optothermal Raman method". In: *Scientific Reports* 9 (2019), p. 13338.

- [33] V Gnezdilov et al. "Helical fluctuations in the Raman response of the topological insulator Bi<sub>2</sub>Se<sub>3</sub>". In: *Physical Review B* 84.19 (2011), p. 195118.
- [34] Roman V Gorbachev et al. "Hunting for monolayer boron nitride: optical and Raman signatures". In: *Small* 7.4 (2011), pp. 465–468.
- [35] K. Goasa et al. "Multiphonon resonant Raman scattering in MoS<sub>2</sub>". In: *Appl. Phys. Lett.* 104 (2014), p. 092106. DOI: [10.1063/1.4867502](https://doi.org/10.1063/1.4867502).
- [36] Bartłomiej Graczykowski et al. "Thermal conductivity and air-mediated losses in periodic porous silicon membranes at high temperatures". In: *Nature communications* 8.1 (2017), pp. 1–9.
- [37] Bacel Hamdou et al. "Thermoelectric properties of band structure engineered topological insulator (Bi<sub>1-x</sub>Sb<sub>x</sub>)<sub>2</sub>Te<sub>3</sub> Nanowires". In: *Advanced Energy Materials* 5.14 (2015), p. 1500280.
- [38] RJ Hannemann. *Thermal control of electronics: Perspectives and prospects*. Tech. rep. 2003.
- [39] Shuo Huang et al. "Thermal conductivity measurement of submicrometer-scale silicon dioxide films by an extended micro-Raman method". In: *Microsystem Technologies* 15.6 (2009), pp. 837–842. ISSN: 1432-1858. DOI: [10.1007/s00542-009-0824-3](https://doi.org/10.1007/s00542-009-0824-3). URL: <https://doi.org/10.1007/s00542-009-0824-3>.
- [40] J Humlíček et al. "Raman and interband optical spectra of epitaxial layers of the topological insulators Bi<sub>2</sub>Te<sub>3</sub> and Bi<sub>2</sub>Se<sub>3</sub> on BaF<sub>2</sub> substrates". In: *Physica Scripta* 2014.T162 (2014), p. 014007.
- [41] "Intel 50 years of Moore's law, <https://www.intel.com/content/www/us/en/silicon-innovations/moores-law-technology.html>". In: ().
- [42] Achint Jain et al. "Minimizing residues and strain in 2D materials transferred from PDMS". In: *Nanotechnology* 29.26 (2018), p. 265203.
- [43] Jaeho Jeon et al. "Layer-controlled CVD growth of large-area two-dimensional MoS<sub>2</sub> films". In: *Nanoscale* 7.5 (2015), pp. 1688–1695.
- [44] Puqing Jiang et al. "Anisotropic thermal transport in bulk hexagonal boron nitride". In: *Phys. Rev. Materials* 2 (2018), p. 064005. DOI: [10.1103/PhysRevMaterials.2.064005](https://doi.org/10.1103/PhysRevMaterials.2.064005).

- [45] Insun Jo et al. "Basal-plane thermal conductivity of few-layer molybdenum disulfide". In: *Applied Physics Letters* 104.20 (2014), p. 201902.
- [46] Insun Jo et al. "Thermal conductivity and phonon transport in suspended few-layer hexagonal boron nitride". In: *Nano letters* 13.2 (2013), pp. 550–554.
- [47] Kibum Kang et al. "Layer-by-layer assembly of two-dimensional materials into wafer-scale heterostructures". In: *Nature* 550.7675 (2017), p. 229.
- [48] Jae-Jeong Kim. *Method for removing etch residue material*. US Patent 5,873,948. 1999.
- [49] Keun Soo Kim et al. "Large-scale pattern growth of graphene films for stretchable transparent electrodes". In: *nature* 457.7230 (2009), p. 706.
- [50] Kyoungwan Kim et al. "van der Waals heterostructures with high accuracy rotational alignment". In: *Nano letters* 16.3 (2016), pp. 1989–1995.
- [51] PG Klemens. "Theory of the a-Plane Thermal Conductivity of Graphite". In: *Thermal Conductivity* 22 (1993), pp. 365–365.
- [52] Jae-Ung Lee et al. "Thermal conductivity of suspended pristine graphene measured by Raman spectroscopy". In: *Phys. Rev. B* 83 (2011), p. 081419.
- [53] Jae-Ung Lee et al. "Thermal conductivity of suspended pristine graphene measured by Raman spectroscopy". In: *Physical Review B* 83.8 (2011), p. 081419.
- [54] Chao Li, Peng Zhou, and David Wei Zhang. "Devices and applications of van der Waals heterostructures". In: *Journal of Semiconductors* 38.3 (2017), p. 031005.
- [55] Duanhui Li et al. "Temperature dependence of the Raman spectra of Bi<sub>2</sub>Te<sub>3</sub> and Bi<sub>0.5</sub>Sb<sub>1.5</sub>Te<sub>3</sub> thermoelectric films". In: *physica status solidi (RRL)–Rapid Research Letters* 6.6 (2012), pp. 268–270.
- [56] Hai Li et al. "A universal, rapid method for clean transfer of nanostructures onto various substrates". In: *ACS nano* 8.7 (2014), pp. 6563–6570.

- [57] Xuesong Li et al. "Transfer of large-area graphene films for high-performance transparent conductive electrodes". In: *Nano letters* 9.12 (2009), pp. 4359–4363.
- [58] L Lindsay, DA Broido, and Natalio Mingo. "Flexural phonons and thermal transport in graphene". In: *Physical Review B* 82.11 (2010), p. 115427.
- [59] H.-L. Liu et al. "Anomalous lattice vibrations of monolayer MoS<sub>2</sub> probed by ultraviolet Raman scattering". In: *Phys. Chem. Chem. Phys.*, 17 (2015), p. 14561.
- [60] Yi Liu et al. "Thermal conductance of the 2D MoS<sub>2</sub>/h-BN and graphene/h-BN interfaces". In: *Scientific reports* 7 (2017), p. 43886.
- [61] Oriol Lopez-Sanchez et al. "Ultrasensitive photodetectors based on monolayer MoS<sub>2</sub>". In: *Nature nanotechnology* 8.7 (2013), p. 497.
- [62] Xuezhong Ma et al. "Capillary-force-assisted clean-stamp transfer of two-dimensional materials". In: *Nano letters* 17.11 (2017), pp. 6961–6967.
- [63] Kin Fai Mak et al. "Atomically thin MoS<sub>2</sub>: a new direct-gap semiconductor". In: *Physical review letters* 105.13 (2010), p. 136805.
- [64] L. M. Malard et al. "Raman spectroscopy as a versatile tool for studying the properties of graphene". In: *Nature Nanotechnol.* 8 (2013), p. 235.
- [65] L. M. Malard et al. "Raman spectroscopy in graphene". In: *Physics Reports* 473 (2009), p. 51.
- [66] Debendra Mallik et al. "Advanced Package Technologies for High-Performance Systems." In: *Intel Technology Journal* 9.4 (2005).
- [67] Puspashree Mishra and K. P. Jain. "Temperature-dependent Raman scattering studies in nanocrystalline silicon and finite-size effects". In: *Phys. Rev. B* 62 (22 2000), pp. 14790–14795. DOI: [10.1103/PhysRevB.62.14790](https://doi.org/10.1103/PhysRevB.62.14790). URL: <https://link.aps.org/doi/10.1103/PhysRevB.62.14790>.
- [68] Thao TT Nguyen et al. "Enhanced thermoelectricity at the ultra-thin film limit". In: *arXiv preprint arXiv:1912.11274* (2019).

- [69] Denis L Nika, Artur S Askerov, and Alexander A Balandin. "Anomalous size dependence of the thermal conductivity of graphene ribbons". In: *Nano letters* 12.6 (2012), pp. 3238–3244.
- [70] DL Nika et al. "Lattice thermal conductivity of graphene flakes: Comparison with bulk graphite". In: *Applied Physics Letters* 94.20 (2009), p. 203103.
- [71] K. S. Novoselov et al. "2D materials and van der Waals heterostructures". In: *Science* 353 (2016).
- [72] KS Novoselov et al. "2D materials and van der Waals heterostructures". In: *Science* 353.6298 (2016), aac9439.
- [73] P. S. Peercy and B. Morosin. "Pressure and Temperature Dependences of the Raman-Active Phonons in  $\text{SnO}_2$ ". In: *Phys. Rev. B* 7 (6 1973), pp. 2779–2786. DOI: [10.1103/PhysRevB.7.2779](https://doi.org/10.1103/PhysRevB.7.2779). URL: <https://link.aps.org/doi/10.1103/PhysRevB.7.2779>.
- [74] Peltier. "Nouvelles expériences sur la calorité des courants électrique". In: *Annales de Chimie et de Physique* 56 (1834), p. 371.
- [75] Michael Thompson Pettes et al. "Influence of Polymeric Residue on the Thermal Conductivity of Suspended Bilayer Graphene". In: *Nano Letters* 11 (2011), p. 1195. DOI: [10.1021/nl1104156y](https://doi.org/10.1021/nl1104156y).
- [76] Filippo Pizzocchero et al. "The hot pick-up technique for batch assembly of van der Waals heterostructures". In: *Nature communications* 7 (2016), p. 11894.
- [77] S. Périchon et al. "Measurement of porous silicon thermal conductivity by micro-Raman scattering". In: *Journal of Applied Physics* 86.8 (1999), pp. 4700–4702. DOI: [10.1063/1.371424](https://doi.org/10.1063/1.371424). eprint: <https://doi.org/10.1063/1.371424>. URL: <https://doi.org/10.1063/1.371424>.
- [78] Branimir Radisavljevic, Michael Brian Whitwick, and Andras Kis. "Integrated circuits and logic operations based on single-layer  $\text{MoS}_2$ ". In: *ACS nano* 5.12 (2011), pp. 9934–9938.
- [79] C. V. Raman and K. S. Krishnan. "A New Type of Secondary Radiation". In: *Nature* 58 (1928), p. 501.

- [80] JS Reparaz et al. "A novel contactless technique for thermal field mapping and thermal conductivity determination: two-laser Raman thermometry". In: *Review of Scientific Instruments* 85.3 (2014), p. 034901.
- [81] W Richter and CR Becker. "A Raman and far-infrared investigation of phonons in the rhombohedral V2–VI3 compounds Bi2Te3, Bi2Se3, Sb2Te3 and Bi2 (Te1- xSex) 3 (0 < x < 1), (Bi1- ySby) 2Te3 (0 < y < 1)". In: *physica status solidi (b)* 84.2 (1977), pp. 619–628.
- [82] Alexander Rigort and Jürgen M Plitzko. "Cryo-focused-ion-beam applications in structural biology". In: *Archives of biochemistry and biophysics* 581 (2015), pp. 122–130.
- [83] Satyaprakash Sahoo et al. "Temperature-dependent Raman studies and thermal conductivity of few-layer MoS2". In: *The Journal of Physical Chemistry C* 117.17 (2013), pp. 9042–9047.
- [84] R. Saito et al. "Raman spectroscopy of transition metal dichalcogenides". In: *J. Phys.: Condens. Matter* 28 (2016), p. 353002.
- [85] D Schmeltzer and Avadh Saxena. "Interference effects for T 2= - 1 time reversal invariant topological insulators: Surface optical and Raman conductivity". In: *Physical Review B* 88.3 (2013), p. 035140.
- [86] Markus Schmotz et al. "A thermal diode using phonon rectification". In: *New Journal of Physics* 13.11 (2011), p. 113027.
- [87] Seebeck. "Magnetische Polarisation der Metalle und Erze durch Temperatur-Differenz". In: *Phys. Klasse* (1822).
- [88] KMF Shahil et al. "Crystal symmetry breaking in few-quintuple Bi 2 Te 3 films: Applications in nanometrology of topological insulators". In: *Applied physics letters* 96.15 (2010), p. 153103.
- [89] E. K. Sichel et al. "Heat capacity and thermal conductivity of hexagonal pyrolytic boron nitride". In: *Phys. Rev. B* 13 (1976), p. 4607.
- [90] G.J. Snyder and E. S. Toberer. "Complex thermoelectric materials". In: *Nature* 7 (2008), p. 105.
- [91] Houfu Song et al. "Two-dimensional materials for thermal management applications". In: *Joule* 2.3 (2018), pp. 442–463.
- [92] Marin Steenackers et al. "Polymer brushes on graphene". In: *Journal of the American Chemical Society* 133.27 (2011), pp. 10490–10498.

- [93] W. Thomson. "On a mechanical theory of thermo-electric currents". In: *Proceedings of the Royal Society of Edinburgh* 3 (1851), p. 91.
- [94] Johann Toudert and Rosalía Serna. "Interband transitions in semi-metals, semiconductors, and topological insulators: a new driving force for plasmonics and nanophotonics". In: *Optical Materials Express* 7.7 (2017), pp. 2299–2325.
- [95] Rama Venkatasubramanian et al. "Thin-film thermoelectric devices with high room-temperature figures of merit". In: *Nature* 413.6856 (2001), pp. 597–602.
- [96] Chengru Wang et al. "Superior thermal conductivity in suspended bilayer hexagonal boron nitride". In: *Scientific reports* 6 (2016), p. 25334.
- [97] Chunxiao Wang et al. "In situ Raman spectroscopy of topological insulator Bi<sub>2</sub>Te<sub>3</sub> films with varying thickness". In: *Nano Research* 6.9 (2013), pp. 688–692.
- [98] Qing Hua Wang et al. "Electronics and optoelectronics of two-dimensional transition metal dichalcogenides". In: *Nature nanotechnology* 7.11 (2012), p. 699.
- [99] Wenzhuo Wu et al. "Piezoelectricity of single-atomic-layer MoS<sub>2</sub> for energy conversion and piezotronics". In: *Nature* 514.7523 (2014), p. 470.
- [100] X. Xu et al. "Thermal conductivity of suspended pristine graphene measured by Raman spectroscopy". In: *Nature Commun.* 5 (2014), p. 3689.
- [101] Xiangfan Xu et al. "Length-dependent thermal conductivity in suspended single-layer graphene". In: *Nature communications* 5 (2014), p. 3689.
- [102] Rusen Yan et al. "Raman and Photoluminescence Study of Dielectric and Thermal Effects on Atomically Thin MoS<sub>2</sub>". In: *arXiv:1211.4136* (2013).
- [103] Rusen Yan et al. "Thermal Conductivity of Monolayer Molybdenum Disulfide Obtained from Temperature-Dependent Raman Spectroscopy". In: *ACS Nano* 8 (2014), p. 986.



- [104] Rusen Yan et al. "Thermal conductivity of monolayer molybdenum disulfide obtained from temperature-dependent Raman spectroscopy". In: *ACS nano* 8.1 (2014), pp. 986–993.
- [105] Pengyu Yuan et al. "Nonmonotonic thickness-dependence of in-plane thermal conductivity of few-layered MoS<sub>2</sub>: 2.4 to 37.8 nm". In: *Physical Chemistry Chemical Physics* 20.40 (2018), pp. 25752–25761.
- [106] C. Yuang et al. "Modulating the thermal conductivity in hexagonal boron nitride via controlled boron isotope concentration". In: *Commun Phys.* 2 (2019), p. 43.
- [107] Alexander Yulaev et al. "Toward clean suspended CVD graphene". In: *RSC advances* 6.87 (2016), pp. 83954–83962.
- [108] Xian Zhang et al. "Measurement of lateral and interfacial thermal conductivity of single-and bilayer MoS<sub>2</sub> and MoSe<sub>2</sub> using refined optothermal Raman technique". In: *ACS applied materials & interfaces* 7.46 (2015), pp. 25923–25929.